second harmonic generation diagnostic of polymers and elecronic matarials.

Siu-Wai Wallace Chan

To cite this version:

Siu-Wai Wallace Chan. second harmonic generation diagnostic of polymers and elecronic matarials.. Atomic Physics [physics.atom-ph]. Université d'Angers, 2007. English. NNT : . tel-00159741

HAL Id: tel-00159741

https://theses.hal.science/tel-00159741

Submitted on 4 Jul 2007

UNIVERSITÉ D'ANGERS

Année 2007
N° d'ordre 795

Diagnostique de polymères et de matériaux électroniques par génération de second harmonique

THÈSE DE DOCTORAT

Spécialité : Physique

ÉCOLE DOCTORALE D'ANGERS

Présentée et soutenue publiquement

le : 16 Mars 2007
à : Angers
par : Siu Wai CHAN

Devant le jury ci-dessous :

François KAJZAR (Rapporteur), Professeur, Université d'Angers
Inta MUZIKANTE (Rapporteur), Professeur, Université de Lettonie, Lettonie
Aleksandra B. DJURIŠIĆ (Rapporteur), Assistant professeur, Université de Hong Kong
Régis BARILLE (Examinateur), Professeur, Université d'Angers
Sylvie DABOS-SEIGNON (Examinateur), Maître de conférence, CNRS-Université d'Angers
Aleksandra APOSTOLUK (Examinateur), Maître de conférence, INSA de Lyon

Directeur de thèse : Professeur Jean-Michel NUNZI
Co-directrice : Docteur Sylvie DABOS-SEIGNON

Laboratoire d'accueil : Propriétés Optiques des Matériaux et Applications (POMA), UMR-CNRS 6136, Université d'Angers, 2 Boulevard Lavoisier, 49045 Angers, France

Résumé

La stabilité optique nonlinéaire du colorant (Disperse red 1) dopé dans différent polymères amorphes préparés par spin-coating ou incorporé dans un polymère préparé par le processus auto-assemblé Layer-by-Layer (LBL) a été étudiée. La relaxation de rotation du colorant est analysée en mesurant la variation de susceptibilité de second ordre induite par le poling tout-optique. Nous montrons que la température de transition vitreuse du polymère n'est pas le seul facteur qui influe sur la stabilité de rotation libre de colorant. Par contre, l'architecture de polymère (la polarité de la chaîne polymère) joue son rôle sur la stabilité de rotation. Nous discutons du ralentissement de la relaxation de rotation moléculaire sur le poling tout-optique. Un modèle 'restoring torque' est introduit pour étudier la stabilité d'orientation intrinsèque de colorant dans polymère préparé par le processus auto-assemblé Layer-by-Layer.

La propriété optique nonlinéaire de second ordre d'oxyde de zinc est étudiée a l' échelle de millimètre jusqu'à nano-mètre. L'effet de surface sur l'augmentation de réponse de la génération de second harmonique est montré. Nous suggérons que la génération de second harmonique induite par le champ électrique crée par la séparation des charges est l'origine de l'augmentation proéminent des susceptibilités à second ordres.

Nous discutons la réponse significative d'optique nonlinéaire de second ordre de fullerène (C60) et phthalocyanine de cuivre (CuPc) qui sont de nature centro-symétrique. L'influence d'épaisseur de couche et le substrat nous montre l'origine de la génération de second harmonique : la génération de second harmonique induite par le champ électrique de la séparation de charge à l'interface du substrat et de la couche. Elle n'est pas à cause des mécanismes d'optique nonlinéaire aux ordres plus élevés. En plus, la technique 'Kelvin Probe' est introduite pour analyser quantitativement le transfert de charge à l'interface.

Mots-clès : Poling Tout-Optique, Génération de Second Harmonique, relaxation de $\chi^{(2)}$, Auto-assemblé Layer-By-Layer, transfert de charge interfacial

Abstract

Nonlinear optical response stability of azo-dye (disperse red 1) doped amorphous glassy polymers prepared by spin-coating and azo-dye functionalized polymer prepared by Layer-by-Layer self-assembly process is studied and discussed. Results of second order nonlinear susceptibility relaxation reveal that rotational stability of dopant depends not only on glass transition temperature but also on polymer architecture. Retardation of rotational relaxation of dopant upon All-Optical Poling is discussed. In addition, a 'restoring torque' model is introduced for understanding intrinsic orientation stability of azo-dye in Layer-by-Layer nonlinear optical polymer.

Second order nonlinear optical properties of a polar inorganic crystal (Zinc Oxide) scaling from milli-meter to nano-meter is studied. Size effect of zinc oxide crystal to its second order nonlinear susceptibility is studied. Second Harmonic Generation (SHG) measurement shows that for nano-scale zinc oxide crystal, surface effect has to be taken into account for its contribution to SHG. Enhancement of SHG in nano-scale zinc oxide is attributed to efficient charge separation at nano-crystal surface. Electric Field Induced Second Harmonic Generation (EFISHG) contributes significantly to SHG of nano-size zinc oxide clusters due to the establishment of strong local external electric field across nano-structure. Quantity of charge accumulation during photo-excitation is also estimated.

Centro-symmetric electronic materials fullerene (C60) and copper phthalocyanine (CuPc) are found to give high second order nonlinear optical response which is not comprehensible under the consideration of the absence of dipole-allowed high second harmonic generation contribution. Inverse proportionality of sample thickness to its second order nonlinear response suggests that quadratic nonlinear optical response of C60 and CuPc do not originate from higher order nonlinear optical mechanisms. We propose that there is a spontaneous charge transfer at the interface of substrate and organic film (C60 or CuPc) which leads to EFISHG effect. Kelvin probe technique for surface potential measurement is discussed for investigating interfacial charge transfer phenomena.

Keywords : All-Optical Poling, Second Harmonic Generation, relaxation of $\chi^{(2)}$, Layer-By-Layer self-assembly, interfacial charge transfer

REMERCIEMENTS

Cette thèse a été accomplie au sein du laboratoire POMA (Propriétés Optiques des Matériaux et Applications) de l'Université d'Angers sous la direction de Prof. Jean-Michel NUNZI et sous la co-direction de Dr. Sylvie DABOS-SEIGNON. Je suis très reconnaissant au Conseil Général du Maine-et-Loire de m'avoir accordé une aide financière durant ces trois années de préparation de doctorat.

Je remercie vivement Prof. André MONTEIL, directeur de laboratoire POMA, de m'avoir accueilli dans son laboratoire durant ces trois années.

Les jurys de ma thèse ont donne beaucoup de opinions scientifiques sue mon travail qui sont tous précieux pour la connaissance plus profonde dans ma domaine de travail. Je remercie Prof. F. KAJZAR (le président du jury), Dr. I. MUZIKANTE et Dr. A. B. DJURIŠIĆ de leur rapportages sur ma thèse. En plus, je remercie Prof. J.-M. NUNZI, Prof. R. BARILLE, Dr. S. DABOS-SEIGNON et Dr. A. APOSTOLUK d'être l'examinateur de ma soutenance.

Mes remerciements les plus ardents iront au Prof. Jean-Michel NUNZI, pour m'avoir accueilli et m'avoir donné le sentiment de faire partie intégrante de son équipe, de m'avoir guidé à la fois dans la recherche et dans ma vie. Grâce à lui j'ai découvert le domaine de recherche et les sujets liés. Sa vision, son discernement et sa générosité dans le partage de ses connaissances m'ont galvanisé et poussé à perfectionner mon travail source d'intérêts et d'épanouissement intellectuel.

J'exprime également ma profonde gratitude à mes co-équipiers et collaborateurs: Unni, Gabi, David, Frédérique, Kitty, Ajay, Adrien, Amel, Sohrab, Katherine, Fei, Hassina, Régis, Abdel, Prof. R. BARILLE, Dr. S. DABOS-SEIGNON, Dr. M. GIRTAN, Dr. D. GINDRE et Dr. M. SYLLA, leur soutien et leur conseil m'ont permis d'effectuer le travail présenté ici.

Je remercie particulièrement Prof. R. BARILLE, Dr. S. DABOS-SEIGNON et Dr. A. APOSTOLUK pour la relecture du manuscrit et les suggestions sur la présentation de ma soutenance.

L'équipe technique et administrative (René, Alain, Julien, Nicolas, Christian, Dominique, Christophe, Isabelle, Marie-France, Marie-Thérèse) ont toujours été disponible pour m'aider. A eux, un grand merci du fond du coeur.

J'ai beaucoup apprécié les discussions scientifiques avec Dr. A. QUATELA de Rome, Dr. E. ORTYL, K. MARAŃSKI de Wrocław, Pr. I. MUZIKANTE, Dr. M. RUTKIS, A. VEMBRIS de Riga et Dr. A. B. DJURIŠIĆ, Dr. W. K. CHAN, Y. H. LEUNG, K. H. TAM de Hong Kong. Ils m'ont fait partager leur expériences sur le travail, la vie, le V.T.T, les voyages et plus encore.

Avec les thésards, les stagiaires et les invités venants de différents coins du monde, nous avons crée un monde en miniature. Nos diverses conversations dans une ambiance conviviale m'ont permis d'enrichir mes connaissances sur les différentes cultures, coutumes et traditions. Tout cela a contribué à mon épanouissement personnel.

Vivre dans un pays totalement étranger n'a pas été évident et j'exprime ma gratitude à ceux du POMA qui m'ont aidé et encouragé à m'adapter et me familiariser à la langue 'romantique'.

Merci à ma famille, ma chérie, mes amis et mon chat qui m'ont soutenu et qui ont eu une totale confiance en moi.

Contents

Chapter 1
OVERVIEW

Chapter 2
SECOND HARMONIC GENERATION OF AZO-DYE NONLINEAR OPTICAL GLASSY POLYMER

Chapter 3
NLO CHARACTERIZATION OF ZINC OXIDE FROM MILLI-METER TO NANO-METER

Chapter 4
SHG OF CENTROSYMMETRIC ORGANIC ELECTRONIC MATERIALS

Symbols

$\chi^{(2)}$: Second order nonlinear optical susceptibility
ε_o : Dielectric permittivity of vacuum
ε : Dielectric permittivity of media
Δn : Birefrigence
α : Linear molecular polarizability/Linear absorption coefficient
β : Molecular hyperpolarizability
μ : Dipole moment
$\wp$: Aspect ratio of nanorod
υ : Volume ratio of zinc oxide nanorod
κ, δ : Linear absorption coefficient
ω : Optical frequency
ω_o : Natural frequency of harmonic oscillator
γ : Damping constant of harmonic oscillator/Ratio $\left|E_{2\omega} / E_{\omega}^{2}\right|$
η : Polymer viscosity
ξ : High-order response of harmonic oscillator/quantum efficiency of orientation
k_ω : Wavevector at optical frequency ω
E_a : Activation energy
k_B : Boltzmann constant
U : Interaction energy between dipole and polymer environment
Ω : Solid angle in spherical coordinate
$\bar{\ell}$: Average nanorod length
$\bar{d}$: Average nanorod diameter
$\langle\tau\rangle$: Decay time constant
τ : Thermal diffusion constant
t' : Time of all-optical poling
ϕ : Relative phase difference between fundamental and second harmonic EM fields
a : Weight constant of bi-exponential decay function
Ξ : Magnetic dipole coefficient
Δ : Electric quadruple coupling coefficient
Γ : Magnetic dipole coupling coefficient
Q : Electric quadruple coefficient
σ : Surface charge density
$\hbar$: Planck constant

Abbreviations

ZnONR : Zinc Oxide Nano-Rod
NLO : Nonlinear Optical
NL : Nonlinear
EM : ElectroMagnetic
E : Electric field
B : Magnetic field
SHG : Second Harmonic Generation
SH : Second Harmonic
LBL : Layer-By-Layer
PC : Poly(Carbonate)
PMMA : Poly(Methyl MethacrylAte)
DR-1 : Disperse Red 1
PSU : Poly(SUlfone)
PS : Poly(Styrene)
PEI : Poly(EthyleneImine)
BR : BiRefrigence
T_g : Glass transition temperature
AOP : All-Optical Poling
PAP : Photo-Assisted Poling
TAP : Temperature-Assisted Poling
CP : Corona Poling
RT : Room Temperature
AHB : Angular Hole Burning
EFISHG : Electric Field Induced Second Harmonic Generation
TPP : 5,10,15,20-tetraphenyl-2 I H,23Hporphine
TPN : 5,6,11, I2-tetraphenylnaphthacene
PAS : Positron Annihilation Spectroscopy
CPD : Contact Potential Difference
KP : Kelvin Probe
PNA : ParaNitroAniline
NR : Nano-Rod
FE : Field Emission
GH : Guest-host

INTRODUCTION

In the past twenty to thirty years, nonlinear optical (NLO) polymer has been extensively studied for its high potential application in fast-response optoelectronic industry because of its fabrication flexibility, property modification capability, easy manipulation, etc… However, polymeric structure exhibits considerable property degradation due to the softness of polymer. Temporal stability of NLO polymer has to be improved to fully put it into practice and application. In addition, understanding its physical properties is of important for device design and application. Azo-dye polymer is generally regarded as a good candidate for second order nonlinear optical application once its centro-symmetry is broken by either different poling methods or noncentro-symmetric polymer self-assembly technique. All-Optical Poling is of particular big interest for NLO polymer poling due to its microscopic control to molecular orientation. Layer-by-Layer self-assembly of azo-polymer is an alternative promising method to break centro-symmetry of nonlinear polymer system which gives an extremely stable nonlinear optical polymeric system for applications like fast optical-switching, frequency doubling device. In this thesis, we will explore various factors (e.g. Glass transition temperature, polymer dispersivity and polarity of polymer structure) determining the stability of noncentro-symmetric configuration of azo-dye nonlinear optical polymers which are poled by All-Optical Poling and are diagnosed by Second Harmonic Generation (SHG). For intrinsic structural noncentro-symmetric azo-dye nonlinear optical polymer prepared by Layer-by-Layer self-assembly, we have performed All-Optical Poling (as secondary poling) and Second Harmonic Generation measurement to access intrinsic azo-dye alignment in Layer-by-Layer nonlinear polymer and its photo-orientation stability upon All-Optical Poling. These will be further discussed in Chapter 2 in the thesis. In chapter 1, an overview of the origin of Second Harmonic Generation will be presented with a classical oscillator model given. The simulations of Second Harmonic Generation in nonlinear medium will be provided and their main features will be discussed.

In chapter 3, Second Harmonic Generation of inorganic zinc oxide polar single crystal will be presented. Polar zinc oxide is a good candidate as one of the building block of transitor, solar cell and sensor. It is also fabricated into nano-scale to increase effective area or efficiency for the desired function. Researchers studied second order nonlinear optical characteristic of zinc oxide single crystal extensively and in this thesis, we investigate second order nonlinear optical susceptibility of zinc oxide from milli-meter crystal to nano-meter crystal. Researchers claimed that there is surface effect of nano-crystal to Second Harmonic Generation enhancement of zinc oxide nano-structure but no direct evidence has been given. We will discuss Second Harmonic Generation enhancement in zinc oxide nano-rod and we will justify the origin of high second order nonlinear response from nano-size zinc oxide polar crystal. We suggest that Electric Field Induced Second Harmonic Generation (EFISHG) from nano-size crystal is responsible for the enhancement of second order nonlinear optical effect. Charge separation across nano-size crystal. We will estimate too charge accumulation density on Zinc Oxide nano-crystal.

In the last chapter of this thesis, Second Harmonic Generation measurement of centro-symmetric electronic materials (C60 and CuPc) will be presented. We show convincingly that high second order nonlinear optical response of centro-symmetric C60 and CuPc is originated from spontaneous interfacial charge transfer across substrate and organic film (C60 or CuPc). Large second order nonlinear optical response from C60 or CuPc is excluded from dominant contribution of higher order nonlinear optical effects. N-type and p-type semi-conductors (C60 and CuPc) and intrinsic semi-conducting substrate are charged up complimentarily due to interfacial charge transfer. It leads to high Electric Field Induced Second Harmonic Generation effect from these centro-symmetric films. Charge transfer across interface is estimated. Quantitative surface potential measurement by Kelvin Probe technique will be discussed for further studies of the charging effect across interface between centro-symmetric semi-conductors.

CHAPTER 1
OVERVIEW

In this chapter, we give a general overview of the basis of Second Harmonic Generation (SHG) mechanism from the classical electro dynamical point of view. It shows the essential idea of the origin of SHG. In addition, an example of second harmonic (SH) electromagnetic (EM) field propagation in nonlinear (NL) material is given for illustration.

1.1 Harmonic oscillator

High-order optical effect like Second Harmonic Generation (SHG) can be understood with the help of dipolar harmonic oscillator[1] as shown in figure 1.1 :

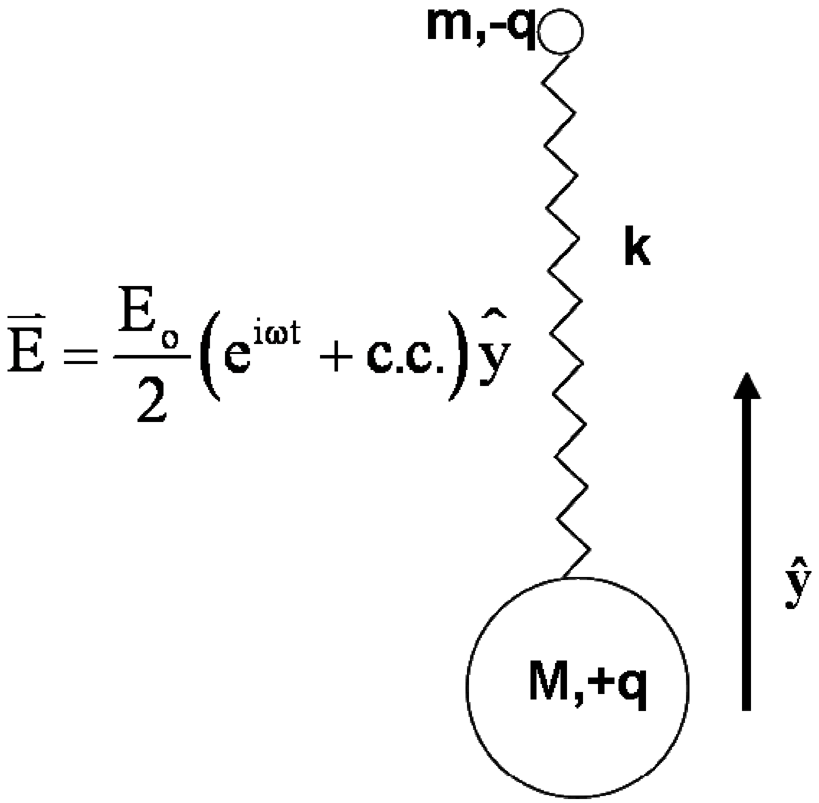

Figure 1.1. Harmonic oscillator under electromagnetic field

An electromagnetic (EM) field of frequency (ω) interacts with a dipole of charge (q) with spring constant (k) which is similar to a dipole system comprising a massive nuclei

(M, +q) and light outermost electrons (m, -q). Equation of motion of the dipole can be expressed as :

$$\ddot{y} + \gamma\dot{y} + \omega_o{}^2 y + \sum_{i>0}\xi_{2i}y^{2i} + \sum_{i>0}\xi_{2i+1}y^{2i+1} = \frac{qE_o}{2m}\left(e^{i\omega t} + c.c.\right) \tag{1.1}$$

where γ is damping constant, $\omega_o{}^2 = k/m$ and $\sum_{i>0}\xi_{2i}y^{2i}$ are higher order asymmetrical response terms and $\sum_{i>0}\xi_{2i+1}y^{2i+1}$ are higher order symmetrical response terms. For illustrating the emergence of the second harmonic generation with the above dipole oscillator model, we consider only the lowest order asymmetrical response term $\xi_2 y^2$ in the equation of motion of the dipole :

$$\ddot{y} + \gamma\dot{y} + \omega_o{}^2 y + \xi_2 y^2 = \frac{qE_o}{2m}\left(e^{i\omega t} + c.c.\right) \tag{1.2}$$

where ξ_2 is the strength constant of the lowest order asymmetrical response. We consider solution of y-displacement in the form as follow :

$$y = \frac{1}{2}\left(A_1 e^{i\omega t} + A_2 e^{i2\omega t} + c.c.\right) \tag{1.3}$$

because we aim at seeking the solution of y at second harmonic oscillating frequency 2ω. Dipole oscillation motion can be further expressed as :

$$\begin{aligned} & -\frac{\omega^2}{2}\left(A_1 e^{i\omega t} + c.c.\right) - 2\omega^2\left(A_2 e^{i2\omega t} + c.c.\right) + i\frac{\omega\gamma}{2}\left(A_1 e^{i\omega t} - c.c.\right) \\ & + i\omega\gamma\left(A_2 e^{i2\omega t} - c.c.\right) + \frac{\omega_o{}^2}{2}\left(A_1 e^{i\omega t} + A_2 e^{i2\omega t} + c.c.\right) \\ & + \frac{\zeta_2}{4}\begin{pmatrix} A_1{}^2 e^{i2\omega t} + A_2{}^2 e^{i4\omega t} + A_1\overline{A_1} + 2A_1A_2 e^{i3\omega t} \\ +2A_1\overline{A_2}e^{-i\omega t} + A_2\overline{A_2} + c.c. \end{pmatrix} = \frac{qE_o}{2m}\left(e^{i\omega t} + c.c.\right) \end{aligned} \tag{1.4}$$

$\{e^{in\omega t}\}_{n\rightarrow \text{integer}}$ is an orthogonal set of basis. By comparing the coefficient of $e^{in\omega t}$ in equation 1.4, amplitudes (A_1,A_2) of y-oscillation can be obtained. Equating coefficients of $e^{i\omega t}$ in equation 1.4, amplitude (A_1) of dipolar oscillation at frequency ω is given as :

$$A_1 = \left(\frac{qE_o}{m}\right)\frac{1}{(\omega_o{}^2 - \omega^2) + i\omega\gamma} \tag{1.5}$$

with an assumption that $|\xi_2 A_2| \ll \left[\left(\omega_0{}^2 - \omega^2\right)^2 + \omega^2\gamma^2\right]^{1/2}$. Linear polarization p(ω) of dipole relates to EM field at frequency (ω) by linear susceptibility α :

$$p(\omega) = q\frac{A_1}{2}\left(e^{i\omega t} + c.c.\right) = \alpha\frac{E_o}{2}\left(e^{i\omega t} + c.c.\right) \tag{1.6}$$

$$\alpha = \left(\frac{q^2}{m}\right)\frac{1}{(\omega_o{}^2 - \omega^2) + i\omega\gamma} \tag{1.7}$$

In similar manner, we obtain A_2 by comparing the coefficient of $e^{i2\omega t}$ of equation 1.4 :

$$A_2 = -\frac{\xi_2 A_1{}^2}{2(\omega_o{}^2 - (2\omega)^2 + i2\omega\gamma)} = -\frac{\xi_2 q^2}{2m^2(\omega_o{}^2 - (2\omega)^2 + i2\omega\gamma)\left[(\omega_o{}^2 - \omega^2) + i\omega\gamma\right]^2}E_o{}^2 \tag{1.8}$$

Dipolar polarization p(2ω) at second harmonic frequency 2ω can be related to the first-order nonlinear hyper-polarizability β

$$p(2\omega) = q\frac{A_2}{2}\left(e^{i2\omega t} + c.c.\right) = \beta\frac{E_o{}^2}{4}\left(e^{i2\omega t} + c.c.\right) \tag{1.9}$$

$$\beta = -\frac{\xi_2 q^3}{m^2(\omega_o{}^2 - (2\omega)^2 + i2\omega\gamma)\left[(\omega_o{}^2 - \omega^2) + i\omega\gamma\right]^2} \tag{1.10}$$

For N non-interacting dipolar oscillators per unit volume as described by equation 1.2, linear polarization P(ω) and second harmonic bulk polarization P(2ω) can be expressed simply as

$$P(\omega) = \chi^{(1)}E(\omega) = Np(\omega) = N\alpha E(\omega) \tag{1.11a}$$

$$P(2\omega) = \chi^{(2)}E^2(\omega) = Np(2\omega) = N\beta E^2(\omega) \tag{1.11b}$$

$$\chi^{(1)} = \left(\frac{q^2}{m}\right)\frac{N}{(\omega_o{}^2 - \omega^2) + i\omega\gamma} \tag{1.12a}$$

$$\chi^{(2)} = -\frac{\xi_2 q^3 N}{m^2(\omega_o{}^2 - (2\omega)^2 + i2\omega\gamma)\left[(\omega_o{}^2 - \omega^2) + i\omega\gamma\right]^2} \tag{1.12b}$$

Non-zero bulk second harmonic dipolar polarization P(2ω) acts as a source of second harmonic radiation 2ω which results in second harmonic generation (SHG) that we discuss in principle in this thesis. As we observe from equation 1.12b, $\chi^{(2)}$ can be non-zero only if there exists the asymmetrical response like ξ_2 which assures the lowest order nonlinear optical response (e.g. SHG). For higher order nonlinear optical response P(nω) where n>2, higher order asymmetrical and symmetrical responses (ξ_n for n>2) of dipolar oscillation could be considered thoroughly for the calculation of $\chi^{(n)}$ with method similar to the one shown above. Moreover, for a more precise calculation of bulk (macroscopic) NLO properties giving SHG, thermal-dynamical response of dipole radiators has to be taken into account. For example, if asymmetric radiators are configured centro-symmetrically (randomly) in the system of interest, second (even) order bulk NLO response would vanish due to the cancellation effect. So, poling (ordering of radiators) has to be done for breaking the centro-symmetry of the NLO system. We will discuss poling and centro-symmetry breaking of NLO system (Electric field poling, All-optical poling, Layer-By-Layer polyelectrolyte deposition) in detail for different particular NLO systems in the forthcoming chapter (chapter 2) of this thesis.

Generally speaking, second (even) order nonlinear optical response exists in dipolar system of interest providing that 1) second (even) order asymmetrical response ξ_{2i} is non-vanishing and 2) there is non-zero effective number of oscillators ($N \neq 0$) present in the system. The above asymmetric harmonic oscillation model illustrates the most significant effect of SHG contribution due to electric dipole radiation at second harmonic frequency 2ω. SHG originating from electric dipole mechanism can be found readily in noncentro-symmetric systems like polar inorganic crystals, poled nonlinear optical (NLO) polymeric materials, Langmuir-Blodgett (LB) films, NLO liquid crystals, ferroelectrics and interfaces which are inherently noncentro-symmetric. These lead to great interest in the development of SHG as an efficient optical tool for studying various types of materials and their physical properties[2-5].

As noticed, for the above electric dipole oscillation model, several assumptions were made during calculation like one-dimensional (ŷ) motion and non-magnetic response. These assumptions would be valid for SH response of an rod-like uni-axial polar molecule like push-pull azo-dye and paranitroaniline (PNA) or macromolecules which have relatively strong electric response. However, in reality, molecules span in 3 dimensions with finite sizes. In addition, nonlinear electromagnetic response of system would be not only due to electric field $\vec{E}$ perturbation but also due to simultaneous magnetic field $\vec{B}$ perturbation. Let's consider an example of a chiral system which is non-polar and has helical structure as shown in figure 1.2.

Chiral system is noncentro-symmetric in nature as it is in lack of mirror symmetry. Consider, for simplicity, 2 helical enantiomers which have good electron transport capability like π-conjugated chiral 1,1'-binaphthyl-based helical polymer as shown below[6] :

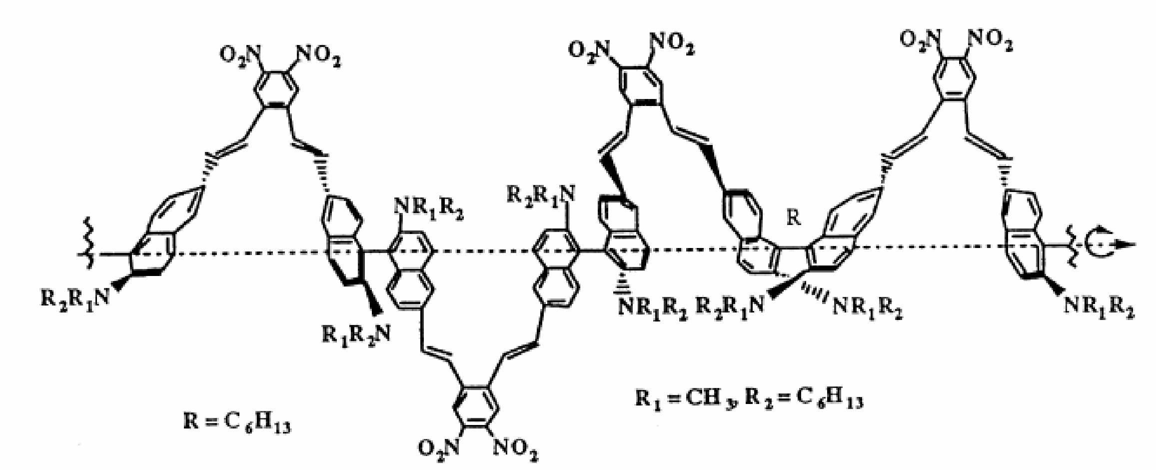

Under EM field perturbation, electrons would drift circularly along the helical path of structure upward or downward depending on handedness of enantiomers. Second harmonic polarization P(2ω) and magnetization M(2ω) is induced and SHG which depends quadratically on EM fields, would include additional terms of interference between electric field and magnetic field perturbations : $P_i(2\omega) \sim \chi^{(2)}_{ijk} E_j B_k$,

$$M_i(2\omega) \sim \chi^{(2)}_{ijk} E_j E_k \,.$$

Recently, SHG of chiral system is attracting big attention both in sense of its importance for fundamental physics understanding and its potential application in the design of NLO systems and bio-structure sensing[7]. Even non-polar chiral system[6, 8, 9], which will be more stable in system configuration compared to polar system, exhibits relatively large SHG effect. Based on quadratic EM field coupling, second harmonic generation-circular dichroism (SHG-CD)[10-13], is developed as an effective tool for studying the handedness of chiral system at interface and second order NLO of racemic system. In the following section we would discuss, in general, the mechanism of SHG which is quadratic dependent on both of the electric field E(ω) and magnetic field B(ω) of electromagnetic EM radiation.

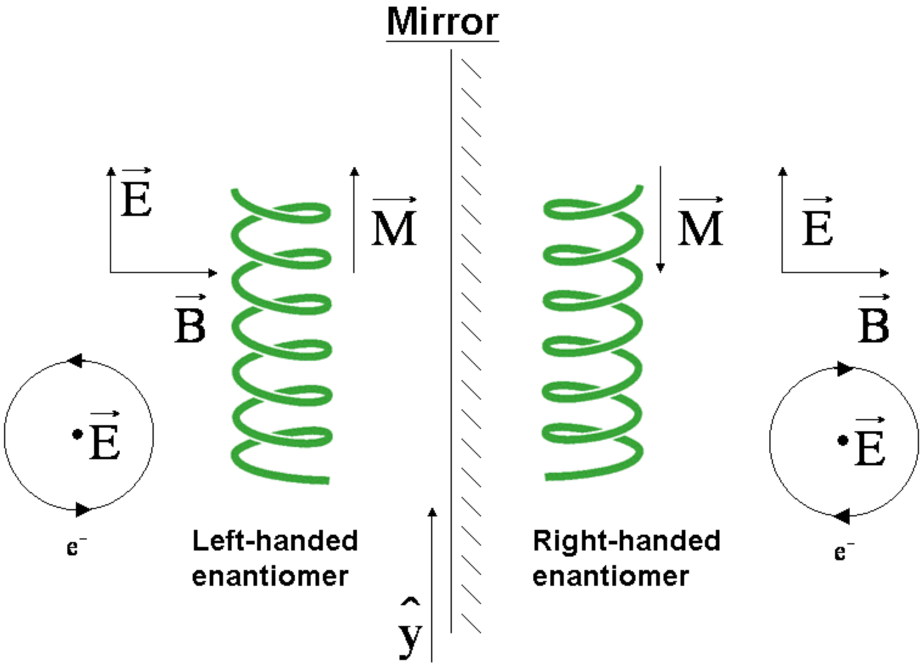

Figure. 1.2 Second Harmonic Generation from chiral helical system of left-handed enantiomer and right-handed enantiomer

1.2 Quadratic EM field dependence SHG

In the above section, SHG from electric-dipole approximation was discussed. However, for understanding SHG due to EM field, both electric and magnetic response of NLO system has to be taken into account equally.

For three dimensional consideration of second harmonic polarization of material under dipole approximation, 3rd rank tensor is incorporated for correlating relationship between electromagnetic field E(ω) and second harmonic polarization P(2ω) :

$$P_i(2\omega) = \chi^{(2)}_{ijk} E_j(\omega) E_k(\omega) \tag{1.13}$$

where contracted notation is employed for simplicity ($\delta_{ij} E_j = \sum_{j=1}^{3} \delta_i E_j$, Cartesian coordinates (x=1,y=2,z=3) of laboratory frame of reference are assigned). For having non-vanishing second harmonic polarization P(2ω), total number of polar terms (e.g. $\chi^{(2)}$, $\vec{E}$) and axial terms (e.g. $\vec{B}$) should be odd. Under electric dipole approximation as shown in equation 1.13, there are 3 polar terms (2 polar $E(\omega)$ + 1 polar $\chi^{(2)}$ = 3 polar terms) which account for second harmonic polarization or in the other words, the source of SHG. If a system possesses inversion symmetry (centro-symmetric organization), Quadratic EM field SHG vanishes as polar term $\chi^{(2)}$ becomes zero under electric dipole approximation but Electric Field Induced Second Harmonic Generation EFISHG can still be possible because in the case of EFISHG : $P_i(2\omega) = \chi^{(3)}_{ijkl} E_j(\omega) E_k(\omega) E_l(0)$

3 (odd number) polar terms are in play.

For a general discussion of SHG with quadratic EM field dependence, mutual interaction between electric field $\vec{E}$ and magnetic field $\vec{B}$ in a system has to be taken into consideration. Even for centro-symmetric system, second harmonic polarization can be generalized as :

$$P_i(2\omega) = g_{ijkl} E_j \partial_k E_l \tag{1.14}$$

where g_{ijkl} is a 4th rank NLO susceptibility tensor and its tensor components depend particularly on relative size order of system and EM field wavelength (λ), different SHG mechanism and point group symmetry of the system of interest. For example, SHG depending on quadratic EM field in a centro-symmetric system could be magnetic dipole coupling mechanism, magnetic dipole mechanism, electric quadruple mechanism and electric quadruple coupling mechanism[14]. As similar to asymmetric electric dipole oscillation as shown in the previous section, second harmonic polarization P(2ω) from centro-symmetric system due to quadratic charge displacement $\vec{r}(2\omega)$ can be understood preliminarily using classical Lorentz force model[15]:

$$\ddot{\vec{r}}+\gamma\dot{\vec{r}}+\omega_o\vec{r}=\frac{q}{m}\left(\vec{E}+\dot{\vec{r}}\,x\vec{B}\right) \tag{1.15}$$

Where $\vec{E}=E_\omega e^{i(\vec{k}_\omega\bullet\vec{r}-\omega t)}\hat{e}_E+c.c.$ and $\vec{B}=B_\omega e^{i(\vec{k}_\omega\bullet\vec{r}-\omega t)}\hat{e}_B+c.c.$. With the introduction of these expressions of EM field to equation 1.15, quadratic dipolar motion $\vec{r}(2\omega)$ can be calculated which relates to EM field as what we have shown in equation 1.14.

In summary, mechanism of SHG depending quadratically on EM fields could be presented as in table 1.1. However, non-zero components of second order nonlinear susceptibilities due to different mechanisms are attributed completely to point group symmetry[16, 17] of particular system of interest like poled NLO polymers, polar inorganic crystals and macromolecular films. Symmetry properties of non-vanishing components of second order nonlinear susceptibilities will be further discussed in following chapters for different NLO systems.

Quadratic SHG mechanism	P(2ω)~
Electric dipole	$\chi^{(2)}_{ijk} E_j E_k$
Magnetic dipole coupling	$\Gamma_{ijk} E_j H_k$
Electric quadrupole	$-Q_{ij} \partial_j E_k E_l$
Magnetic dipole	$-\frac{c}{2\omega i} \nabla \times \Xi_{ijkl} E_k E_l$
Electric quadrupole coupling	$\Delta_{ijkl} E_j \partial_k E_l$

Table 1.1 Different mechanisms of Second Harmonic Generation which are quadratic EM field dependence

1.3 SHG propagation in NLO media : Oblique incidence

Second order NLO response of system to quadratic EM field was discussed in general in previous section. In this section, we discuss interaction of EM field (ω) with different polarizations (s-polarized and p- polarized) and its SHG (2ω) in NLO medium. 3-layer system as shown below in figure 1.3 is employed as a model for studying EM wave propagations :

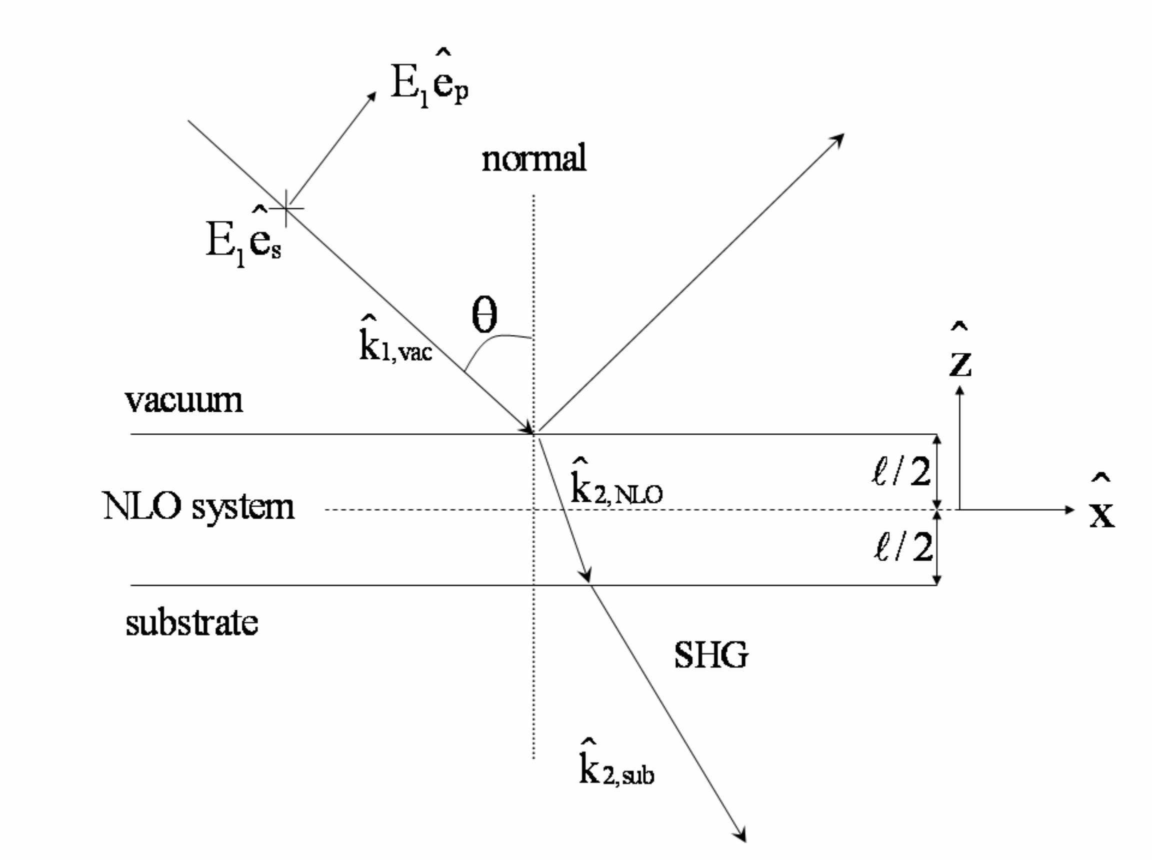

Figure 1.3 Three-layer model of Second Harmonic Generation propagation in nonlinear optical medium

We consider oblique incidence of the fundamental EM field (ω) to isotropic and absorbing NLO material which is of the form

$$\vec{E}_{1v} = \hat{e}_v E_1 e^{i(\vec{k}_1 \cdot \vec{r} - \omega t)} \tag{1.16}$$

where $\hat{e}_v$ = (0,1,0) for v = s (s-polarization), $\hat{e}_v$ = (cosθ,0,sinθ) for v = p (p-polarization), $\vec{k}_1 = \frac{\omega}{c}(\sin\theta, 0, -\cos\theta)$. We construct the EM field of SHG (2ω) at different medium :

Vacuum

$$\vec{E}_{2v} = \hat{e}_v R e^{i(\vec{k}_2^r \bullet \vec{r} - \frac{\ell}{2}\hat{z})} \tag{1.17}$$

where $\vec{k}_2^r = \frac{2\omega}{c}\left(\sin\theta, 0, \cos\theta\right)$, R is the amplitude of the reflected SHG.

NLO system

$$\vec{E}_{2v} = \vec{E}_b e^{i2\vec{k}_1 \bullet \vec{r}} + \hat{e}_{2v}\widetilde{A}e^{i\vec{k}_2 \bullet \vec{r}} \tag{1.18}$$

where $\vec{k}_2 = \frac{2\omega n_2}{c}\left(\sin\theta_2, 0, -\cos\theta_2\right)$, $\widetilde{A}$ is amplitude of free SH EM field and $\vec{E}_b$ is bound SH EM field

$$\vec{E}_b = \frac{4\pi}{n_1^2 - n_2^2}\left(\vec{P}_{NL} - \frac{2\vec{k}_1(2\vec{k}_1 \bullet \vec{P}_{NL})}{\left|\vec{k}_2\right|^2}\right) \tag{1.19}$$

$$\vec{P}_{NL} = P_i(2\omega) = \chi_{ijk}^{(2)} E_j E_k \text{, for i=x,y,z} \tag{1.20}$$

where $\vec{P}_{NL}$ is the nonlinear polarization which acts as a source of interaction (energy exchange) between EM fields of fundamental ω and SHG 2ω fields.

Substrate

$$\vec{E}_{2v} = \hat{e}_{2v}^{sub} T e^{i(\vec{k}_2^{sub} \bullet \vec{r} + \frac{\ell}{2}\hat{z})} \tag{1.21}$$

where T is the amplitude of transmitted SHG, $\vec{k}_2^{sub} = \frac{2\omega n_2^{sub}}{c}\left(\sin\theta_2^{sub}, 0, -\cos\theta_2^{sub}\right)$. Using standard boundary matching of tangential and normal components of EM fields at boundaries (vacuum-NLO system and NLO system-substrate interfaces), power of SHG can be obtained. For example, the solution of SHG from a NLO system possessing $C_{\infty v}$ point-group symmetry is given below in equation 1.22 :

$$P(2\omega)_{v\to p} = \left(\chi^{(2)}_{\mathrm{eff}}\right)^2 P(\omega)_v{}^2 \, \frac{32\pi^3}{cA} \frac{\left[t^{1v}_{vacf}\right]^4 \left[t^{2p}_{fs}\right]^2 \left[t^{2p}_{sa}\right]^2}{n_2{}^2 c_2{}^2} \left(\frac{2\pi\ell}{\lambda}\right)^2 e^{-2(\delta_1+\delta_2)} \, \frac{\sin^2\psi + \sinh^2\phi}{\psi^2+\phi^2} \tag{1.22}$$

where c is the speed of light, A is the area of illumination n_i = refractive index of NLO system at fundamental (i = 1) or SH (i =2) frequency, $c_i = \sqrt{1-\frac{\sin^2\theta}{n_i{}^2}}$ where i = 1 or 2, ℓ is film thickness and δ_i (i = 1 or 2) are absorption of the NLO system at fundamental (ω) or SH (2ω) frequencies. We assume that the NLO system is non-birefrigent. $\left[t^{ij}_{kl}\right]$s are transmission coefficients of fundamental frequency (i = 1) or SH frequency (i = 2) at different polarization state (j = s : s-polarization, j = p : p-polarization) at different interfaces (k or l = vacuum (vac), film (f), substrate (s) or air (a)). $\Psi = \frac{2\pi\ell}{\lambda}\left(n_1c_1 - n_2c_2\right)$ and $\phi = \delta_1 - \delta_2$.

For $C_{\infty v}$ point-group symmetry, there are only 3 non-vanishing second order NLO susceptibilities $\chi^{(2)}_{zzz}$, $\chi^{(2)}_{zxx}$ and $\chi^{(2)}_{xxz}$. They can be all obtained from SHG measurement of s-in/p-out and p-in/p-out configurations.

s-in/p-out

$$\chi^{(2)}_{\mathrm{eff}} = \chi^{(2)}_{zxx}\sin\theta_2 \tag{1.23}$$

p-in/p-out

$$\chi^{(2)}_{\mathrm{eff}} = \chi^{(2)}_{xxz}\cos\theta_2\sin 2\theta_1 + \sin\theta_2\left[\chi^{(2)}_{zxx}\cos^2\theta_1 + \chi^{(2)}_{zzz}\sin^2\theta_1\right] \tag{1.24}$$

For SHG, there is a phase mismatch term $\Psi = \frac{2\pi\ell}{\lambda}\left(n_1c_1 - n_2c_2\right)$ which governs the efficiency of energy exchange between fundamental (ω) and SH generated (2ω) EM fields.

1.4 SHG simulation of two NLO systems

We give two examples of SHG simulation to illustrate the main characteristics of SHG measurement according to SHG equation 1.22 derived.

The first example that we consider is a polar zinc oxide (ZnO) single crystal plate of different thickness with non-vanishing second order NLO susceptibilities : $\chi^{(2)}_{zxx} = \chi^{(2)}_{xzx} = 4\mathrm{pm/V}$ and $\chi^{(2)}_{zzz} = -14\mathrm{pm/V}$ and zero absorbance. Simulation is made for SHG signal measurement with respect to incident angle of EM fields to the normal axis (z-axis) of sample. SHG signal is considered to be measured in transmission mode.

As we can speculate from the SHG simulation that the increase in thickness of polar ZnO crystal, SHG magnitude increases accordingly. In addition, if thickness of ZnO crystal plate increases, there are more and more fringes which are well know as Maker-Fringes[18] of SHG response from NLO material. It emerges when thickness of sample is much higher than its coherence length (for ZnO, coherent length $\frac{\lambda_{2\omega}}{n_{2\omega} - n_{\omega}} \sim 6$ μm). The emergence of Maker-fringes is due mainly to the dispersion of NLO system. Difference of wave propagation speed between fundamental EM field and its SHG EM field in NLO media causes destructive interference of SH EM field and it leads to minimum energy detection (existence of fringes).

ZnO Thickness (μm)	P(2ω) (rel. value)
1	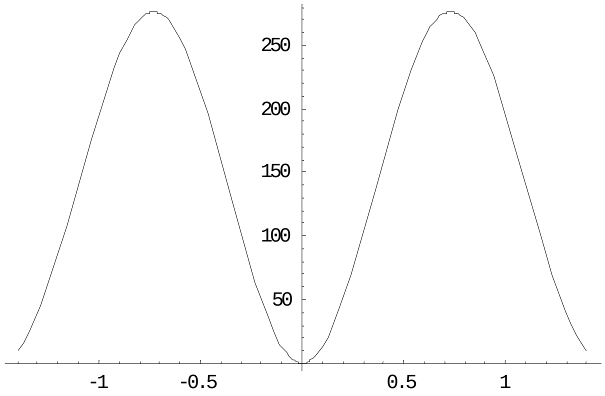
100	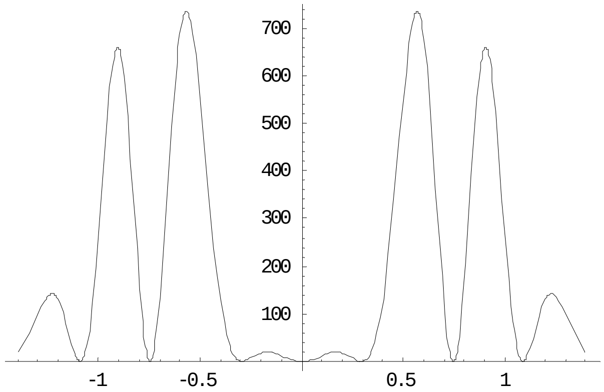
500	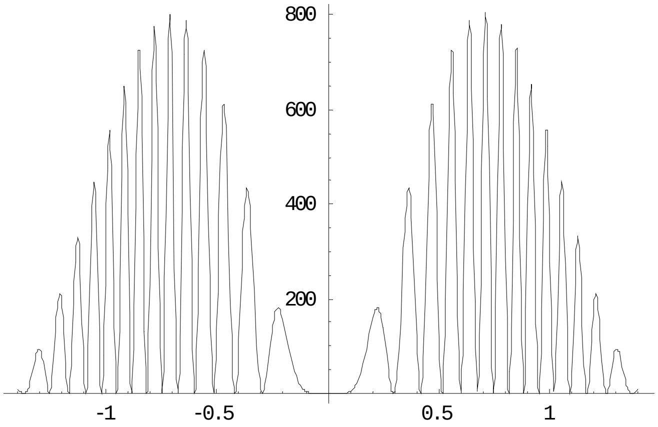
	Incident angle θ(radian)

Figure 1.4 SHG simulation of polar ZnO single crystal of different thickness

Second example is SHG simulation of a poled NLO polymer (PMMA/DR-1) where dye absorption is taken into account in SHG simulation. For moderate electric field poling of NLO polymer ($\mathrm{E} < 100\mathrm{V}\mu\mathrm{m}^{-1}$), $\dfrac{\chi^{(2)}_{zxx}(\text{or } \chi^{(2)}_{xzx})}{\chi^{(2)}_{zzz}} \sim \dfrac{1}{3}$. The parameters of SHG fitting are as the following : film thickness = 1 μm, coherence length = $\dfrac{0.532}{1.496-1.48}$ = 35 μm, $\chi^{(2)}_{zxx} = \chi^{(2)}_{xzx} = 2\mathrm{pm/V}$ and $\chi^{(2)}_{zzz} = 6\mathrm{pm/V}$. The SHG simulations are shown in figure 1.5.

As we see from SHG simulations, the profile of the SH signal with respect to incident angle in all 3 cases is similar because the NLO polymer film thickness is far lower than its coherence length. However, with increasing SH absorption of the NLO system, the amplitude of SHG decreases. It infers that without considering the absorption of NLO system, it is not adequate to estimate correctly its second order NLO effect because absorption of SH signal in the NLO system leads to the under-estimation of actual second harmonic signal intensity being created. In chapter 2, we would study SH response of dye-doped NLO polymers and the consideration of dye absorption in each case of studies would become crucial. In addition, in chapter 3 and chapter 4, second order nonlinear properties of highly absorbing NLO medium (ZnO, C60 and CuPc) will be discussed. Consideration of absorption at SH frequency will become non-negligible for correct interpretation of their second order optical nonlinearities.

<table>
<tr><td>Absorption δ_2 at 532 nm</td><td>P(2ω) (rel. value)</td></tr>
<tr><td>0</td><td>
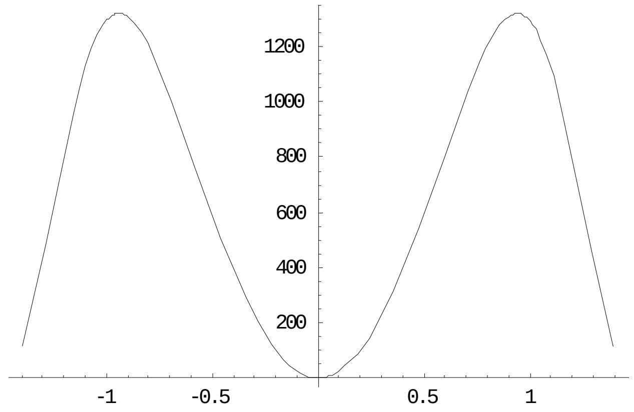

</td></tr>
<tr><td>0.05</td><td>
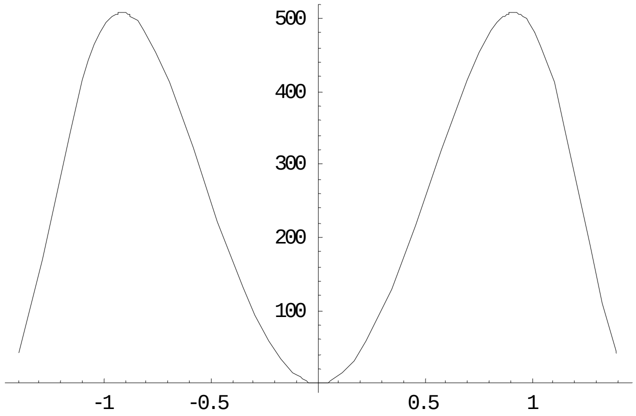

</td></tr>
<tr><td>0.1</td><td>
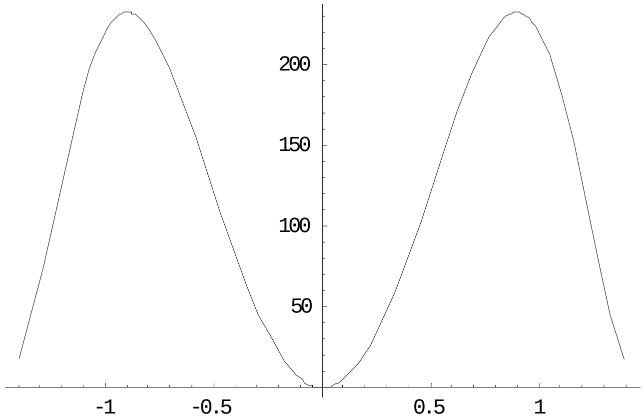

</td></tr>
<tr><td></td><td>Incident angle θ(radian)</td></tr>
</table>

Figure 1.5 SHG simulation of poled NLO polymer of different SH absorption

1.5 Chapter summary

In summary, we reviewed the essential idea for the understanding of nonlinear optical process in NLO system. A classical harmonic oscillator model was given to illustrate the second harmonic radiation from dipolar oscillator. Furthermore, the generality of second order nonlinear optical process existing in electric- & magnetic-sensitive system was addressed. Expression of fundamental and SH EM waves propagation in NLO media in a three-layer model was explained and shown. At last, simulations of SHG in NLO medium with different thickness or different absorption were illustrated to stress on the main feature of SH signal at measurement.

Chapter references

1. A. Yariv, *Quantum Electronics* (John Wiley & Sons, Inc., USA, 1975).
2. D. S. Chemla, "Non-linear optical properties of condensed matter," Reports on Progress in Physics **43**(10), 1191 (1980).
3. T. Verbiest, S. Houbrechts, M. Kauranen, K. Clays, and A. Persoons, "Second-order nonlinear optical materials: recent advances in chromophore design," Journal of Materials Chemistry **7**(11), 2175-2189 (1997).
4. M. Fiebig, D. Frohlich, T. Lottermoser, V. V. Pavlov, R. V. Pisarev, and H. J. Weber, "Second harmonic generation in the centrosymmetric antiferromagnet NiO," Physical Review Letters **8713**(13)(2001).
5. N. N. T. Kim, M. Dumont, J. A. Delaire, and K. Nakatani, "Orientation of azo-dye molecules in polymer films, via photoisomerization: Dichroism measurements and second harmonic generation," Molecular Crystals And Liquid Crystals **430**, 249-256 (2005).
6. S. Sioncke, T. Verbiest, and A. Persoons, "Second-order nonlinear optical properties of chiral materials," Materials Science & Engineering R-Reports **42**(5-6), 115-155 (2003).
7. E. E. Steltz and A. Lakhtakia, "Theory of second-harmonic-generated radiation from chiral sculptured thin films for bio-sensing," Optics Communications **216**(1-3), 139-150 (2003).
8. P. Fischer and F. Hache, "Nonlinear optical spectroscopy of chiral molecules," Chirality **17**(8), 421-437 (2005).
9. M. Kauranen, T. Verbiest, J. J. Maki, and A. Persoons, "Nonlinear optical properties of chiral polymers," Synthetic Metals **81**(2-3), 117-120 (1996).
10. J. D. Byers, H. I. Yee, and J. M. Hicks, "A 2nd-Harmonic Generation Analog Of Optical-Rotatory Dispersion For The Study Of Chiral Monolayers," Journal Of Chemical Physics **101**(7), 6233-6241 (1994).
11. F. Hach, M. C. Schanne-Klein, H. Mesnil, M. Alexandre, G. Lemercier, and C. Andraud, "Nonlinear optical activity in chiral molecules: surface second harmonic generation and nonlinear circular dichroism," Comptes Rendus Physique **3**(4), 429-437 (2002).
12. G. J. Simpson, "Structural origins of circular dichroism in surface second harmonic generation," Journal Of Chemical Physics **117**(7), 3398-3410 (2002).
13. J. D. Byers, H. I. Yee, T. Petralli-Mallow, and J. M. Hicks, "Second-harmonic generation circular-dichroism spectroscopy from chiral monolayers," Physical

Review B **49**(20), 14643 (1994).

14. H. Hoshi, T. Yamada, K. Ishikawa, H. Takezoe, and A. Fukuda, "2nd-Harmonic Generation In Centrosymmetric Molecular Films - Analysis Under Anisotropic Conditions," Physical Review B **52**(16), 12355-12365 (1995).
15. E. Adler, "nonlinear optical frequency polarization in a dielectric," Physical Review **134**, A728 (1964).
16. Y. R. Shen, "Permutation Symmetry of Nonlinear Susceptibilities and Energy Relation," Physical Review **167**(3), 818 (1968).
17. R. W. Boyd, *Nonlinear Optics* (Academic Press, Inc., 1992).
18. P. D. Maker, R. W. Therhune, M. Nisenoff, and S. C. M., "Effects of Dispersion and Focusing on the production of optical harmonics," Physical Review Letters **8**(1), 21-23 (1962).

CHAPTER 2
SECOND HARMONIC GENERATION OF AZO-DYE NONLINEAR OPTICAL GLASSY POLYMER

In this chapter, Second Harmonic Generation (SHG) would be developed as a diagnostic tool for studying second order nonlinear optical (NLO) properties of azo-dye glassy polymer. As we have already mentioned in chapter 1 that most of the azo-dye doped/functionalized glassy polymers are intrinsically centro-symmetric due to thermodynamic orientation randomization of azo-dye molecules which is contrary to the cases of azo-dye in non-glassy polymers like ferroelectric and liquid crystalline polymer. For azo-dye glassy polymer, centro-symmetry can be broken by various methods of poling like Thermal-Assisted electric field Poling (TAP)[1], Corona Poling (CP)[2-4], Photo-Assisted Poling (PAP)[5-7] and All-Optical Poling (AOP)[8-18]. In the following section, poling techniques for centro-symmetric NLO azo-dye glassy polymer will be introduced.

2.1 Poling of azo-dye glassy amorphous polymer

2.1.1 Poling by external electric field

An external static electric field (E), which is polar in nature, is applied in TAP, CP or PAP to orientate dipole molecules (azo-dye in our case) in a polymer matrix as shown in figure 2.1 below. This breaks centro-symmetry of the NLO system. Macroscopic second order NLO susceptibilities $\chi^{(2)}_{ijk}$ are related to molecular NLO hyperpolarizability β_{IJK} in the following relation :

$$\chi^{(2)}_{ijk} = N\left\langle \beta^{*}_{IJK} \right\rangle_{ijk} \tag{2.1}$$

where N is the total number of NLO molecules in system, i,j,k are laboratory coordinates and I,J,K are molecule coordinates. Local electric field factor β^{*} can be included for precise calculation. With transformation matrix connecting laboratory and molecule coordinate systems, equation 2.1 can be written as :

$$\chi^{(2)}_{ijk} = N\beta^{*}_{IJK} \left\langle a_{iI} a_{jJ} a_{kK} \right\rangle \tag{2.2}$$

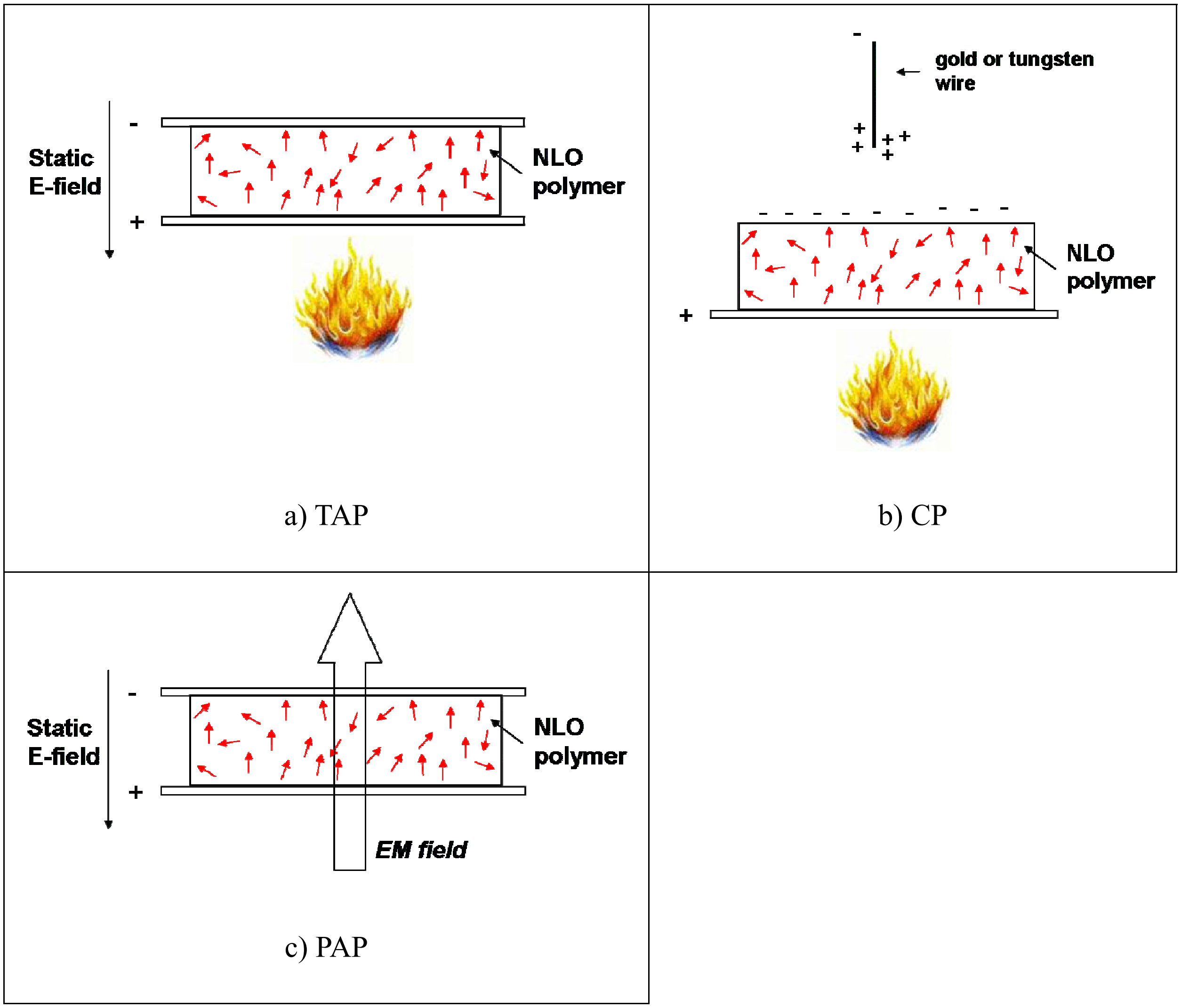

a) TAP

b) CP

c) PAP

Figure 2.1 Schematic diagrams of three poling methods : a) Thermal-Assisted Poling TAP b) Corona Poling CP c) Photo-Assisted Poling PAP

Applying external static electric field along laboratory z-axis $\vec{E}$, ensemble average of transformation matrix can be written as :

$$\left\langle a_{iI}a_{jJ}a_{kK}\right\rangle = \int a_{iI}a_{jJ}a_{kK}G(\Omega,E)d\Omega \qquad (2.3)$$

and $G(\Omega,E)$ is the Boltzmann orientation distribution function :

$$G(\Omega,E) = \frac{e^{\frac{-(U-\vec{\mu}\bullet\vec{E})}{kT}}}{\int e^{\frac{-(U-\vec{\mu}\bullet\vec{E})}{kT}}d\Omega} \qquad (2.4)$$

where U is the interaction energy of dipolar molecule with the environment (such as dipole-dipole interaction between azo-dye and polar group of polymer chain), $\vec{\mu}$ is dipole moment of molecule, kT is the Boltzmann factor. For glassy amorphous polymer that we study, interaction energy U of dipolar molecules to their environment is negligible. However, for ferroelectric host[19, 20] or liquid crystal host[21-23], dipolar molecules are aligned intrinsically in the matrix and so, potential energy variation $U(\Omega)$ due to molecular rotation has to be taken into account significantly for correct estimation of the thermo-dynamical distribution factor under the introduction of external electric field $\vec{E}$ for molecule alignment.

Spherical coordinate system as shown in figure 2.2 is employed for the description of molecular orientation during poling.

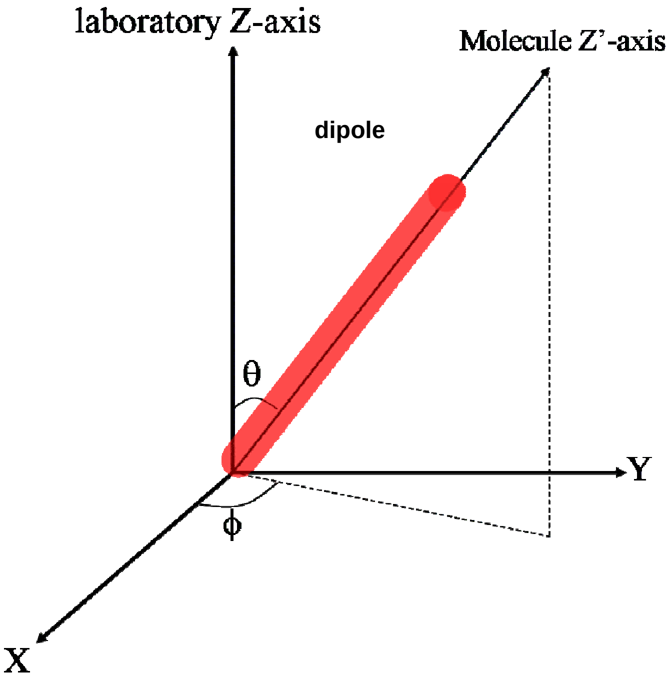

Figure 2.2 Spherical coordinate representation of orientation direction of a rod-like dipolar molecule

Assuming that molecules are one-dimensional rod-like with only one non-vanishing hyperpolarizability $\beta_{z'z'z'}$ and their orientation possess azimuthal symmetry along laboratory z-axis. Boltzmann orientation distribution function can be further simplified by using Legendre polynomial expansion :

$$G(\Omega, E) = G(\theta, E) = \sum_{0}^{\infty} \frac{2\ell + 1}{2} A_{\ell} P_{\ell}(\cos\theta) \tag{2.5}$$

For moderate external applied static electric field ($E<100V\mu m^{-1}$), the exponential distribution factor can be approximated to

$$e^{-\frac{(U-\vec{\mu}\bullet\vec{E})}{kT}} \approx \left(1 + \frac{\vec{\mu}\bullet\vec{E}}{kT}\right) e^{-\frac{U}{kT}} \tag{2.6}$$

If centro-symmetric NLO polymer is poled by any one of the poling methods described in figure 2.1, its centro-symmetry will be broken and it possesses $C_{v\infty}$ point group symmetry. For NLO system with $C_{v\infty}$ point group symmetry, there are 3 non-vanishing second order NLO susceptibilities $\chi^{(2)}_{zxx}$, $\chi^{(2)}_{xzx} \sim \chi^{(2)}_{zxx}$ and $\chi^{(2)}_{zzz}$. They can be expressed as follow under the lowest order approximation :

$$\chi^{(2)}_{zzz} \sim N \frac{\beta_{z'z'z'} \mu_{z'} E}{5kT} \tag{2.7a}$$

and

$$\chi^{(2)}_{zxx} \text{ or } \chi^{(2)}_{xzx} \sim N \frac{\beta_{z'z'z'} \mu_{z'} E}{15kT} \tag{2.7b}$$

This simplified results of second order NLO susceptibilities due to external static electric field alignment gives us an insight to the relation of NLO susceptibilities to physical properties of the systems being studied. For the $\chi^{(2)}$ estimations as shown in equation 2.7, third order nonlinear optical contribution to $\chi^{(2)}$ due to second order molecular hyperpolarizability γ is not included. According to $\chi^{(2)}$ approximation as indicated in equation 2.7a and 2.7b, for poling of moderate electric field strength, ratio of $\chi^{(2)} \rightarrow \frac{\chi^{(2)}_{zxx}}{\chi^{(2)}_{zzz}}$ is close to $\frac{1}{3}$ which is regarded as a characteristic value related to the external static electric field poling. The result will be further applied for understanding

NLO susceptibilities of layer-by-layer (LBL) self-assembly NLO polymer.

2.1.2 All-optical poling (AOP)

Unlike poling mediated by external static electric field as described in the above section, for All-Optical Poling (AOP), centro-symmetry breaking of NLO system is brought by the interference of fundamental EM wave frequency[24] (ω) and its second harmonic EM wave frequency (2ω) as shown in figure 2.3. Second order NLO susceptibility $\chi_{ind}^{(2)}$ can be expressed as :

$$\chi_{ind}^{(2)} \sim \left\langle \left(E_{\omega}(\vec{r},t) + E_{2\omega}(\vec{r},t) \right)^3 \right\rangle_t \tag{2.8}$$

If we consider that EM waves co-propagate in z-direction and they are polarized in y-direction, induced second order NLO susceptibility $\chi_{ind}^{(2)}(z)$ can be expressed as :

$$\chi_{ind}^{(2)}(z) = \chi_{eff}^{(2)} \cos(\Delta k \bullet z + \Delta\Phi) e^{-\frac{\alpha}{2}z} \tag{2.9}$$

where $\Delta k = 2k_{\omega} - k_{2\omega}$ is the phase mismatch factor, $\Delta\Phi$ is the relative phase difference between fundamental EM field and second harmonic EM field and α is the absorption coefficient at SH frequency (We assume that the system does not absorb at fundamental frequency). One of the important characteristic of second order NLO susceptibility induced by AOP is that $\chi_{ind}^{(2)}$ is a second order grating which possesses a phase-matching periodicity of Δk. Phase mismatch of second harmonic (SH) EM field and fundamental EM field can be solved because this grating feature. Efficiency of SHG is maximized in AOP case due to the fulfillment of perfect phase-match of the propagation of fundamental and SH EM fields in the NLO medium.

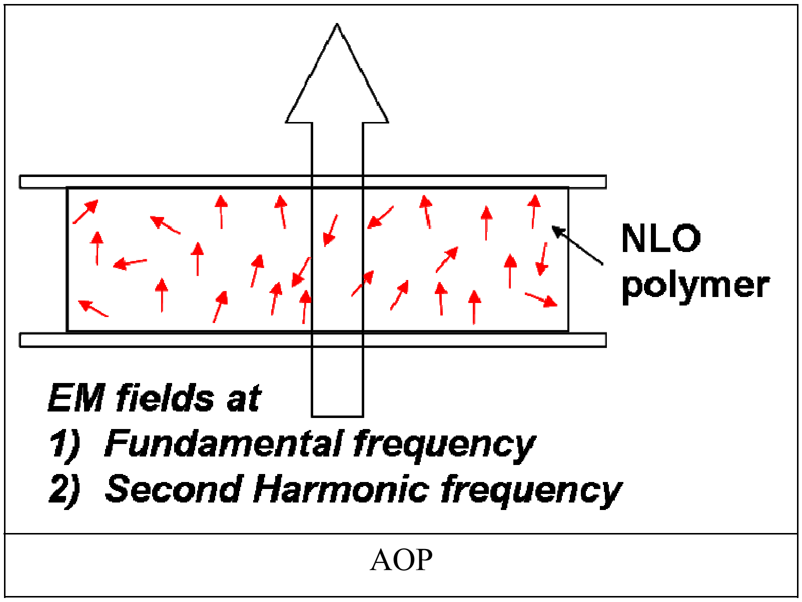

Figure 2.3 All-Optical Poling AOP

2.2 Orientation of molecules in polymer system

We have discussed various mechanisms for the introduction of second order optical nonlinearity by centro-symmetry breaking (Poling) of NLO system. However, efficiency of molecular reorientation in polymer matrix by different poling techniques varies due to the rigidity of glassy polymer at different temperature with reference to its glass transition temperature[25, 26] (T_g). Generally speaking, for amorphous glassy polymer, viscosity (η) decreases with decreasing polymer temperature. It can be understood by the specific volume variation in polymer above and below glass transition temperature T_g as shown in figure 2.4.

Glass transition temperature T_g is a second order thermal effect which indicates the temperature at which there is a state transition (from melt state to glassy state) in polymer matrix. It is commonly determined by Differential Scanning Calorimetry (DSC). Decreasing polymer temperature from viscous flow state to glassy state on passing through the glass transition temperature T_g, specific volume (free volume) decreases which in turn, increases viscosity of polymer matrix. At viscous flow state, polymer viscosity $\eta(T)$ follows satisfactorily to Williams-Landel-Ferry (WLF)[27, 28] relation :

$$\eta(T) = \eta_o e^{-\frac{C_1(T-T_g)}{C_2+(T-T_g)}} \qquad (2.10)$$

where $C_{1,2}$ are material constants and η_o is viscosity of polymer at T_g. Temperature is measured in Kelvin. However, at glassy state, temperature dependence to polymer viscosity is still a controversial issue.

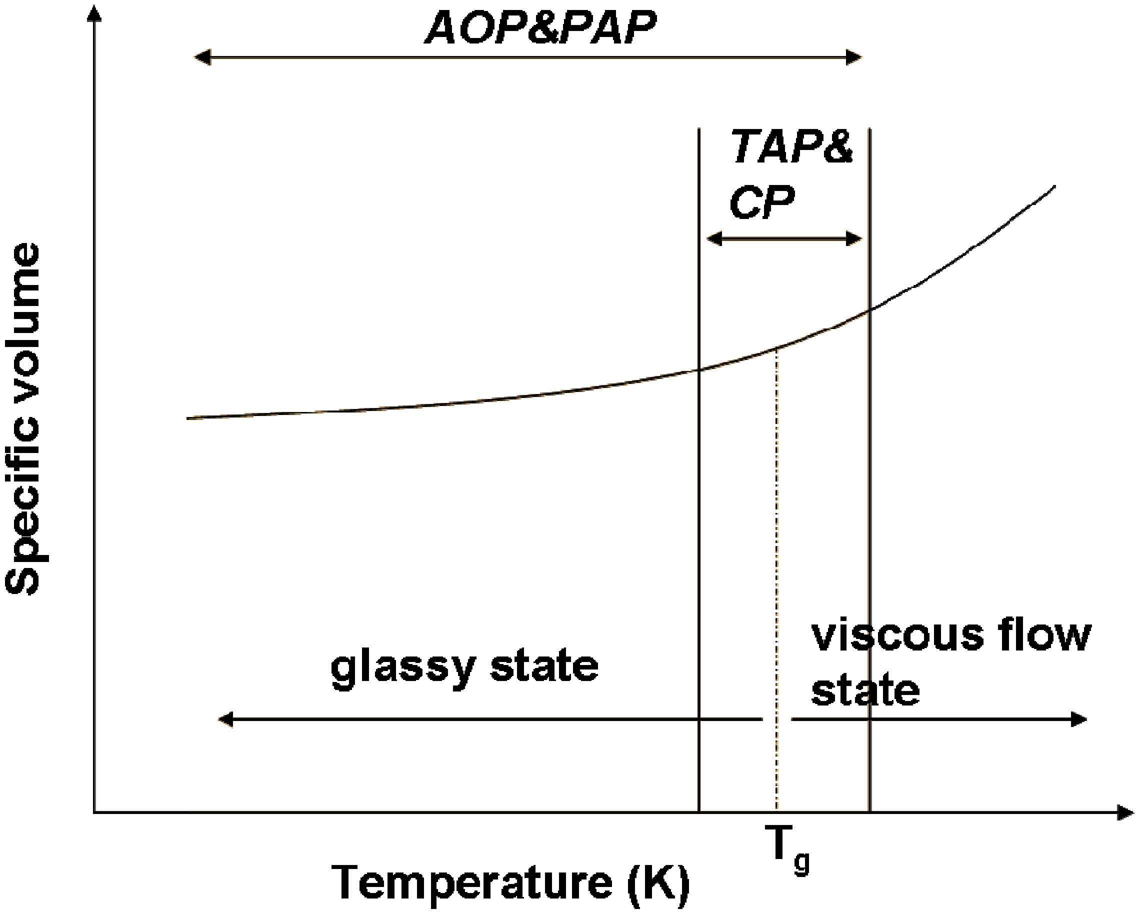

Figure 2.4 Specific volume (viscosity) change of polymer with respect to temperature

Some researchers[29] believe that under T_g, polymer viscosity follows non-Arrhenius-type relation (Vogel-Fulcher equation) :

$$\eta(T) = \eta_o e^{-\frac{K}{T_o - T}} \tag{2.11}$$

where K is material constant and $T_o \sim T_g+50$ (in Kelvin unit). On the other hand, some other researchers[30, 31] suggest that it follows Arrhenius relation :

$$\eta(T) = \eta_o e^{-\frac{E_a}{RT}} \tag{2.12}$$

where E_a is the activation energy and R is the gas constant. Disregarding the validity of the models which are more satisfactory for describing relation between polymer viscosity and its temperature, it is clear that polymer viscosity increases when its temperature decreases though its dependence to temperature might be varied due to particular chemical and structural properties of polymer being studied.

Efficiency of the reorientation of dye molecules at TAP and CP is boosted up at temperature close to T_g as rotational constraint imposed by polymer matrix to dye molecules diminishes at higher temperature. It is shown below in figure 2.4 above that when polymer temperature increases, polymer viscosity η decreases accordingly. Poled polymers are cooled down under continuous application of electric field so as to freeze the alignment of dye molecules at rigid glassy polymer state. However with PAP and AOP, azo-dye molecules can be reorientated with high efficiency even in glassy state at low temperature the nature of its trans-cis-trans photo-isomerization[32] mechanism (as shown in figure 2.5). At 2-photon OR one-photon absorption, 'rotary motion' of dye molecules at their trans-cis-trans conformational changes facilitates their reorientation process during noncentro-symmetric orientational hole-burning (AOP) OR in the presence of external electric field (PAP).

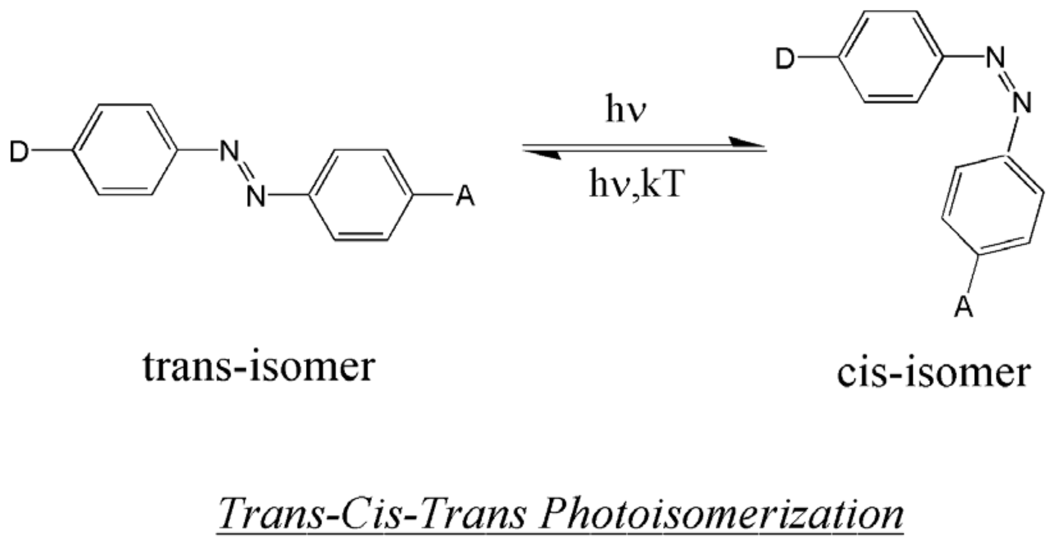

Figure 2.5 Photoisomerization of a push-pull azo-dye molecule

In the following section, AOP is developed as a tool for the investigation of the non-perturbated orientation/rotation mechanism of azo-dye guest molecules in different amorphous glassy polymers with different rigidity (Guest-Host (GH) NLO azo-polymers). It has an advantage over the poling techniques (as for TAP or CP), which involve external static electric field, because asymmetric charge injection during poling[33, 34] would disturb the studies of free orientation/rotation mechanism of molecules in a polymer matrix.

2.3 Orientation relaxation of azo-dye doped amorphous polymers upon AOP

2.3.1 Sample preparation

Disperse Red 1 (DR-1, insert in figure 2.6a) was incorporated at 4.5% by weight into 3 amorphous glassy polymer matrices with different glass transition temperature (T_g) as shown in figure 2.6b : poly(methyl methacrylate) (PMMA, $M_w = 34000$ g, $T_g \sim 114$°C), poly(carbonate) (PC, $M_w = 64000$ g, $T_g \sim 149$°C), poly(sulfone) (PSU, $M_w = 56000$ g, $T_g \sim 190$°C). All chemicals were purchased from Aldrich. Polymer solutions of 10% by volume in chloroform solution were spin-coated onto glass substrate to obtain polymer films of thickness 0.7 μm, as measured with Dektak 6m stylus profilometer. As shown in figure 2.6a, optical densities (O.D.) of the samples at $\lambda = 532$ nm were about 0.7 as measured by Perkin Elmer Lambda 19. After being spin-coated, samples were kept at temperature of around 130°C for several hours in order to remove completely the residual solvent. For PC/DR-1 and PSU/DR-1 samples, they were not heated up to temperature above their glass transition temperature ($T_g \sim 149$°C and 190°C respectively) as high temperature leads to sublimation of DR-1 at polymer hosts.

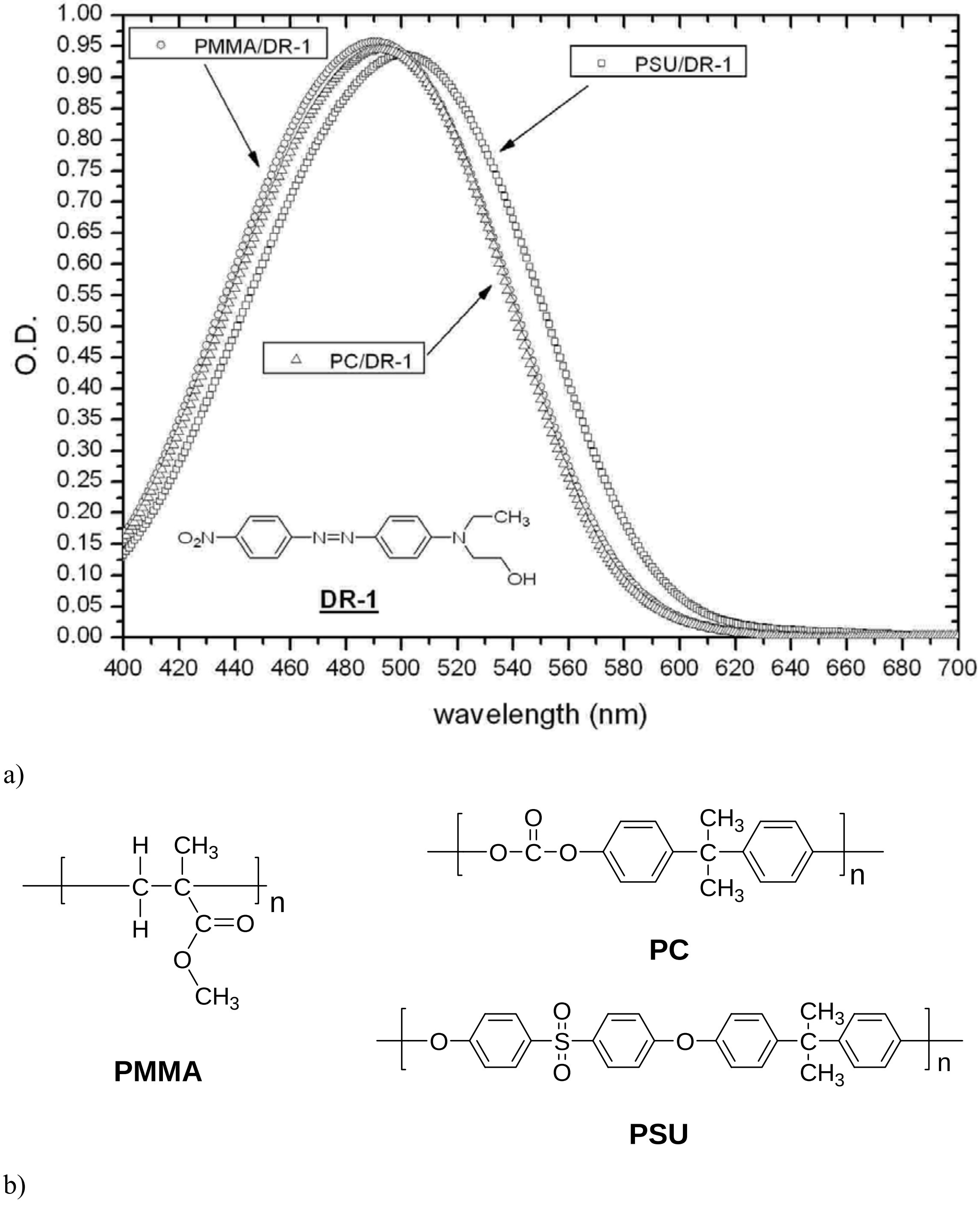

igure 2.6 a) Absorption spectrum of the samples and structure of DR-1; b) Chemical structures of the glassy polymer hosts

2.3.2 All-Optical Poling (AOP) experiment

All-optical poling (AOP) is the registration of a quasi-permanent phase-matched second order optical nonlinearity by photo-excitation using the interference between fundamental and the second harmonic (SH) EM fields : it gives $\chi^{(2)}$ which is proportional to $<\mathbf{E}^3(z,t)>_t$. A Q-switched Nd:YAG laser (Quantel YG-580) giving coherent fundamental (ω = 1064 nm) and second harmonic SH (2ω = 532 nm) pulses (10 Hz, pulse width ~ 8ns) was used in this study. Pulse energies at fundamental (ω) and SH (2ω) wavelengths are 15 mJ and 5 μJ respectively (Area of illumination ~ 0.4 mm^2) and are at p-polarization. A schematic diagram of AOP is shown in figure 2.7.

Samples were mounted onto a 30 isosceles prism during AOP. During the 'Poling' phase, coherent fundamental (ω) and SH (2ω) EM fields are sent to the sample. A quasi-permanent second-order optical nonlinearity $<\chi^{(2)}>$ grating is inscribed in the sample by angular selective photo-excitation of the azo-dye molecules. The second-order optical nonlinearity $<\chi^{(2)}>$ is then monitored during the 'Probing' phase. Second harmonic generation (SHG) from the inscribed $<\chi^{(2)}>$ is then registered by a photomultiplier tube (PMT, Hamamatsu R1828). The SH signal is further processed by an oscilloscope (Tektronix TDS3000B). Growth and relaxation of $<\chi^{(2)}>$ during and after AOP were studied at different temperatures isothermally. Derivation of $<\chi^{(2)}>$ can be referred to appendix I.

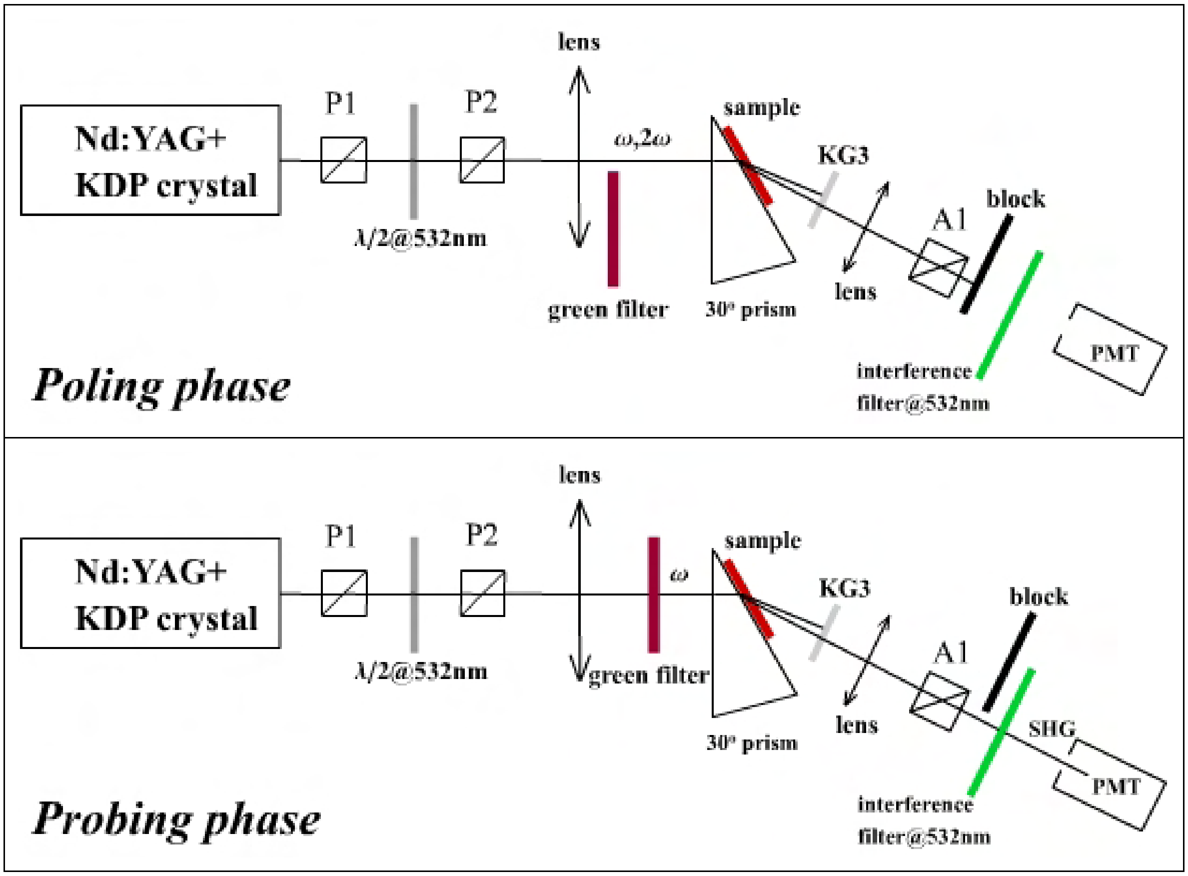

Figure 2.7 Schematic diagrams of All-Optical Poling (AOP) at two stages :
Poling phase and Probing phase

2.3.3 Results of AOP growth and relaxation

$\left\langle \chi^{(2)}_{(0)} \right\rangle_{t'}$ growth at room temperature (RT) for PMMA/DR-1, PS/DR-1 and PSU/DR-1 during AOP is shown in figure 2.8. Saturation of $\left\langle \chi^{(2)}_{(0)} \right\rangle_{sat}$ is reached after 60-80 minutes of AOP. Decay of normalized second-order NLO susceptibility at RT in the 3 samples $\left\langle \chi^{(2)}_{(t)} \right\rangle_{t'}$(norm) after *t*’ [min] of AOP is shown in figure 2.8 as well. At the time scale of our experiment, it can practically be fitted with the bi-exponential decay function :

$$\left\langle \chi^{(2)}_{(t)} \right\rangle_{t'}(\text{norm}) = ae^{-t/\langle\tau\rangle_1} + (1-a)e^{-t/\langle\tau\rangle_2} \tag{2.13}$$

where a is the relative weight between slow and fast components with decay time constants $\langle\tau\rangle_1$ and $\langle\tau\rangle_2$, respectively. The AOP growth and decay was studied in the 3 polymers at room or at elevated temperatures. The bi-exponential decay fitting parameters are given in table 2.1. Precision in the decay times is evaluated to ±20%.

In another experiment, two identical samples of PMMA/DR-1 were previously heated up to T_g and cooled down to room temperature at the rates of 20 °C/hour and 1000 °C/hour respectively. They were subsequently oriented by AOP and the decay was studied at RT. We did not measure any difference in their decay rate. It shows that the cooling history of polymer from the viscous flow state to the glassy state does not affect the AOP relaxation profile of samples which is opposite to the case of electric field poled NLO polymers. For NLO polymer poled under external electric field, thermal (heating or cooling) history of electrically poled NLO polymer affects significantly the $<\chi^{(2)}>$ free relaxation[35, 36].

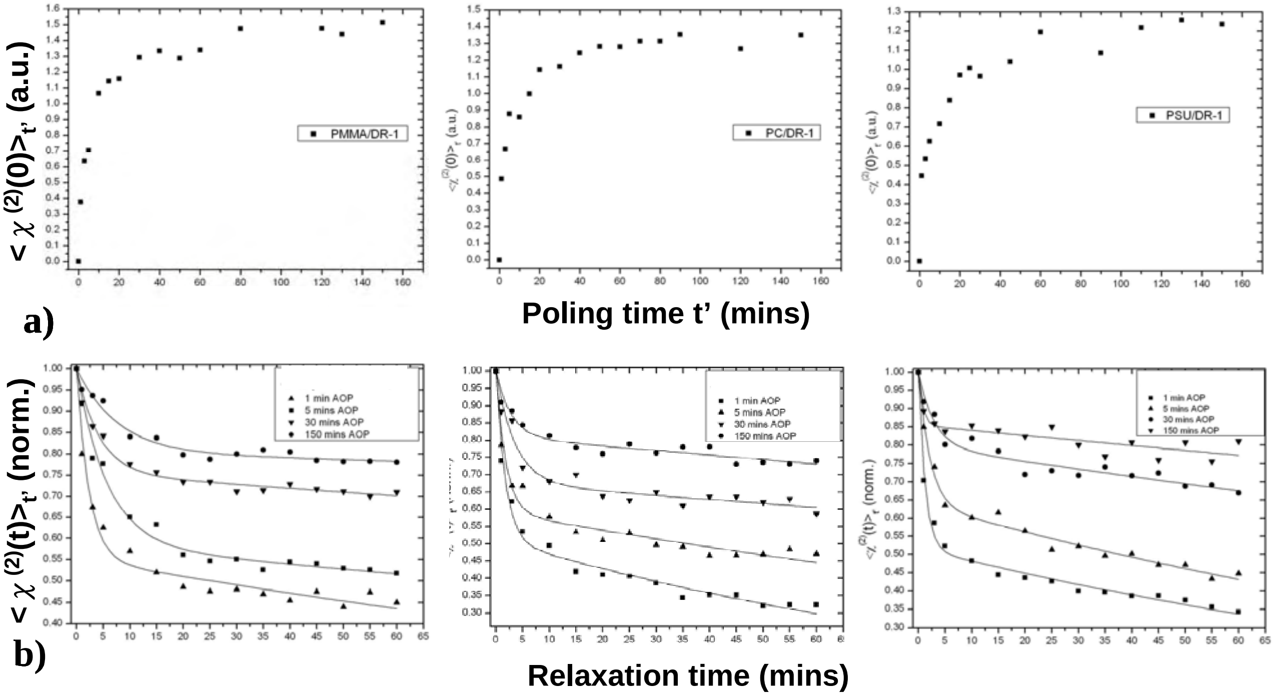

Figure 2.8 Growth of AOP $<\chi^{(2)}(0)>_{t'}$ (a) and normalized dark relaxation $<\chi^{(2)}(t)>_{t'}$ (b) of the samples for different poling durations t'

t’ (min)	a	$\langle\tau\rangle_1$ (min)	$\langle\tau\rangle_2$ (min)	a	$\langle\tau\rangle_1$ (min)	$\langle\tau\rangle_2$ (min)
	20°C PMMA/DR1(T$_g$~110˚C)			**66°C PMMA/DR1(T$_g$~110˚C)**		
1	0.55	255	2.3	0.32	26	0.67
5	0.58	477	5.7	0.46	19	0.78
30	0.75	802	4.1	0..48	64	2.85
150	0.8	2267	7.6	0.55	117	4.08
	20°C PC/DR1(T$_g$~150˚C)			**60°C PC/DR1(T$_g$~150˚C)**		
1	0.51	110	1.7	0.34	38	2.34
5	0.59	208	1.8	0.5	52	1.08
30	0.67	536	3.5	0.42	210	5
150	0.81	576	2.8	0.74	216	3.8
	20°C PSU/DR1(T$_g$~190˚C)			**80°C PSU/DR1(T$_g$~190˚C)**		
1	0.51	140	0.78	0.35	131	6
5	0.64	151	2.8	0.42	149	3
30	0.8	355	2.1	0.65	77	1
150	0.85	596	1.24	0.7	170	1.5

Table 2.1 Bi-exponential decay fitting coefficients for the normalized $\left\langle \chi^{(2)}_{(t)} \right\rangle_{t'}$ decay of the polymers after different AOP durations t’. AOP and decay were performed at room and elevated temperature for the 3 NLO polymers : PMMA/DR1, PC/DR1 and PSU/DR1

2.3.4 Non-Debye rotational relaxation

The second order NLO susceptibility $\chi^{(2)}$ is proportional to the 1st and 3rd order parameters $P_l(\cos\theta)$[37-39]. Decay of $\chi^{(2)}$ directly reflects the orientation relaxation of azo-dyes. According to the experimental decay of the normalized $\left\langle \chi^{(2)}_{(t)} \right\rangle_{t'}$ shown in Figure 2.8b for the 3 different guest-host polymers, the longer the AOP duration t', the slower the $\chi^{(2)}$ decay rate $\left\langle \tau \right\rangle_1^{-1}$. It reveals that orientation relaxation of azo-dyes is retarded upon prolonged duration of AOP. Interestingly, table 2.1 shows that the retardation of orientation relaxation is independent to the poling temperature but it depends on the poling duration.

One might try to understand the retardation of the rotational relaxation during AOP as follow : Azo-dyes, which are located at more viscous local environment, orientate much more slower in the photo-isomerization process during AOP. The longer time the poling, the more 'stable' orientation of azo-dyes is achieved, which in turn relax much slower during the dark relaxation. We believe that, to a certain extent, the above statement is correct. However, would the change of dipolar rotational relaxation upon different poling duration (t') be so significant comparing to the experimental result? We compare our results of the rotational relaxation of PMMA/DR-1 to the Debye-type rotational diffusion model[40] which implies that the rotational motion of molecules in the environment is in random manner (an non-directional rotational diffusion). Uncorrelated rotational jump[41] will not be considered in our discussion.

Considering that there is a broad distribution of rotational relaxation constant[42, 43] D inside an amorphous polymer, which can be due to polymer density fluctuation, local free volume variation, polymer crystallinity. If the distribution of rotational relaxation constant D do not change during AOP and relaxation, the inscribed second order nonlinear susceptibility $<\chi^{(2)}(0)>_{t'}$ being measured can be, to the first-order approximation, expressed as :

$$< \chi^{(2)}(0) >_{t'} \propto \int_D \int_{\Delta\Phi} A(\Delta\Phi, D)[1 - me^{-JDt'}]d\Delta\Phi dD \qquad (2.14)$$

where $\Delta\Phi$ is the spatial averaging between fundamental and second harmonic EM fields inside sample. Dipolar rotational relaxation after saturation can be expressed as :

$$<\chi^{(2)}(t)>_{sat.} \propto \int_D \int_{\Delta\Phi} A(\Delta\Phi, D) e^{-JDt} d\Delta\Phi dD \qquad (2.15)$$

where t' is the time of AOP, $A(\Delta\Phi, D)$, *m*, *J* are the coefficients depending respectively on the azo-dye population with different rotational relaxation *D*, pumping energies, quantum yield of photo-sxcitation, dipole moment and hyperpolarizability. Thermal orientation diffusion is the only orientation randomization process being considered :

$$\frac{\partial N(\Omega, t)}{\partial t} = D\nabla^2 N(\Omega, t) \qquad (2.16)$$

where $N(\Omega,t)$ is the number of dipole at solid angle Ω, D is the thermal diffusion constant (min). Combining equation 2.14 and equation 2.15, the relaxation of inscribed second order nonlinear susceptibility $<\chi^{(2)}(t)>_{t'}$ can be written as :

$$<\chi^{(2)}(t)>_{t'} = <\chi^{(2)}(t)>_{sat.} - \frac{[<\chi^{(2)}(0)>_{sat.} - <\chi^{(2)}(0)>_{t'}]}{<\chi^{(2)}(t')>_{sat.}} <\chi^{(2)}(t+t')>_{sat.} \qquad (2.17)$$

We fit the experimental results of $<\chi^{(2)}(t)>_{t'}$ relaxation of PMMA/DR1 after t'=1 min of AOP with bi-exponential decay model as shown in equation 2.13. The result is shown in figure 2.9. By employing the bi-exponential decay fit of $<\chi^{(2)}(t)>_{1\ mins}$, the growth of $<\chi^{(2)}(0)>_{t'}$ during AOP (as shown in figure 2.8a) and equation 2.17, we model the relaxation profile of $<\chi^{(2)}(t)>_{t'}$ for t'>1 min. Here we make an assumption that for ultra-short duration of AOP (1 min), effective structural modification of polymer matrix by successive photoisomerization cycle of azo-dyes is comparably insignificant and so, the distribution of rotational relaxation time constant D in polymer before and after 1-min AOP would be identical. The comparison of the modeling and the experimental results of $<\chi^{(2)}(t)>_{t'}$ relaxation for t'=1,5,30 and 150 mins is shown in figure 2.9. It is clear that the longer the time (t') of AOP, the larger the deviation of $<\chi^{(2)}(t)>_{t'}$ relaxation to the Debye-type dipole relaxation model for PMMA/DR-1. For PC/DR-1 and PSU/DR-1, such deviation between Debye-type relaxation and experimental $<\chi^{(2)}(t)>_{t'}$ relaxation is also observed. It is obvious that Debye-type dipole relaxation would not be sufficient to explain the retardation of dipolar rotational relaxation upon AOP in guest-host amorphous polymeric system with different rigidity.

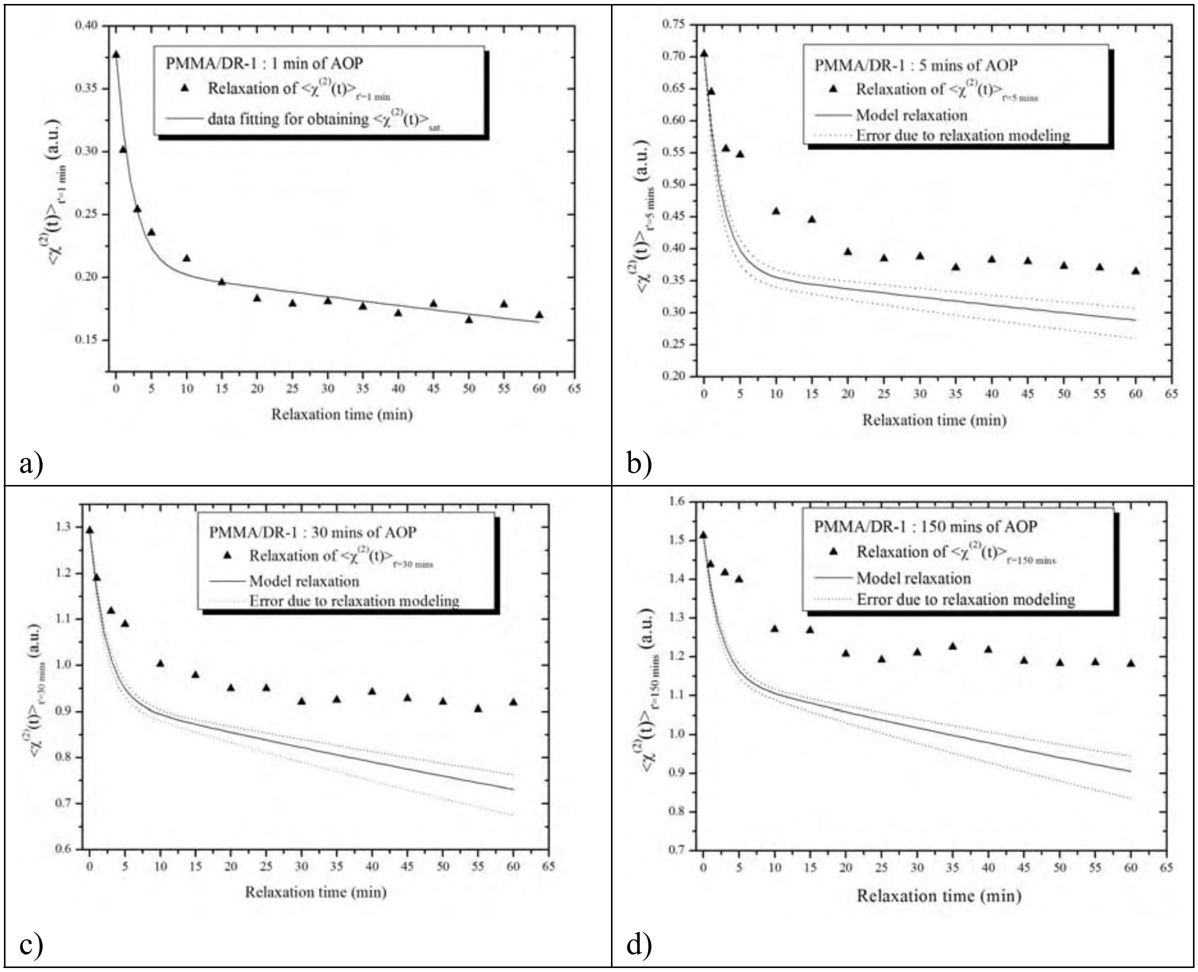

Figure 2.9 $<\chi^{(2)}(t)>_{t'}$ relaxation and their Debye rotational relaxation fittings (according to equation 2.17) of PMMA/DR-1 at room temperature (RT)

2.3.5 Polymer rigidity to $\chi^{(2)}$ relaxation upon AOP

Glass transition temperature (T_g) is always regarded as an indicator of the rigidity of polymer host. High T_g polymers are always used as host for guest dye molecules in order to increase stability of the induced $\chi^{(2)}$[44]. However, referring to table 2.1, the increase of the slow decay constant $<\tau>_1$ upon AOP of PMMA/DR-1 is far higher than that of PC/DR-1 and PSU/DR-1, though PMMA/DR-1 has the lowest T_g among them. It indicates that the retardation of the orientation relaxation upon AOP is not solely related to first order α-relaxation. Second (β-relaxation) or higher order localized segmental polymer motions would be responsible for the hardening of the local polymeric environment surrounding the azo-dyes upon AOP. In order to justify the above argument, we studied the $<\chi^{(2)}(t)>_{t'}$ relaxation of DR-1 doped poly(styrene) (PS/DR-1) upon different duration (t') of AOP at room temperature (RT). Results of bi-exponential function decay fitting and structure of poly(styrene) are shown in the table 2.2 and the figure 2.10 below :

t' (min)	a	$<\tau>_1$(min)	$<\tau>_2$(min)
	PS/DR-1(T_g~100°C)		
1	0.6	**67**	0.7
5	0.58	**68**	0.47
30	0.66	**56**	0.43
150	0.73	**109**	0.4

Table 2.2 Bi-exponential decay fitting of $<\chi^{(2)}(t)>_{t'}$ relaxation upon different durations of AOP

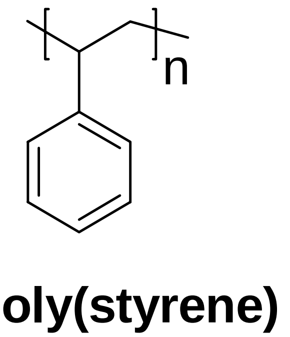

Figure 2.10 Chemical structure of poly(styrene) (PS)

Comparing $<\chi^{(2)}(t)>_{t'}$ relaxation of PS/DR-1 (table 2.2) and PMMA/DR-1 (table 2.1) upon different AOP duration (t') at room temeperature (RT), it is interesting to note that although they have similar T_g (100°C-110°C), their $<\chi^{(2)}(t)>_{t'}$ relaxation behavior are quite different. Thermal orientation diffusion of the dye molecules is much faster in PS host than that in PMMA host. We attribute this to the existence of highly polar ester groups at PMMA side chains which are efficiently rearranged during competitive polymeric expansion and shrinkage induced by the photo-isomerization upon 2-photon and 1-photon absorption at AOP. As a result, the thermal orientation diffusion of dye molecules is tremendously hindered in highly stable and ‘densified’ polymeric environments.

2.3.6 Generality of retardation of dipolar orientation relaxation

AOP is widely studied because it can be employed to different kinds of materials including octupolar[45] and ionic ones[46]. Furthermore, NLO properties can be patterned and controlled microscopically by adjusting the relative polarizations of the fundamental and second harmonic (SH) electromagnetic (EM) fields. However, it is currently believed that the stability of AOP-induced optical nonlinearity, which arises with the aid of selective angular dye excitation in successive photo-isomerization cycles, is lower than that induced by other poling techniques because there is local volumetric expansion[43] during photo-induced trans-cis-trans isomerization of azo-dye. Reversible photo-isomerization cycle of an azo-dye is shown in figure 2.5.

Volumetric expansion brought by the photo-isomerization would increase the free volume (or decrease the viscosity) in the local environment of the azo-dye which in turn, leads to a faster thermal orientational relaxation of azo-dyes upon AOP. Dye-functionalized crosslinkable[47] or high T_g polymers can be employed to improve the stability of the optical nonlinearity induced by AOP. However, according to our AOP relaxation results from the three different NLO polymeric systems as shown previously, $\chi^{(2)}$ dark relaxation is retarded upon prolonged AOP. It reveals that dipolar orientation relaxation is hindered. We would like to explore whether the dipolar rotational relaxation retardation exists only for odd order polar order parameters evolution which are reflected from $\chi^{(2)}$ relaxation or the rotational relaxation retardation exist generally upon prolonged successive photo-isomerization cycles? In the other words, would time evolution of even order polar parameter be retarded too upon prolonged successive photo-isomerization cycles? To understand the generality of dipolar rotational relaxation, photo-induced birefringence (BR) experiment was performed for studying time evolution of even order polar parameter ($\Delta n\,(t)$) upon different duration of photo-induced BR. Experimental setup and results will be shown in the following subsection.

2.3.7 Photo-induced birefringence (BR)

Birefringence (BR) refers to the variation of linear refractive index (n_i) of the material with reference to the laboratory coordinate axis: i = x, y, z. It exists naturally in intrinsic anisotropic materials. The linearly polarized EM field at 532 nm delivered by a Nd:YAG laser was employed to introduce anisotropy in the sample by angular hole burning (AHB) of azo-dyes (disperse red 1 DR1) in PMMA, PC and PSU through photo-isomerization. The photo-induced birefringence Δn was then monitored by a low-power Helium-Neon (He-Ne) laser at 633 nm. A schematic diagram of the photo-induced birefringence setup is shown in figure 2.11:

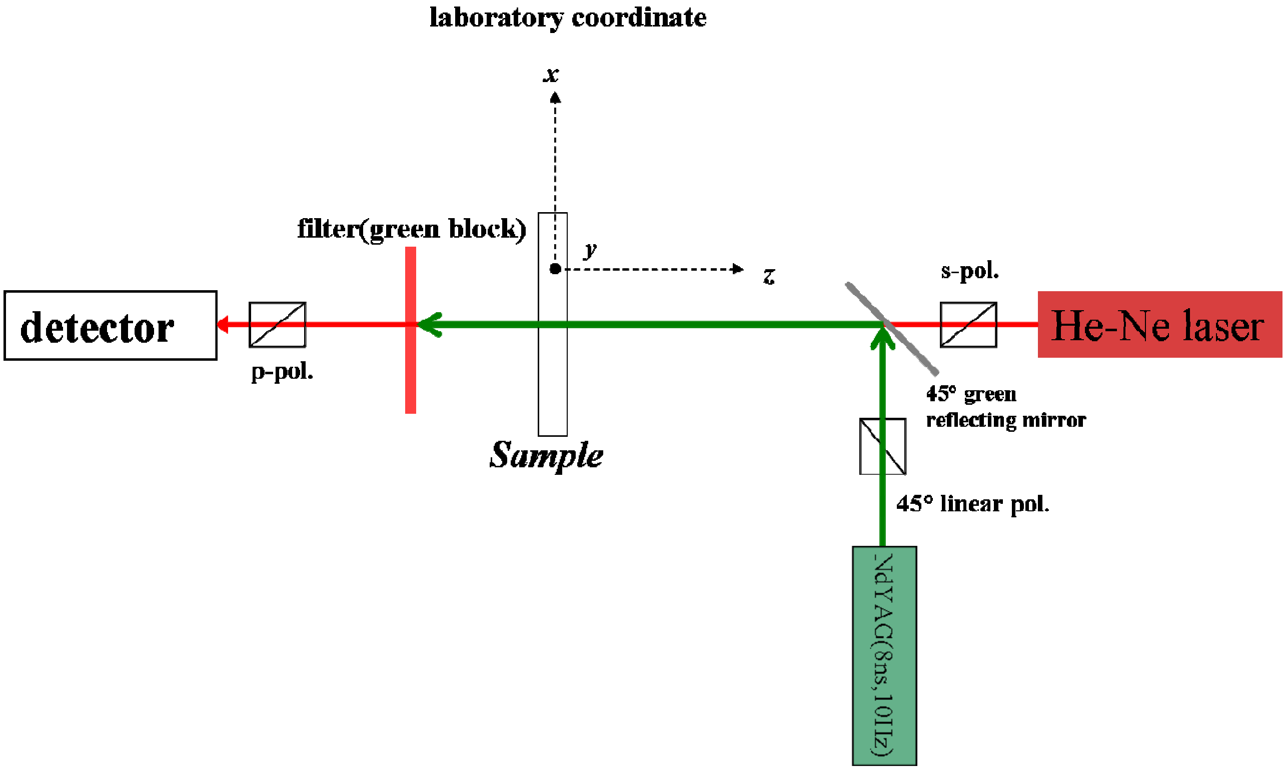

Figure 2.11 Schematic diagram of photo-induced birefringence (BR) experiment and Δn measurement

A 45° linearly polarized EM pulse at 532 nm (pulse energy ~ 0.5 mJ, illumination area ~ 20 mm^2) from the Nd:YAG laser is incident normally on the sample. It introduces the anisotropy to samples through successive angular selective azo-dye isomerization and reorientation. The low-power He-Ne laser (Spectra Physics SP155, power 1 mW) acts as the probe for photo-induced birefringence Δn in the plane perpendicular to the normal z-axis. A s-polarized red probe is sent onto the sample and the intensity of the p-polarized output is recorded by a Si-detector (HAMAMASTU S2281). The polarization state of the s-polarized input probe beam is modified due to the photo-induced BR.

2.3.8 Δn relaxation upon photo-induced birefringence (BR)

Birefringence was photo-induced in PMMA/DR-1, PS/DR-1 and PSU/DR-1 by a polarized green (532 nm) illumination for different time durations (t’). He-Ne laser was used for probing the birefringence $\Delta n(t)_{t'}$ growth and relaxation within around 1 hour after green illumination. These measurements were done isothermally at RT. The growth of $\Delta n(0)_{t'}$ and normalized dark relaxation $\Delta n(t)_{t'}$ are shown in figure 2.12a and figure 2.12b, respectively.

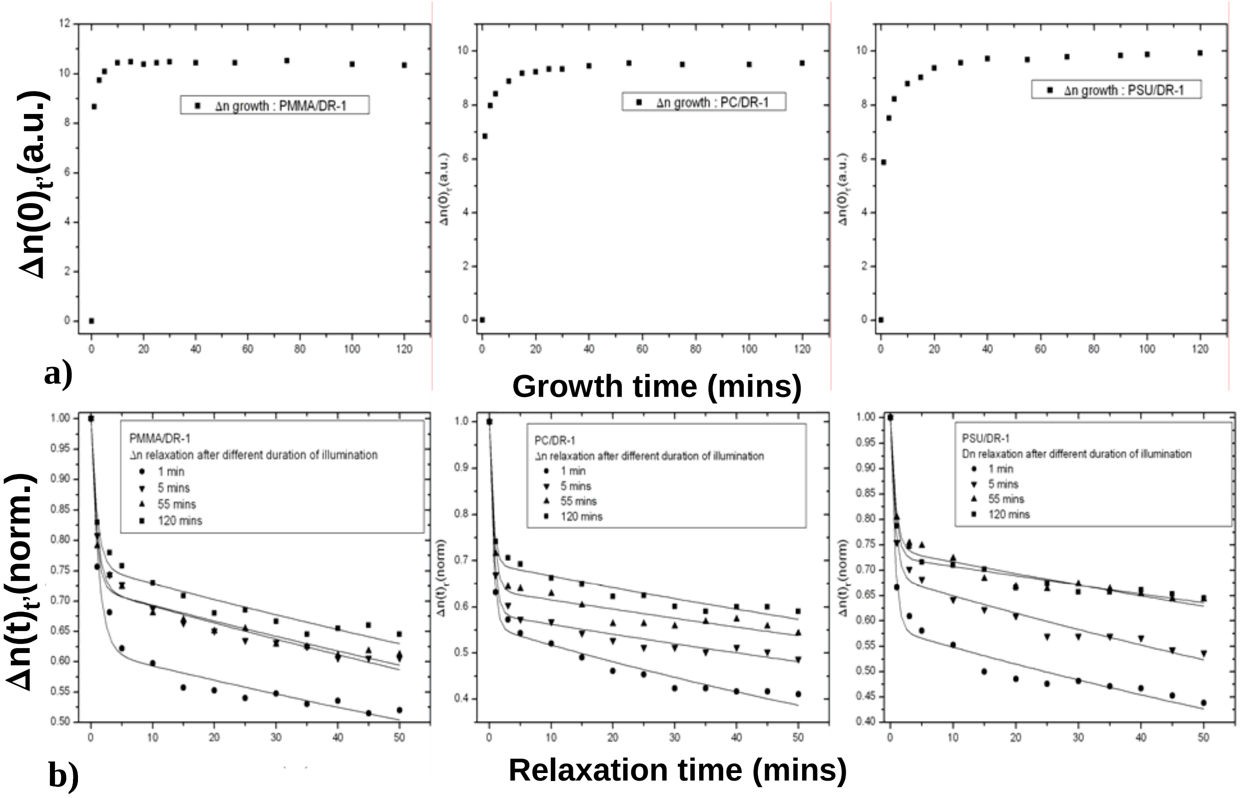

Figure 2.12 a) Growth of $\Delta n(0)_{t'}$ and b) normalized dark relaxation $\Delta n(t)_{t'}$ for different green illumination time duration (t’)

Solid lines are the biexponential decay fitting parameters of the growth and relaxation of photo-induced birefringence. The bi-exponential function employed is shown at right hand side of equation 2.13. Table 2.3 below shows $\Delta n(t)_{t'}$ relaxation biexponential fitting parameters.

t’	a	$\langle\tau\rangle_1$(min)	$\langle\tau\rangle_2$(min)	a	$\langle\tau\rangle_1$(min)	$\langle\tau\rangle_2$(min)	a	$\langle\tau\rangle_1$(min)	$\langle\tau\rangle_2$(min)
(min)	PMMA/DR-1			PC/DR-1			PSU/DR-1		
1	0.61	**245**	1.2	0.56	**137**	0.59	0.58	**159**	0.66
5	0.72	**243**	0.9	0.58	**258**	0.66	0.68	**184**	0.71
55	0.72	**259**	0.79	0.64	**296**	0.67	0.74	**307**	0.76
120	0.75	**272**	0.95	0.69	**264**	0.57	0.73	**377**	0.7

Table 2.3 Bi-exponential decay fitting parameters of $\Delta n(t)_{t'}$ relaxation
upon different duration of green illumination

We note that the slow decay constant $\langle\tau\rangle_1$ increases with increasing illumination time that the long-term relaxation of $\Delta n(t)_{t'}$ is retarded upon prolonged illumination. It is similar to the case of $\chi^{(2)}$ relaxation retardation though the magnitude of the decay fitting constants in BR and AOP relaxation cannot be compared quantitatively. This shows that generally speaking, guest polymer matrix is hardened upon prolonged photo-isomerization.

2.3.9 Discussion

For photo-induced BR, dye molecules which are more or less parallel to the EM field undergo repeated photo-isomerization cycles which cause free volume expansion to the surrounding polymer matrix. On the contrary, dye molecules which are more or less perpendicular to the EM field are not photo-excited and the volumetric expansion around the other dye molecules which are excited results in shrinkage of their surrounding polymer. Such polymeric expansion and shrinkage leads to the retardation of orientational thermal diffusion of dyes aligning perpendicular to the EM field. This explains how photo-induced BR (Δn) relaxation is retarded upon consecutive photo-induced isomerization cycles.

For AOP, the same competitive polymeric expansion and shrinkage processes as that for photo-induced BR takes place, but the excitation is polar and not axial. Under polar excitation due to the $\langle \mathbf{E}^3(r,t)\rangle_t$ interference of EM fields once dye molecules are aligned and oriented in the ‘photo-stable’ direction, the surrounding polymeric matrix shrinks, which hinders their thermal orientational diffusion. This explains how AOP-induced $<\chi^{(2)}(t)>_{t'}$ relaxation is retarded upon consecutive photo-induced isomerization cycles.

For dye-dispersed amorphous polymers, this is usually a distribution of thermal rotational diffusion time constants D according to the location of guest molecules at different polymeric environment. The distribution N(D) is broadened by inhomogeneity of the polymer matrix. So for corona poling (CP) or Thermally-assisted electric field poling (TAP), relaxation is usually described by a stretched exponential function[48] $e^{-\left(\frac{t}{\tau}\right)^{\beta}}$. However, for AOP-induced $\chi^{(2)}$ and photo-induced birefringence Δn relaxation, a biexponential function is often preferred to a stretched exponential function for data fitting. It shows that upon successive photo-isomerization cycles, there is a redistribution of thermal diffusion relaxation times τ of dye molecules on the contrary to a smooth continuous distribution of relaxation times for polymer matrix.

Decay of AOP-induced $\chi^{(2)}$ and photo-induced BR Δn upon different duration of photo-excitation at RT and elevated temperature was presented. Retardation of $\chi^{(2)}$ and Δn relaxation is observed upon prolonged photo-excitation in AOP and photo-induced BR. $\chi^{(2)}$ and Δn relaxation retardations upon prolonged photoexcitation reflect that molecule orientation relaxation retardation is a general characteristic of dye-doped polymer matrices. Retardation of $\chi^{(2)}$ relaxation in PMMA at 3 different temperatures below T_g suggests that the orientation relaxation retardation of the dye-molecules is not a temperature-localized effect and it takes place generally in the glassy state of the polymer matrix. Comparison of $\chi^{(2)}$ relaxation in polymer hosts with similar T_g (PMMA and PS) reveals that the polymer architecture (e.g. polarity) is a key factor determining the stability of the orientation relaxation upon photoexcitation. A phenomenological picture of the effect is given. It is attributed to the competing free volume expansion and shrinkage during a selective and polar/axial photo-isomeriaztion in AOP and photo-induced BR.

2.4 AOP and SHG diagnostics of a Layer-by-Layer deposited nonlinear polyelectrolyte

Since the first proposition of electrostatic macromolecular multi-layer self-assembly by Iler R. K. in 1966[49], it has been widely investigated due to its high potential applications. Electrostatic LBL self-assembly based on alternate adsorption of polyelectrolytes of opposite charges was further developed in early 90s by Decher *et al.*[50, 51] for the application in optical switching[52], opto-electronic device[53-55], biochemical sensor[56], and solar cell[57, 58]. Biological materials are employed recently for electrostatic LBL self-assembly which can be used for pharmaceutical industry[59-62].

Azo-dye functionalized polyelectrolyte (polyanion) is commonly employed for electrostatic LBL self-assembly with counter-ionic polyelectrolyte because of its high optical sensitivity, optical reversibility and optical durability (stability). Researchers studied dynamic of multilayer growth, film anisotropy and optical nonlinearity of azo-dye functionalized LBL films[63-68]. However, the understanding and the optimization of the film growth like the effect of salt, the effect of polyelectrolyte pH and polyelectrolytes' combination are still lacking. Atomic force microscopy (AFM), Quartz microbalance measurement (QCM) and Large-angle x-ray scattering are used for the characterization of the mechanical properties of LBL film while optical properties of LBL film are characterized very often by total internal reflection (TIR), dichroism, birefringence, second harmonic generation (SHG) and photo-fluorescence. One of the most important aspects for these film characterizations is to access the film stability with respect to time, temperature and different film environment.

In this section, electrostatic LBL self-assembly of an azo-dye functionalized polyelectrolyte and a counter-ionic polyelectrolyte is reported. Second order optical nonlinearity of their LBL films is studied by SHG. All-optical poling (AOP) is developed and demonstrated as an efficient diagnostic tool for accessing LBL film stability by monitoring orientational relaxation of chromophore in polymer matrix of LBL films.

2.4.1 Experiment

2.4.1.1 Materials

Azo-dye functionalized maleic anhydride copolymer (M-DR1) and polyethyleneimine (PEI) were employed as polyelectrolytes for LBL multilayer thin films preparation. PEI was purchased from Aldrich and used without further purification. M-DR1 was prepared and dissolved in dilute NaOH solution (~ 0.05M). The solution was maintained neutral as DR-1 moiety may be detached from the polymer chain if it is too acidic. Synthesis of M-DR1 is shown in figure 2.13. 18.2 MΩ Millipore water was used in all cleansing and dipping procedure.

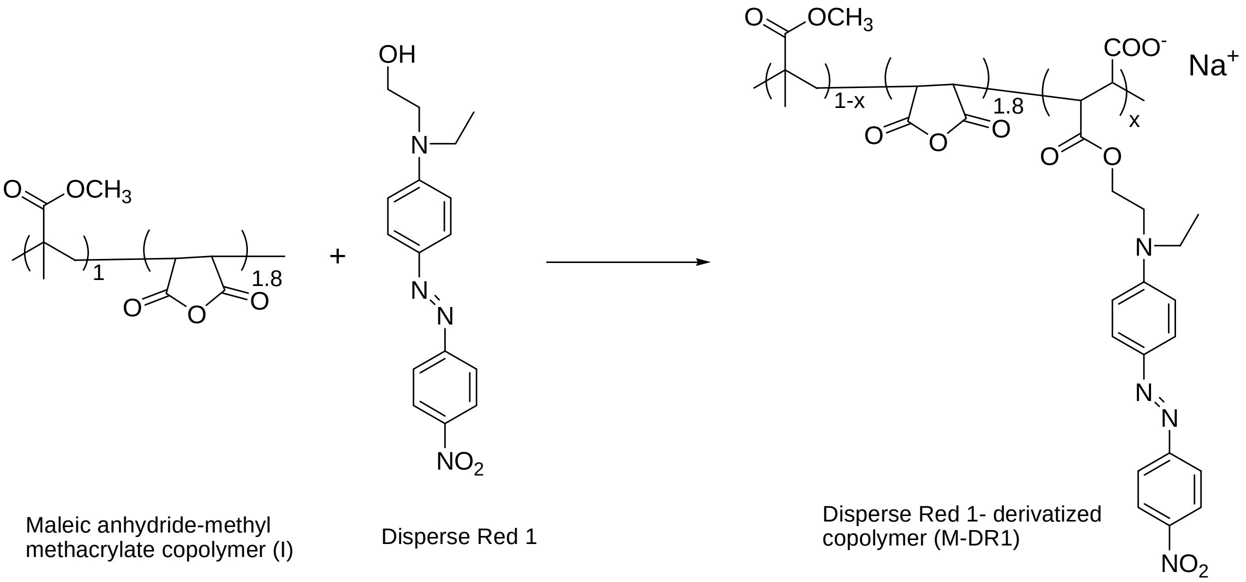

Figure 2.13 Reaction of poly(maleic anhydride-co-methyl methacrylate) (I) with Disperse Red 1 (DR1)

2.4.1.2 Layer-by-Layer self-assembly deposition

Glass substrates were cleaned by immersing in piranha solution (H_2O_2/concentrated H_2SO_4 3:7 v/v) for 2 hours and were washed with deionised water several times and dried in an oven at 120ºC. One side of glass substrates was covered with an adhesive tape. It was removed after finishing Layer-by-Layer (LBL) deposition so that one-side multilayer LBL film can be obtained. Substrates were immersed alternatively into polycation solution (PEI, 5 mg/ml and pH = 3.5 with the addition of H_2SO_4) and polyanion solution (hydrolyzed **M-DR1,** 1.2 mg/ml, pH = 7) as shown in figure 2.14 below.

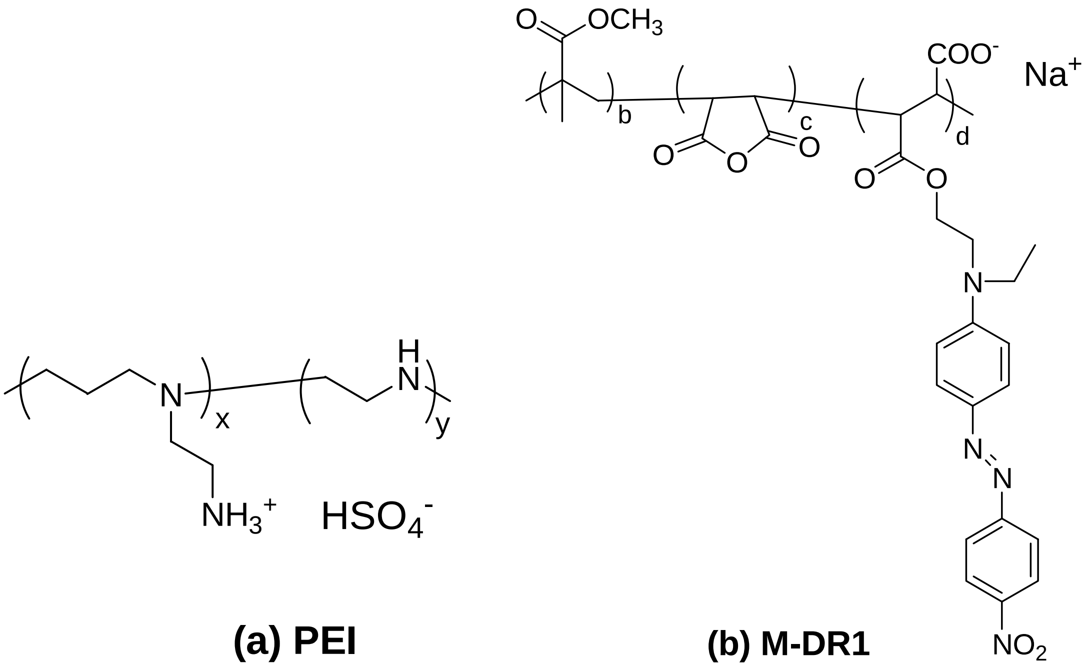

(a) PEI **(b) M-DR1**

Figure 2.14. Chemical structure of polyelectrolytes : a) Polycation (PEI)
b) Polyanion (M-DR1)

The dipping time in each polyelectrolyte solution was 10 minutes and substrates were rinsed with deionised water 2 times before they were immersed into another polyelectrolyte solution. For the studies of salt effect, sodium chloride (NaCl) was introduced into the polyelectrolyte solutions (0.05 M) for LBL self-assembly procedure. Films were dried in an oven at 90ºC for 5 hours once the desired number of bilayers (from 1 bilayer to 30 bilayers) was reached.

2.4.1.3 UV-Vis spectroscopy and film thickness measurement

UV-Vis absorption of LBL films with different number of bilayers was studied using Perkin Elmer Lambda 19 spectrometer. LBL films were placed at normal incidence with respect to the incoming beam and transmission at UV-Vis wavelength regime was measured. LBL film thickness was measured with mechanical method with a profilometer (Dektak 6M). All LBL films were measured after being dried in oven at 90°C for 5 hours.

2.4.1.4 Atomic Force Microscopy (AFM)

Surface morphology of LBL film is crucial in determining the quality and efficiency of Layer-by-Layer electrostatic self-assembly. Tapping mode atomic force microscopy (AFM) was employed for characterizing the superficial structure and the morphology of LBL films. Root mean square (RMS) roughness of LBL films was obtained from scan area of 3 μm x 3 μm.

2.4.1.5 Second Harmonic Generation (SHG)

An azo-dye containing polymer exhibits noncentro-symmetric structure if it is fabricated by LBL self-assembly. Chromophores are preferentially oriented along the surface normal asymmetrically during self-assembly process. LBL film of azo-dye containing polymer gives considerably large second-order optical nonlinearity $\chi^{(2)}$ as reported by different research groups[69-72]. Second Harmonic Generation (SHG) measurement was performed for the studies of second order optical linearity of freshly prepared M-DR1 LBL films. P-polarized fundamental pulses (1.064 μm , 8 ns, 10 Hz) from Nd:YAG laser (Quantel YG-580) were incident to LBL films at different incident angle θ_{in} with respect to film normal (z-axis). SHG signal (0.532 μm) of p-polarization was recorded with photomultiplier tube (PMT, Hamamatsu R1828-01) and further processed with oscilloscope. SHG signal level of the LBL films was compared quantitatively with a referencing nonlinear optical (NLO) Zinc Oxide single crystal (MTI, thickness = 500 μm). Schematic diagram of the SHG measurement is shown in figure 4.5.

2.4.1.6 All-Optical Poling (AOP)

Stability of the intrinsic noncentro-symmetric azo-dye orientation in the LBL self-assembly was probed by All-Optical Poling[73] (AOP). Quasi-permanent second-order optical nonlinearity $\chi^{(2)}_{AOP}$ grating was inscribed in the samples during AOP. Coherent fundamental (1.064 μm) and Second Harmonic SH (0.532 μm) pulses from Nd:YAG laser were incident onto PEI:M-DR1 or PEI:M-DR1(NaCl) LBL films coherently for $\chi^{(2)}_{AOP}$ grating inscription. Relative pulse energies of fundamental and SH were adjusted for optimizing AOP efficiency. Orientation stability of azo chromophores of LBL films upon AOP was investigated by monitoring decay of inscribed $\chi^{(2)}_{AOP}$ grating ($\sim I_{SHG}^{0.5}$) as soon as the termination of AOP. In addition, centro-symmetric M-DR1 film with thickness 0.5 μm, prepared by spin-coating, was also oriented by AOP in order to compare the influence of M-DR1 film preparations (Remarks : LBL self-assembly gives non-centrosymmetric film while spin-coating gives amorphous film) to polymer rigidity and reversibility. Detail of experimental setup is shown in figure 2.7.

2.4.2 SHG and AOP results

2.4.2.1 LBL film characterization

One of the most convenient methods to monitor the growth of LBL multilayer is by absorption spectroscopy. UV-Vis absorption characteristic of LBL films were measured after the desired number of bilayer were attained. According to figure 2.15a, from 2 to 30 bilayers, UV-Vis absorption profile of PEI:M-DR1 LBL films corresponds satisfactorily and linearly to the number of bilayers without any observable transition band shift or emergence of any other special transition feature. It proves that for the LBL self-assembly of PEI:M-DR1, there is no ‘saturation’ (termination of polyionic attachment) in LBL self-assembly within 30 cycles of dipping. Linear dependence of film thickness on the number of bilayer of PEI:M-DR1 (insert of figure 2.15a) support further that the self-assembly process was achieved successfully. For PEI:M-DR1(NaCl), UV-Vis absorption profile and film thickness correspond to the number of bilayer as those of PEI:M-DR1. With the addition of NaCl in polyelectrolytes for LBL self-assembly, film thickness and absorbance were different from that without addition of NaCl. Absorbance of PEI:M-DR1(NaCl) was approximately 3 times higher than that of PEI:M-DR1 with the same number of bilayer and its film thickness increased proportionally. Some researchers[74, 75] reported previously that the introduction of salt to polyelectrolytes would increase bilayer thickness which in turn, increases film absorbance as a result of the increment of dye content in the film. UV-Vis spectrum of 20 bilayers of PEI:M-DR1 and PEI:M-DR1(NaCl) is shown is figure 2.15b. An interesting red shift of absorption peak from PEI:M-DR1 (λ_{max} = 468 nm) to PEI:M-DR1(NaCl) (λ_{max} = 473.5 nm) was observed and this feature exists regardless of the number of bilayer of LBL film being prepared. Further investigation of the effect of ions (Na^+ and Cl^-) to special transition band feature of dye in LBL structure is needed for the understanding of the red-shift phenomenon.

One of the advantages of LBL self-assembly method is that it can yield multilayer thin film with relatively smooth surface compared to thin film prepared by spin-coating or vacuum deposition. Surface roughness is a crucial factor which affects the performance of organo-electronic device. The surface morphologies of the PEI:M-DR1 thin films were studied by AFM. AFM photos of samples of different number of LBL are shown in figure 2.16a and figure 2.16b. The RMS roughness increased from 10 nm (10 bilayers) to 20 nm (30 bilayers) in salt-free system (PEI:M-DR1) and 11 nm (10 bilayers) to 26 nm (30 bilayers) in ‘salted’ system (PEI:M-DR1(NaCl).

There were observable differences in the surface morphologies between the 2 systems. Pronounce polymer aggregations were observed in the system with NaCl. This maybe due to the charge shielding by additional salt (NaCl) which allowed the polymer to coil up and to aggregate during self-assembly process.

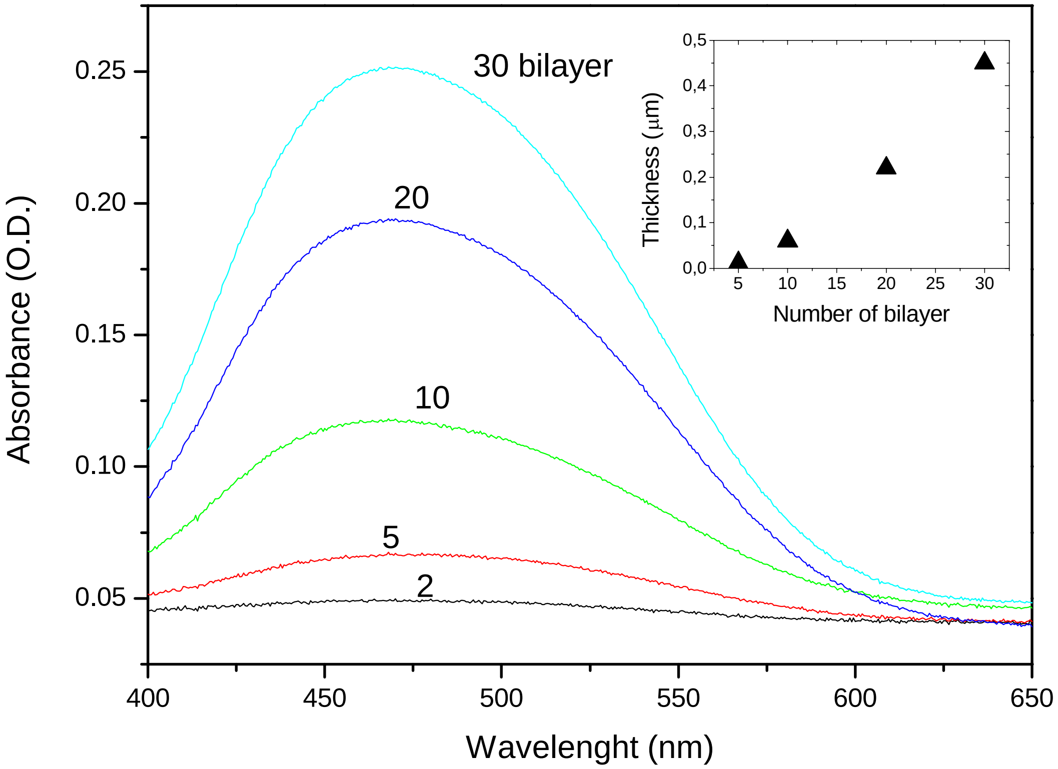

Figure 2.15a. UV-Vis absorption spectrum and thickness of PEI:M-DR1
for different number of bilayer

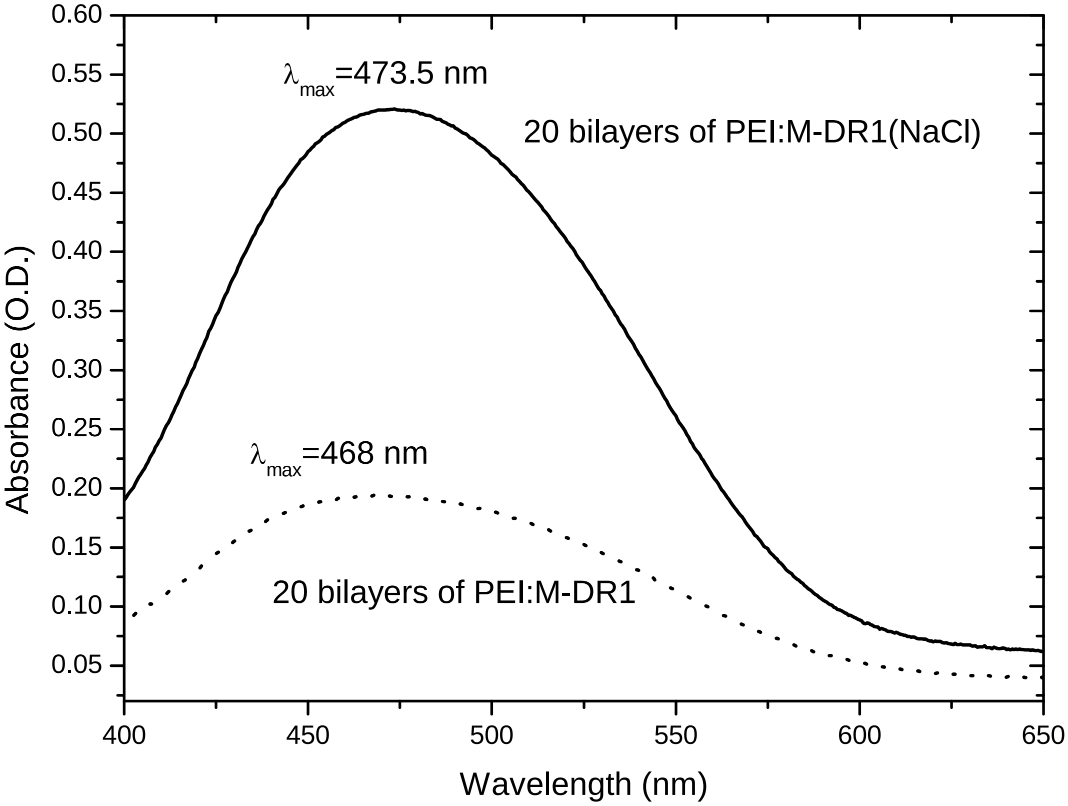

Figure 2.15b. Comparison of UV-Vis absorption of PEI:M-DR1 and PEI:M-DR1(NaCl) of 20 bilayers

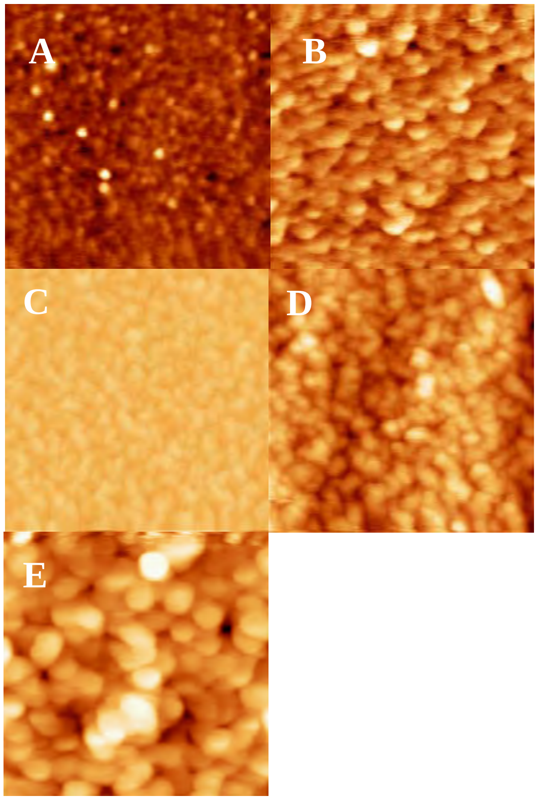

Figure 2.16a. AFM images (3x3 μm^2) of PEI:M-DR1 of A)1, B)5, C)10, D)30 and E)40 bilayers

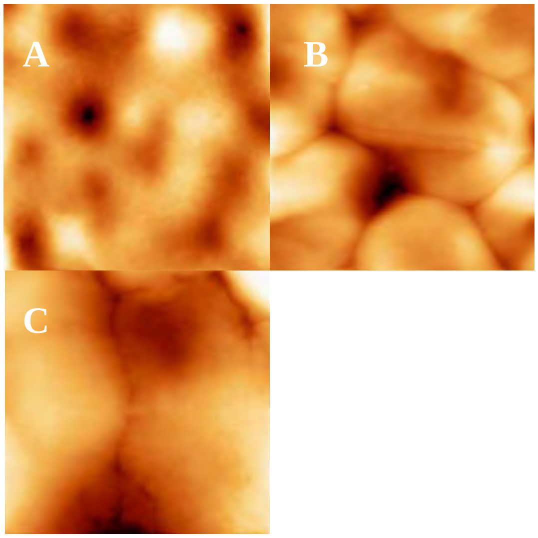

Figure 2.16b. AFM images (3x3 μm^2) of PEI:M-DR1(NaCl) of A)10, B)20 and C)30 bilayers

2.4.2.2 Second order optical nonlinearity $\chi^{(2)}$ of M-DR1 LBL

Second order optical nonlinearity $\chi^{(2)}$, which relates to noncentro-symmetric alignment of chromophore (DR1) of M-DR1 LBL film, was studied by Second Harmonic Generation (SHG). The SH signal power from LBL films can be expressed as :

$$P_{2\omega} = \frac{32\pi^3}{cA}\frac{[t_{af}^{\omega}]^4[t_{fs}^{2\omega}]^2[t_{sa}^{2\omega}]^2}{n_{2\omega}{}^2 c_{2\omega}{}^2} P_{\omega}^2 (\frac{2\pi l}{\lambda})^2 e^{-2\delta_{2\omega}} \frac{\sin^2\Psi + \sinh^2\delta_{2\omega}}{\Psi^2 + \delta_{2\omega}{}^2}\left(\chi_{eff}^{(2)}\right)^2 \qquad (2.18)$$

where : $[\mathbf{t}^{i}{}_{jk}]$ are the Fresnel transmission coefficients of fundamental (ω) and SH (2ω) beams at different interfaces; A is the area of the laser beam spot; $\delta_{2\omega}$ is the absorption coefficient of LBL films at 532 nm; $\Psi=(2\pi l/\lambda)(n_{\omega}\cos\theta_{\omega}-n_{2\omega}\cos\theta_{2\omega})$ is the phase mismatch parameter; P_{ω} and $P_{2\omega}$ are the powers of incident fundamental beam and SH output beams; $\chi^{(2)}{}_{eff}$ is the effective second-order nonlinear optical (NLO) coefficient. Under LBL self-assembly, films would possess 6mm point group symmetry and $\chi^{(2)}{}_{eff}$ could be expressed as :

$$\chi^{(2)}{}_{eff} = \chi_{zxx}^{(2)}\left(\sin\theta_{2\omega}\cos^2\theta_{\omega} + \cos\theta_{2\omega}\sin 2\theta_{\omega}\right) + \chi_{zzz}^{(2)}\sin\theta_{2\omega}\sin^2\theta_{\omega} \qquad (2.19)$$

providing that p-polarized fundamental pulses are incident onto the samples and p-polarized SHG signal pulses are recorded (p-p configuration). Results of SHG measurement in p-p configuration of PEI:M-DR1 and PEI:M-DR1(NaCl) ranging from 1 bilayer to 30 bilyers are shown in figure 2.17. Best data fitting according to equation 2.18 and equation 2.19 of SHG is presented as well. Fitting values of non-vanishing second order NLO coefficients $\chi^{(2)}{}_{zxx}$(pm/V) and $\chi^{(2)}{}_{zzz}$(pm/V) are summarized in table 2.4. In addition, for clearer understanding of average chromophore orientation in LBL films, second order NLO coefficients are expressed as an unit per bilayer per unit density ($\chi^{(2)}{}_{zxx}$(u.), $\chi^{(2)}{}_{zzz}$(u.)) of chromophore for direct comparison of degree of chromophore alignment in PEI:M-DR1 and PEI:M-DR1(NaCl) LBL films respectively.

No. of Bilayer	**PEI :M-DR1** **I(SHG)$_{p-p}$(a.u.)**	**PEI :M-DR1(NaCl)** **I(SHG)$_{p-p}$(a.u.)**
1	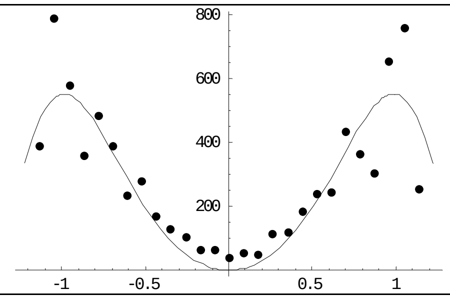	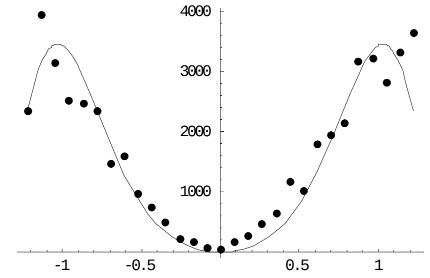
2	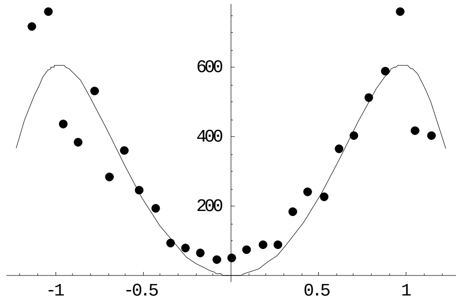	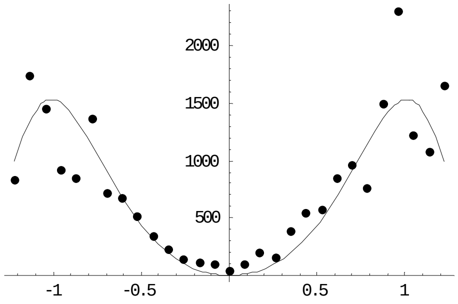
5	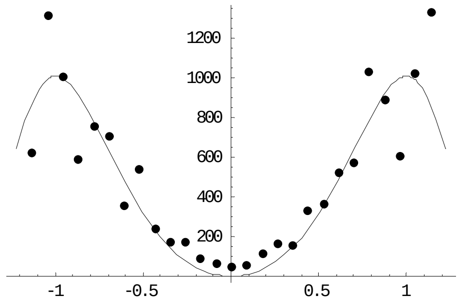	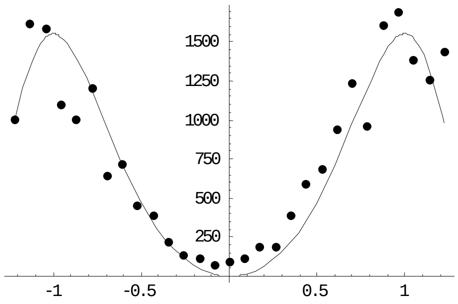
10	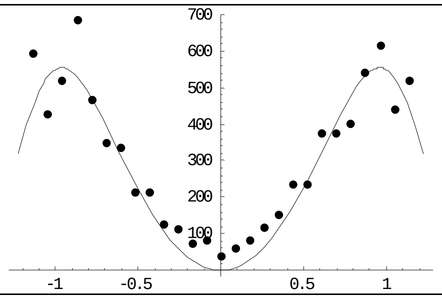	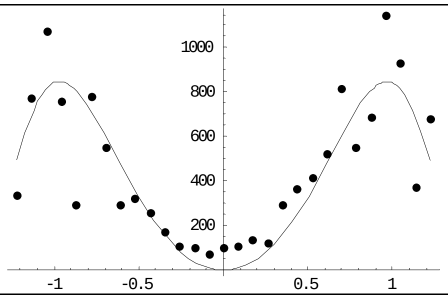
20	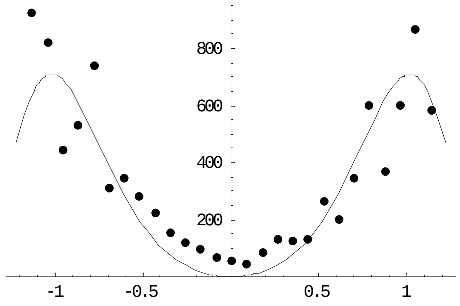	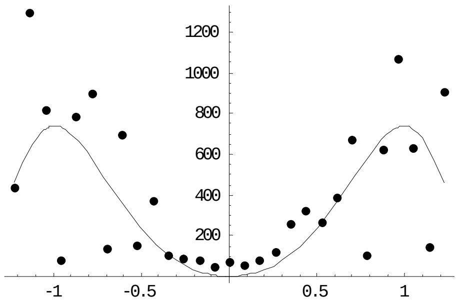

30	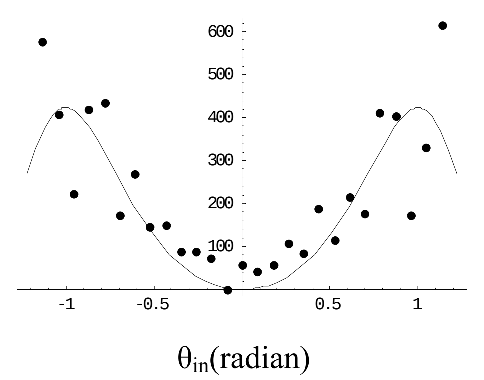	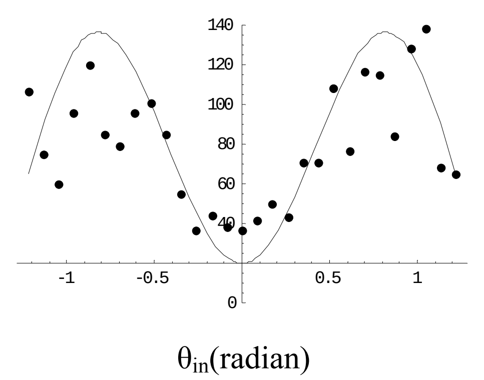

Figure 2.17 SHG measurement of PEI:M-DR1 and PEI:M-DR1(NaCl) of different number of bilayer and their data fitting according to equation 2.18 and equation 2.19. The measurement are in p-in/p-out configuration

Number of bilayer	$\chi^{(2)}_{zxx}$ (pm/V)	$\chi^{(2)}_{zzz}$ (pm/V)	$\chi^{(2)}_{zxx}$(u.) (per bilayer, DR-1 density)	$\chi^{(2)}_{zzz}$(u.) (per bilayer, DR-1 density)
PEI :M-DR1				
1	1.36	6.94	1.36	6.94
2	1.4	3.52	0.7	1.76
5	0.14	2.18	0.028	0.436
10	0.16	0.64	0.016	0.064
20	0.06	0.6	0.003	0.03
30	0.04	0.3	0.0013	0.01
PEI :M-DR1(NaCl)				
1	2.54	25.56	1.016	10.224
2	1.02	5.7	0.204	1.14
5	0.46	3.1	0.0368	0.248
10	0.22	1.02	0.0088	0.0408
20	0.1	0.7	0.002	0.014
30	0.06	0.4	0.0008	0.0053

Table 2.4. Fitting value of 2nd order NLO coefficients of PEI:M-DR1 and PEI:M-DR1(NaCl) of different number of bilayer from SHG measurement

Referring to table 2.4, when number of bilayer increases from 1 to 30, second order NLO coefficients decrease monotonically. In addition, for all number of bilayer being tested, $\chi^{(2)}_{zxx}$(u.) and $\chi^{(2)}_{zzz}$(u.) of PEI:M-DR1 are around 2 times higher (except for 1 bilayer) than that of PEI:M-DR1(NaCl) which infers that noncentro-symmetric alignment of chromophore is more efficient in PEI:M-DR1 LBL polymeric structure than that in PEI:M-DR1(NaCl) under the identical film preparation procedure. Screening effect due to counter ions (Na^+ and Cl^-) which diffused at the surrounding of chromophores would weaken the E-field gradient across the film during the self-assembly process and as the result, the degree of chromophore alignment with respect to the surface normal would eventually be diminished. Previous SHG studies of PAH:M-DR1 by our group[76] suggested that second-order optical nonlinearity increases up to 5 bilayers which is different from that of PEI:M-DR1 or PEI:M-DR1(NaCl) discussed above. This reveals that the choice of polycation is crucial in determining LBL film nonlinearity.

2.4.2.3 Access of optical nonlinearity stability of LBL film by AOP

All-optical poling (AOP) is regarded as a convenient and efficient method for centro-symmetry breaking of azo-NLO polymeric system. Under photo-excitation of coherent electromagnetic fields (ω and 2ω), azo-chromophores in NLO system are orientated successively in trans-cis-trans isomerization process to attain a new energetic stable orientation configuration. Macroscopic second order nonlinear optical grating $\chi^{(2)}{}_{AOP}$ is inscribed in LBL films upon AOP : $\chi^{(2)}{}_{AOP} \sim \langle\{E_{\omega}(t)+E_{2\omega}(t)\}^{3}\rangle_{t}$. During $\chi^{(2)}{}_{AOP}$ inscription, intrinsic chromophore orientation of LBL films is perturbed and chromophores are reorientated under influence of EM fields. As soon as AOP stops, reorientated chromophores relax thermo-dynamically. For intrinsically centro-symmetric spin-coated NLO polymer, orientational relaxation of chromophore can be approximated as :

$$\frac{dN(\Omega)}{dt} = D\nabla^{2}N(\Omega) \tag{2.20}$$

where N(Ω) is the number of chromophore at solid angle Ω, D is homogeneous thermal rotational diffusion constant of polymer matrix. However, for LBL films like PEI :M-DR1 and PEI :M-DR1(NaCl) that we study, equation 2.20 would no longer be valid for describing rotational relaxation of chromophores due to 'inhomogeneity' of chromophore environment brought by LBL polyelectrolytes adsorption process. In another word, thermal rotational diffusion of chromophore is inhomogeneous and it depends largely on intrinsic LBL film structure. In this section, we develop AOP as a diagnostic tool for the access of optical nonlinearity stability of LBL film.

Thermal rotational diffusion of chromophore in LBL self-assembly film upon AOP can be expressed as :

$$\frac{dN(\Omega)}{dt} = D\nabla^{2}N(\Omega) + \mu E \sin^{2}\theta N(\Omega) \tag{2.21}$$

where the second term is 'restoring torque' modification due to intrinsic ordering in LBL self-assembly sample.

Upon LBL self-assembly, chromophores (polyelectrolytes as well) are arranged noncentro-symmetrically due to net electrostatic attraction $\left(\vec{E}\right)$ of polyions. The capability of chromophoric noncentro-symmetric alignment in LBL film is reflected from SHG measurement as discussed in section 2.2. The bigger the second order optical nonlinearities ($\chi^{(2)}{}_{zxx}$(u.) and $\chi^{(2)}{}_{zzz}$(u.)), the stronger the intrinsic constraint implied by electrostatic attraction. Therefore, it is similar to the electric poling of NLO polymer[77] : $\chi^{(2)}$ ~ Electric field strength (E). In addition to homogeneous thermal rotational relaxation, chromophores experience an inhomogeneous restoring torque $\mu E \sin^2\theta$ simultaneously. Intrinsic electrostatic attraction $\left(\vec{E}\right)$ in LBL film is proportional to $\chi^{(2)}{}_{zzz}$(u.) obtained from SHG measurement : $\overline{E} \sim \chi^{(2)}{}_{zzz}(\text{a.u.}) = k\chi^{(2)}{}_{zzz}(\text{a.u.})$. Thermal rotational relaxation of chromophores in LBL film upon AOP is further elaborated according to equation 2.21 as:

$$\frac{dN(\Omega)}{dt} = D\nabla^2 N(\Omega) + k\mu\chi^{(2)}_{zzz}(\text{a.u.})\sin^2\theta N(\Omega) \qquad (2.22)$$

and the dynamic of thermal relaxation of chromophores can be inferred as the decay of inscribed $\chi^{(2)}{}_{AOP}$ ($SHG^{0.5}$) as :

$$\chi^{(2)}{}_{AOP}(t) = \chi^{(2)}{}_{AOP}(0)e^{-(D+\alpha\chi^{(2)}_{zzz})t} \qquad (2.23)$$

where α is a coupling constant of the restoring torque (where $\alpha = 2k\mu$). It measures the stability of intrinsic chromophores alignment in LBL film. The higher the value of the coupling constant, the higher the orientation stability of chromophore in LBL film. It means that chromophores, which have been orientated during AOP, have a bigger tendency to re-orientate back to the original configuration imposed by the LBL self-assembly process.

Figure 2.18 and figure 2.19 show normalized $\chi^{(2)}{}_{AOP}$ decay of PEI :M-DR1 and PEI :M-DR1(NaCl) film upon 30 minutes of AOP for different number of bilayer from 5 to 30.

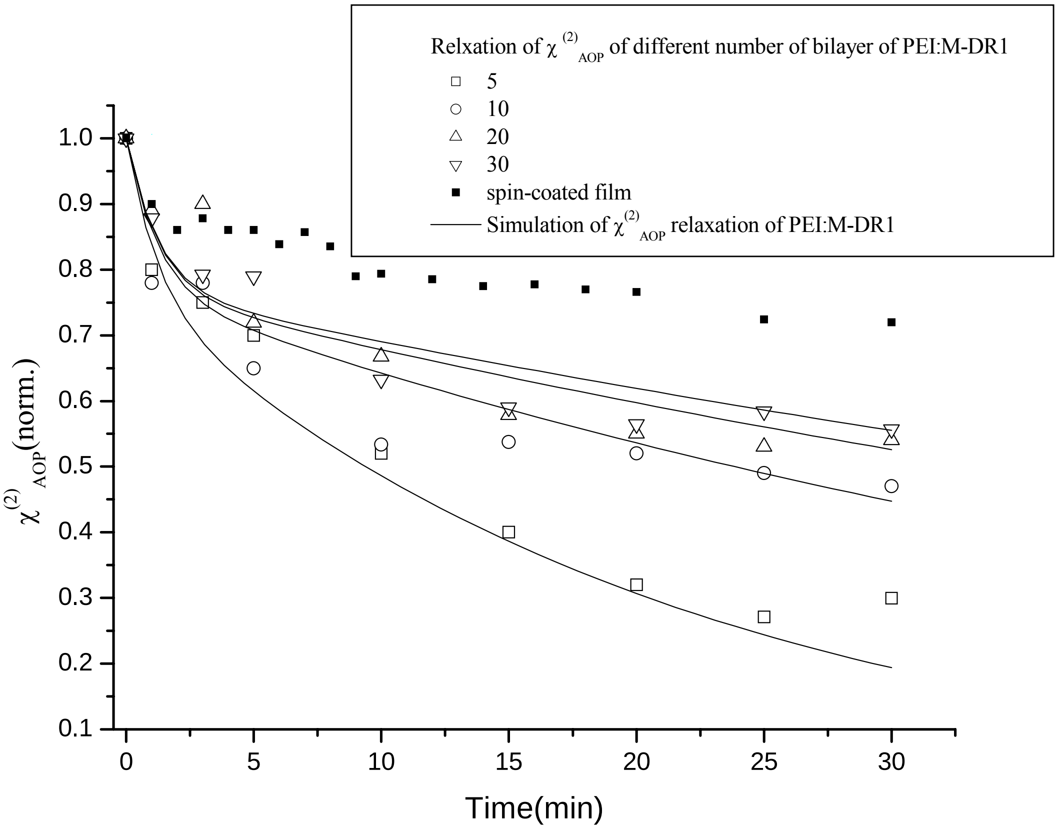

Figure 2.18. Relaxation of $\chi^{(2)}_{AOP}$ of different number of bilayer of PEI:M-DR1 and their relaxation simulation according to restoring torque model of equation 2.23

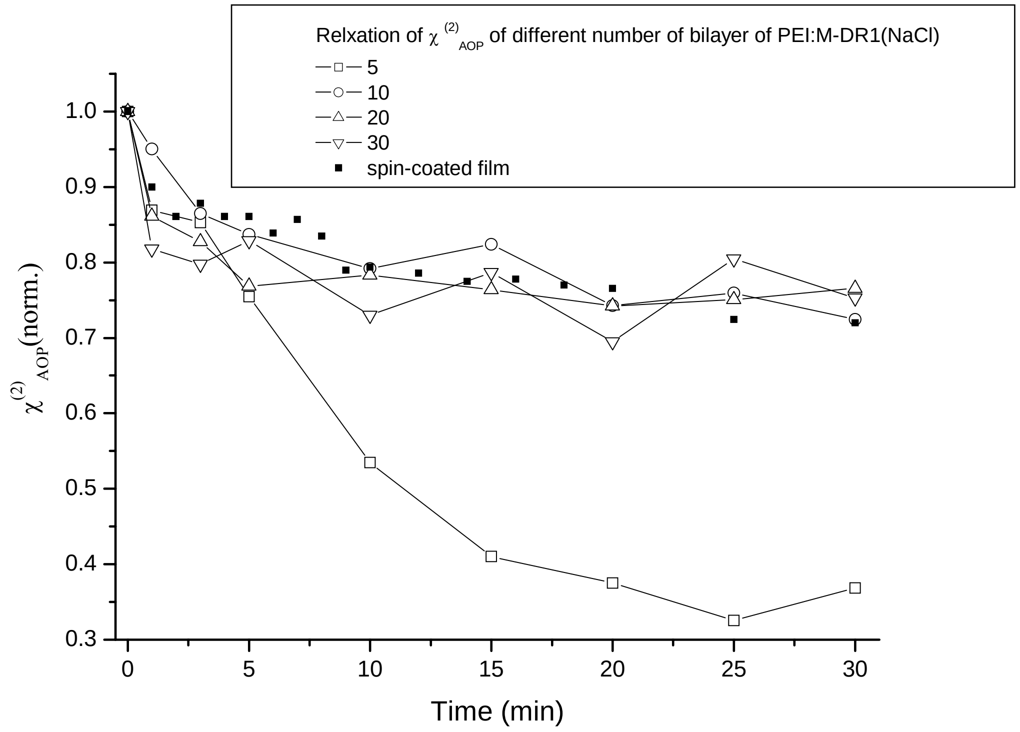

Figure 2.19. Relaxation of $\chi^{(2)}_{AOP}$ of different number of bilayer of PEI:M-DR1(NaCl) and their relaxation simulation according to restoring torque model of equation 2.23

For both kinds of LBL films, the more the number of bilayer, the slower the $\chi^{(2)}_{AOP}$ decay. The effect of restoring torque imposed on chromophores diminishes when increasing number of bilayers (as $\chi^{(2)}_{zzz}$(u.) diminishes). It reflects that chromophores are aligned in more stable configuration at the first few layers of LBL self-assembly. $\chi^{(2)}_{AOP}$ decay of spin-coated M-DR1 film (0.5 μm) is inserted in both figures for the decay comparison. For PEI:M-DR1(NaCl), $\chi^{(2)}_{AOP}$ decay is slower than that of PEI:M-DR1. We attribute it to weak intrinsic chromophore alignment and rearrangement of ions when compared to more rigid polymer matrix in all optical poling process.

We simulated $\chi^{(2)}_{AOP}$ decay of PEI:M-DR1 based on our proposed 'restoring torque' modified thermal rotational diffusion model (equation 2.23). Bi-exponential decay function and $\chi^{(2)}_{zzz}$(u.) of PEI:M-DR1 (from table 2.4) are employed for $\chi^{(2)}_{AOP}$ simulation :

$$\chi^{(2)}{}_{AOP}(\text{norm.}) = ae^{-(D_1+\alpha\chi^{(2)}_{zzz})t} + (1-a)e^{-(D_2+\alpha\chi^{(2)}_{zzz})t} \tag{2.24}$$

Best $\chi^{(2)}{}_{AOP}$ decay simulation of different number of bilayer of PEI:M-DR1 ($a = 0.77$, $D_1 = 0.01$, $D_2 = 0.8$, $\alpha = 0.09$) is shown in figure 2.18 which corresponds satisfactorily to the experimental results. It illustrates that the 'restoring torque' model explains well the rotational relaxation mechanism of chromophore in inhomogeneous LBL film and it illustrates that All-Optical Poling AOP could be employed as a diagnostic tool for accessing the stability of nonlinear LBL self-assembly multilayer film.

2.4.3 Discussion

Home-made Disperse Red 1 functionalized maleic anhydride copolymer (M-DR1) and polyethyleneimine (PEI) are employed as polyelectrolytes in LBL self-assembly. PEI :M-DR1 and PEI :M-DR1(NaCl) LBL films were fabricated successfully using the layer-by-layer electrostatic self-assembly deposition method. Films were characterized with UV-Vis absorption spectroscopy, thickness profilometer, Atomic force microscopy (AFM), Second harmonic generation (SHG) and All-optical poling (AOP). Results show that PEI:M-DR1 and PEI :M-DR1(NaCl) can be assembled satisfactorily up to at least 30 bilayers without any disruption of the film thickness and the absorbance. AFM film studies showed that surface Rough Mean Square (RMS) roughness increases with increasing number of bilayer. SHG measurement confirmed that for PEI :M-DR1 and PEI :M-DR1(NaCl), average noncentro-symmetric chromophore alignment in the LBL films decrease monotonically with increasing number of bilayer. $\chi^{(2)}{}_{zxx}$(u.) and $\chi^{(2)}{}_{zzz}$(u.) of PEI:M-DR1 are around 2 times larger than that of PEI:M-DR1(NaCl). It infers that noncentro-symmetric alignment of chromophore is more efficient in PEI:M-DR1 LBL film than that in PEI:M-DR1(NaCl) film under the identical film preparation procedure. At last, AOP is illustrated as a diagnostic tool to study the stability of the intrinsic chromophore alignment in LBL films. Thermal rotational relaxation of chromophore in PEI :M-DR1 film of different number of bilayer oriented by AOP is simulated with the addition of a 'restoring torque' model correction.

With the addition of salt (NaCl) during LBL assembly of the NLO azo-polymer, NLO stability is generally enhanced in the sense of the stability of noncentro-symmetric azo-dye orientation in polymer matrix. However, more studies have to be done for clarifying the stabilizing effect of salt to NLO azo-LBL polymer.

2.5 Chapter summary

In summary, we demonstrated the feasibility of Second Harmonic Generation (SHG) and All-Optical Poling (AOP) as non-invasive sensitive diagnostic tools to study stability and second order nonlinearity of 2 different types of NLO azo-polymer system : Guest-Host polymer system and LBL self-assembly system. Generally speaking, SHG monitors the first order NLO effect and so, SHG sensitivity to dye motion of NLO system would be in much higher comparing to other techniques like Birefrigence (BR) or Electric Field Induced Second Harmonic Generation (EFISHG). With the aid of AOP, non-perturbated (dark) dipole motion (relaxation) in polymer matrices can be studied conveniently.

From $\chi^{(2)}$ relaxation studies of polymer with different rigidity upon different duration of all-optical poling and photo-induced birefrigence, we verify that polymer viscosity surrounding azo-dye is strengthened on average. It is contrary to the commonly accepted argument that photo-isomerization during photo-excitation would most likely loosen NLO azo-polymer viscosity and the stability of NLO azo-polymer is lower if poling involves photo-isomerization (like PAP and AOP) instead of pure electric means (like CP and TAP). An explanation of polymer hardening upon photo-isomerization was given. Moreover, we found out that dipolar orientation stability of azo-dye in polymer is no longer governed only by the glass transition temperature of polymer host which has been already reported previously[78, 79]. Higher order polymer local relaxation (like beta relaxation) would affect the rotational stability of the azo-dye in polymer as well.

In addition, we studied azo-dye-grafted NLO polymer, which was assembled by Layer-By-Layer (LBL) technique. By employing Second Harmonic Generation measurement technique, we found that increasing number of self-assembly layer would decrease the alignment capability of grafted azo-dye molecules and we showed that too the incorporation of salt in polyelectrolytes during LBL process can enhance the azo-dye alignment tendency. In addition, we developed a method (SECONDARY POLING by AOP) of accessing the stability of intrinsic azo-dye alignment in LBL film. With a ‘restoring torque’ model, we could compare and access stability of azo-dye alignment in LBL films which is potentially useful in the future as a diagnostic tool for studying LBL film stability and forming mechanism.

As investigated by Ortyl E. *et al.*[80] on $\chi^{(2)}$ relaxation of polyurethanes grafted with two different kind of azo-dye (end with a. sulfonamide group or b. nitro group) upon saturation AOP, results show that $\chi^{(2)}$ relaxation depends significantly on the ending group of azo-dye and polymer architecture of polyurethanes. It illustrate AOP can be acted as an useful tool to monitor the stability and capability of different new NLO polymer for tailor-making and designing better azo-dye NLO polymer for application.

In order to further understand the effect of AOP (photo-induced isomerization) to polymer hardening, we are carrying on with Positron Annihilation Spectroscopy[81] (PAS) to study the free volume distribution in polymer upon different duration of AOP (photo-induced isomerization). Tracking the temporal change of polymer free volume upon AOP would indeed give deep insight of the polymer hardening feature by consecutive dipolar rotation and volumetric expansion (contraction).

Chapter references

1. K. D. Singer, J. E. Sohn, and S. J. Lalama, "2nd Harmonic-Generation In Poled Polymer-Films," Applied Physics Letters **49**(5), 248-250 (1986).
2. H. L. Hampsch, J. Yang, G. K. Wong, and J. M. Torkelson, "Dopant orientation dynamics in doped second-order nonlinear optical amorphous polymers. 1. Effects of temperature above and below Tg in corona-poled films," Macromolecules **23**(15), 3640-3647 (1990).
3. G. A. Lindsay, R. A. Henry, J. M. Hoover, A. Knoesen, and M. A. Mortazavi, "Sub-T(G) Relaxation Behavior Of Corona-Poled Nonlinear Optical Polymer-Films And Views On Physical Aging," Macromolecules **25**(19), 4888-4894 (1992).
4. K. D. Singer, M. G. Kuzyk, W. R. Holland, J. E. Sohn, S. J. Lalama, R. B. Comizzoli, H. E. Katz, and M. L. Schilling, "Electro-Optic Phase Modulation And Optical 2nd-Harmonic Generation In Corona-Poled Polymer-Films," Applied Physics Letters **53**(19), 1800-1802 (1988).
5. M. Dumont and A. El Osman, "On spontaneous and photoinduced orientational mobility of dye molecules in polymers," Chemical Physics **245**(1-3), 437-462 (1999).
6. Z. Sekkat and M. Dumont, "Photoinduced Orientation Of Azo Dyes In Polymeric Films - Characterization Of Molecular Angular Mobility," Synthetic Metals **54**(1-3), 373-381 (1993).
7. M. Dumont and Z. Sekkat, "Dynamical study of photoinduced anisotropy and orientational relaxation of azo dyes in polymeric films. poling at room temperature," SPIE **1774**, 188-199 (1992).
8. J. M. Nunzi, C. Fiorini, A. C. Etile, and F. Kajzar, "All-optical poling in polymers: dynamical aspects and perspectives," Pure And Applied Optics **7**(2), 141-150 (1998).
9. C. Fiorini, F. Charra, J. M. Nunzi, and P. Raimond, "Quasi-permanent all-optical encoding of noncentrosymmetry in azo-dye polymers," Journal Of The Optical Society Of America B-Optical Physics **14**(8), 1984-2003 (1997).
10. X. Liu, G. Xu, J. Si, P. Ye, Z. Li, and Y. Shen, "Erasure effect of the reading beam on the decay process of chi((2)) in all-optical poling," Applied Physics B-Lasers And Optics **71**(4), 539-543 (2000).
11. J. H. Si, J. R. Qiu, and K. Hirao, "Control of the noncentrosymmetry of thick

polymer films by nonresonant all-optical poling," journal of applied physics **90**(10), 4895-4899 (2001).

12. Y. Sui, X. Q. Yu, J. Yin, X. X. Zhong, Q. Li, Y. L. Chen, Z. K. Zhu, and Z. G. Wang, "All-optical poling of a side-chain poly(urethane-imide) film and surface morphology studies," Optics Communications **191**(3-6), 439-444 (2001).
13. X. X. Zhong, X. Q. Yu, Q. Li, S. Y. Luo, Y. L. Chen, Y. Sui, and J. Yin, "Identification of the alignment of azobenzene molecules induced by all-optical poling in polymer film," Optics Communications **190**(1-6), 333-337 (2001).
14. Y. J. Jia, G. M. Wang, B. Guo, W. Su, and Q. J. Zhang, "An all-optical poling investigation of low absorbing azobenzene side-chain polymer films," Journal Of Optics A-Pure And Applied Optics **6**(9), 833-836 (2004).
15. B. Guo, F. S. Liu, L. J. Zhu, Y. Chen, Q. J. Zhang, and G. M. Wang, "Study on the all-optical poling behavior of a series of side-chain azo copolymers and homopolymer," Journal Of Optoelectronics And Advanced Materials **7**(3), 1523-1528 (2005).
16. N. Tsutsumi and T. Shingu, "chi((2)) holography induced by all-optical poling," Chemical Physics Letters **403**(4-6), 420-424 (2005).
17. A. Apostoluk, "Dynamique de la polarisation tout-optique de molécules organiques présentant un photochromisme rapide en phase polymérisée," (Université d'Angers, Angers, 2003).
18. C. Fiorini, "Propriétés Optiques Non-lineaires du Second Ordre Induites Par Voie Optique Dans Les Milieux Moleculaires," (Université de Paris-Sud U.F.R. Scientifique d'Orsay, Paris, 1995).
19. H. Hoshi and H. Takezoe, "Optical second-harmonic generation in ferroelectric liquid crystals with a twist defect," Physics Letters A **358**(3), 242-244 (2006).
20. K. M. Ok, E. O. Chi, and P. S. Halasyamani, "Bulk characterization methods for non-centrosymmetric materials: second-harmonic generation, piezoelectricity, pyroelectricity, and ferroelectricity," Chemical Society Reviews **35**(8), 710-717 (2006).
21. T. V. Galstian, E. Brasselet, and D. Dumont, "Resonant optical torque in dichroic azo dye doped nematic liquid crystals," Molecular Crystals And Liquid Crystals **375**, 593-606 (2002).
22. D. Dantsker, J. Kumar, and S. K. Tripathy, "Optical alignment of liquid crystals," Journal Of Applied Physics **89**(8), 4318-4325 (2001).

23. M. Nollmann, D. Shalom, P. Etchegoin, and J. Sereni, "Photobleaching and reorientational dynamics of dyes in a nematic liquid crystal," Physical Review E **59**(2), 1850-1859 (1999).
24. A. C. Etile, C. Fiorini, F. Charra, and J. M. Nunzi, "Phase-coherent control of the molecular polar order in polymers using dual-frequency interferences between circularly polarized beams," physical review A **56**(5), 3888-3896 (1997).
25. S. C. Kuebler, A. Heuer, and H. W. Spiess, "Glass transition of polymers: Memory effects in structural relaxation of polystyrene," Physical Review E **56**(1), 741-749 (1997).
26. G. P. Johari and Goldstei.M, "Viscous Liquids And Glass Transition.2. Secondary Relaxations In Glasses Of Rigid Molecules," Journal Of Chemical Physics **53**(6), 2372-& (1970).
27. G. Williams and D. C. Watts, "Non-Symmetrical Dielectric Relaxation Behaviour Arising From A Simple Empirical Decay Function," Transactions Of The Faraday Society **66**(565P), 80-& (1970).
28. M. F. Shlesinger and E. W. Montroll, "On The Williams-Watts Function Of Dielectric-Relaxation," Proceedings Of The National Academy Of Sciences Of The United States Of America-Physical Sciences **81**(4), 1280-1283 (1984).
29. M. D. Ediger, T. Inoue, M. T. Cicerone, and F. R. Blackburn, "Probe rotation near and below the glass transition temperature: Relationship to viscoelasticity and physical aging," Macromolecular Symposia **101**, 139-146 (1996).
30. P. A. O'Connell and G. B. McKenna, "Arrhenius-type temperature dependence of the segmental relaxation below T-g," Journal Of Chemical Physics **110**(22), 11054-11060 (1999).
31. M. Paluch, C. M. Roland, S. Pawlus, J. Ziolo, and K. L. Ngai, "Does the arrhenius temperature dependence of the Johari-Goldstein relaxation persist above T-g?" Physical Review Letters **91**(11)(2003).
32. C. S. Paik and H. Morawetz, "Photochemical And Thermal Isomerization Of Azoaromatic Residues In Side Chains And Backbone Of Polymers In Bulk," Macromolecules **5**(2), 171-& (1972).
33. M. A. Pauley, H. W. Guan, and C. H. Wang, "Poling dynamics and investigation into the behavior of trapped charge in poled polymer films for nonlinear optical

applications," Journal Of Chemical Physics **104**(17), 6834-6842 (1996).

34. M. A. Pauley, C. H. Wang, and A. K. Y. Jen, "Poling dynamics and effects of trapped charge in poled polymer films for nonlinear optical applications," Macromolecules **29**(22), 7064-7074 (1996).
35. Q. Shen and K. Y. Wong, "Improved thermal stability of poled polymers by optimized physical aging process," Optics Communications **164**, 47-50 (1999).
36. K. Y. Wong and Q. Shen, "Effects of physical aging on the relaxation of poled nonlinear optical polymers," Journal Of Applied Physics **86**(6), 2953-2958 (1999).
37. V. Rodriguez, F. Adamietz, L. Sanguinet, T. Buffeteau, and C. Sourisseau, "Quantitative determination of the polar order induced under high electric field in amorphous PDR1M azobenzene polymer films," Journal Of Physical Chemistry B **107**(36), 9736-9743 (2003).
38. K. D. Singer, M. G. Kuzyk, and J. E. Sohn, "2nd-Order Nonlinear-Optical Processes In Orientationally Ordered Materials - Relationship Between Molecular And Macroscopic Properties," Journal Of The Optical Society Of America B-Optical Physics **4**(6), 968-976 (1987).
39. V. Rodriguez, F. Lagugne-Labarthet, and C. Sourisseau, "Orientation distribution functions based upon both (P-1), (P-3) order parameters and upon the four (P-1) up to (P-4) values: Application to an electrically poled nonlinear optical azopolymer film," Applied Spectroscopy **59**(3), 322-328 (2005).
40. J. C. Hooker, W. R. Burghardt, and J. M. Torkelson, "Birefringence and second-order nonlinear optics as probes of polymer cooperative segmental mobility: Demonstration of Debye-type relaxation," Journal Of Chemical Physics **111**(6), 2779-2788 (1999).
41. M. S. Beevers and G. Williams, "A Consideration Of Orientational Correlation-Functions, Time-Dependent Distribution-Functions And Pictorial Representations Of The Orientational Motions Of Molecules," Advances In Molecular Relaxation And Interaction Processes **16**(3), 175-193 (1980).
42. K. Zimmerman, F. Ghebremichael, M. G. Kuzyk, and C. W. Dirk, "Electric-Field-Induced Polarization Current Studies In Guest-Host Polymers," Journal Of Applied Physics **75**(3), 1267-1285 (1994).

43. J. G. Victor and J. M. Torkelson, "On Measuring The Distribution Of Local Free-Volume In Glassy-Polymers By Photochromic And Fluorescence Techniques," Macromolecules **20**(9), 2241-2250 (1987).

44. T. K. Kwei, E. M. Pearce, J. R. Pennacchia, and M. Charton, "Correlation Between The Glass-Transition Temperature Of Polymer Mixtures And Intermolecular Force Parameters," Macromolecules **20**(5), 1174-1176 (1987).
45. C. Fiorini, F. Charra, J. M. Nunzi, I. D. W. Samuel, and J. Zyss, "Light-induced second-harmonic generation in an octupolar dye," Optics Letters **20**(24), 2469-2471 (1995).
46. C. Fiorini, J. M. Nunzi, P. Raimond, C. Branger, M. Lequan, and R. M. Lequan, "Symmetry of the all-optical orientation dynamics of an octupolar azo-dye salt," Synthetic Metals **115**(1-3), 127-131 (2000).
47. G. Xu, X. Liu, J. Si, P. Ye, Z. Li, and Y. Shen, "Optical poling in a crosslinkable polymer system," Applied Physics B-Lasers And Optics **68**(4), 693-696 (1999).
48. B. Sturman, E. Podivilov, and M. Gorkunov, "Origin of stretched exponential relaxation for hopping-transport models," Physical Review Letters **91**(17)(2003).
49. R. K. Iler, "Multilayers Of Colloidal Particles," Journal of Colloid and Interface science **21**(6), 569 (1966).
50. G. Decher and J. D. Hong, "Buildup Of Ultrathin Multilayer Films By A Self-Assembly Process.2. Consecutive Adsorption Of Anionic And Cationic Bipolar Amphiphiles And Polyelectrolytes On Charged Surfaces," Berichte Der Bunsen-Gesellschaft-Physical Chemistry Chemical Physics **95**(11), 1430-1434 (1991).
51. G. Decher, J. D. Hong, and J. Schmitt, "Buildup Of Ultrathin Multilayer Films By A Self-Assembly Process.3. Consecutively Alternating Adsorption Of Anionic And Cationic Polyelectrolytes On Charged Surfaces," Thin Solid Films **210**(1-2), 831-835 (1992).
52. Y. Zong, K. Tawa, B. Menges, J. Ruhe, and W. Knoll, "Azobenzene-containing polyamic acid with excellent Langmuir-Blodgett-Kuhn film formation behavior suitable for all-optical switching," Langmuir **21**(15), 7036-7043 (2005).
53. K. Y. K. Man, H. L. Wong, W. K. Chan, A. B. Djurisic, E. Beach, and S. Rozeveld, "Use of a ruthenium-containing conjugated polymer as a photosensitizer in photovoltaic devices fabricated by a layer-by-layer deposition process," Langmuir **22**(7), 3368-3375 (2006).
54. J. W. Baur, S. Kim, P. B. Balanda, J. R. Reynolds, and M. F. Rubner, "Thin-film light-emitting devices based on sequentially adsorbed multilayers of water-soluble poly(p-phenylene)s," Advanced Materials **10**(17), 1452-1455 (1998).
55. S. H. Lee, S. Balasubramanian, D. Y. Kim, N. K. Viswanathan, S. Bian, J. Kumar, and S. K. Tripathy, "Azo polymer multilayer films by electrostatic self-assembly

and layer-by-layer post azo functionalization," Macromolecules **33**(17), 6534-6540 (2000).

56. R. Advincula, Y. F. Wang, and M. K. Park, "Photoisomerization and aggregation behavior of DNA/poly-lysine/azobenzene dye ultrathin films: Substrates for optobioelectronic applications," Abstracts Of Papers Of The American Chemical Society **219**, U449-U449 (2000).

57. M. F. Durstock, R. J. Spry, J. W. Baur, B. E. Taylor, and L. Y. Chiang, "Investigation of electrostatic self-assembly as a means to fabricate and interfacially modify polymer-based photovoltaic devices," Journal Of Applied Physics **94**(5), 3253-3259 (2003).
58. H. Mattoussi, M. F. Rubner, F. Zhou, J. Kumar, S. K. Tripathy, and L. Y. Chiang, "Photovoltaic heterostructure devices made of sequentially adsorbed poly(phenylene vinylene) and functionalized C-60," Applied Physics Letters **77**(10), 1540-1542 (2000).
59. J. van den Beucken, X. F. Walboomers, O. C. Boerman, M. R. J. Vos, N. Sommerdijk, T. Hayakawa, T. Fukushima, Y. Okahata, R. J. M. Nolte, and J. A. Jansen, "Functionalization of multilayered DNA-coatings with bone morphogenetic protein 2," Journal Of Controlled Release **113**(1), 63-72 (2006).
60. F. Yamauchi, Y. Koyamatsu, K. Kato, and H. Iwata, "Layer-by-layer assembly of cationic lipid and plasmid DNA onto gold surface for stent-assisted gene transfer," Biomaterials **27**(18), 3497-3504 (2006).
61. Y. Zhou, R. Z. Ma, Y. Ebina, K. Takada, and T. Sasaki, "Multilayer hybrid films of titania semiconductor nanosheet and silver metal fabricated via layer-by-layer self-assembly and subsequent UV irradiation," Chemistry Of Materials **18**(5), 1235-1239 (2006).
62. H. Paloniemi, M. Lukkarinen, T. Aaritalo, S. Areva, J. Leiro, M. Heinonen, K. Haapakka, and J. Lukkari, "Layer-by-layer electrostatic self-assembly of single-wall carbon nanotube polyelectrolytes," Langmuir **22**(1), 74-83 (2006).
63. J. L. Casson, H. L. Wang, J. B. Roberts, A. N. Parikh, J. M. Robinson, and M. S. Johal, "Kinetics and interpenetration of ionically self-assembled dendrimer and PAZO multilayers," Journal Of Physical Chemistry B **106**(7), 1697-1702 (2002).
64. S. H. Lee, S. Balasubramanian, D. Y. Kim, N. K. Viswanathan, S. Bian, J. Kumar, and S. K. Tripathy, "Azo polymer multilayer films by electrostatic self-assembly and layer-by-layer post azo functionalization," macromolecules **33**(17),

6534-6540 (2000).

65. Z. Sekkat, J. Wood, Y. Geerts, A. ElMeskini, M. Buchel, and W. Knoll, "Organized photochromic azo-polymeric structures: Self-assembled and Langmuir-Blodgett-Kuhn layers," Synthetic Metals **81**(2-3), 281-285 (1996).
66. S. Dante, R. Advincula, C. W. Frank, and P. Stroeve, "Photoisomerization of polyionic layer-by-layer films containing azobenzene," Langmuir **15**(1), 193-201 (1999).
67. A. Bassi, L. Misoguti, M. F. Ginani, O. N. Oliveira, C. R. Mendoca and D. S. Santos, "Spontaneous Birefringence in Layer-by-Layer Films of Chitosan and Azo Dye Sunset Yellow," Macromolecular Rapid Communications **23**(16), 975-977 (2002).
68. M. Breit, M. Gao, G. von Plessen, U. Lemmer, J. Feldmann, and S. T. Cundiff, "Formation dynamics of layer-by-layer self-assembled films probed by second harmonic generation," Journal Of Chemical Physics **117**(8), 3956-3960 (2002).
69. Y. Shimazaki, S. Ito, and N. Tsutsumi, "Adsorption-induced second harmonic generation from the layer-by-layer deposited ultrathin film based on the charge-transfer interaction," Langmuir **16**(24), 9478-9482 (2000).
70. P. Fischer, M. Koetse, A. Laschewsky, E. Wischerhoff, L. Jullien, A. Persoons, and T. Verbiest, "Orientation of nonlinear optical active dyes in electrostatically self-assembled polymer films containing cyclodextrins," macromolecules **33**(26), 9471-9473 (2000).
71. K. M. Lenahan, Y. X. Wang, Y. J. Liu, R. O. Claus, J. R. Heflin, D. Marciu, and C. Figura, "Novel polymer dyes for nonlinear optical applications using ionic self-assembled monolayer technology," Advanced Materials **10**(11), 853-+ (1998).
72. M. J. Roberts, G. A. Lindsay, W. N. Herman, and K. J. Wynne, "Thermally stable nonlinear optical films by alternating polyelectrolyte deposition on hydrophobic substrates," Journal Of The American Chemical Society **120**(43), 11202-11203 (1998).
73. A. Apostoluk, D. Chapron, G. Gadret, B. Sahraoui, L. M. Nunzi, C. Fiorini-Debuisschert, and P. Raimond, "Quasi-phase-matched gratings printed by all-optical poling in polymer films," Optics Letters **27**(22), 2028-2030 (2002).
74. H. G. M. Vandesteeg, M. A. C. Stuart, A. Dekeizer, and B. H. Bijsterbosch, "Polyelectrolyte Adsorption - A Subtle Balance Of Forces," Langmuir **8**(10), 2538-2546 (1992).
75. O. A. Evers, J. Scheutjens, and G. J. Fleer, "Statistical Thermodynamics Of Block

Copolymer Adsorption.1. Formulation Of The Model And Results For The Adsorbed Layer Structure," macromolecules **23**(25), 5221-5233 (1990).

76. G. Aldea, H. Gutierrez, J.-M. Nunzi, G. Chitanu, M. Sylla, and B. C. Simionescu, "Second harmonic generation diagnostic of layer-by-layer deposition from Disperse Red 1 - functionalized maleic anhydride copolymer," Optical Materials 2006 in press.
77. K. D. Singer and A. F. Garito, "Measurements Of Molecular 2nd Order Optical Susceptibilities Using Dc Induced 2nd Harmonic-Generation," Journal Of Chemical Physics **75**(7), 3572-3580 (1981).
78. S. W. Chan, J. M. Nunzi, A. Quatela, and M. Casalboni, "Retardation of orientation relaxation of azo-dye doped amorphous polymers upon all-optical poling," Chemical Physics Letters **428**(4-6), 371-375 (2006).
79. S. W. Chan, A. Quatela, M. Casalboni, and J.-M. Nunzi, "Retardation of the orientation relaxation of azo-dye doped amorphous polymers upon photo-induced isomerization," Proceeding of SPIE **6331** (2006).
80. E. Ortyl, S. W. Chan, J. M. Nunzi, and S. Kucharski, "Second harmonic generation by all-optical poling and its relaxation in the polymer films containing azo sulfonamide chromophores," Optical Materials **29**, 268-272 (2006).
81. R. A. Pethrick, "Positron annihilation - A probe for nanoscale voids and free volume?" Progress In Polymer Science **22**(1), 1-47 (1997).

CHAPTER 3

NONLINEAR OPTICAL CHARACTERIZATION OF ZINC OXIDE FROM MILLI-METER to NANO-METER

Semi-conducting zinc oxide (ZnO) is one of the best material for opto-electronic industry because of it is easy in production, it is environmental friendly besides its high valuable photo-electronic properties. In addition, its properties of wide band-gap[1] (~3.37eV), high exciton binding energy (60meV) and low electrical resistance assure its importance for the fabrication of short-wavelength optoelectronic devices like ultraviolet (UV) light emitting diodes, diode lasers, transparent device electrodes[2], etc. Moreover, it offers numerous possibilities for applications in the micro-optoelectronic industry providing that it is grown epitaxially and exhibits nano-scale geometrical structure such as nanowire, nanorod and nanoring[3]. For instance, researchers demonstrated that a ZnO nanorod (ZnONR) can be acted as an optical cavity for UV lasing[4]. Nanorod structure was also introduced as building block of solar cells to enhance charge transport efficiency[5-7]. The properties of high conductivity and high electric field emission capability of nanorods are applied in the manufacturing of efficient biochemical sensors, optical switches and field-emission display devices[8-10].

Multiples new photo-electronic properties of ZnO emerge when grain size of ZnO becomes smaller and smaller. Correlation between geometrical characterization of ZnO (from bulk-scale (mm) to nano-scale (nm)) and its photo-electronic properties would be a necessity of understanding both in the sense of physics acquisition and suitability of their application. In this chapter, second order nonlinear optical properties of ZnO, scaling from bulk (single crystal) to nano-size (ZnONR) would be studied with far-field Second Harmonic Generation (SHG).

In this chapter, we will discuss second order NLO susceptibility of ZnO single crystal and ZnONR, effect of NR geometry and dielectric environment to its NLO susceptibility under different geometry of SHG measurement.

3.1 SHG of bulk ZnO single crystal

3.1.1 Fabrication of zinc oxide single crystal

Zinc oxide (ZnO) is a member of wurzite crystal family[8] where its single crystalline structure exhibits hexagonal close packing (h.c.p.) lattice structure as shown in figure 3.1 below :

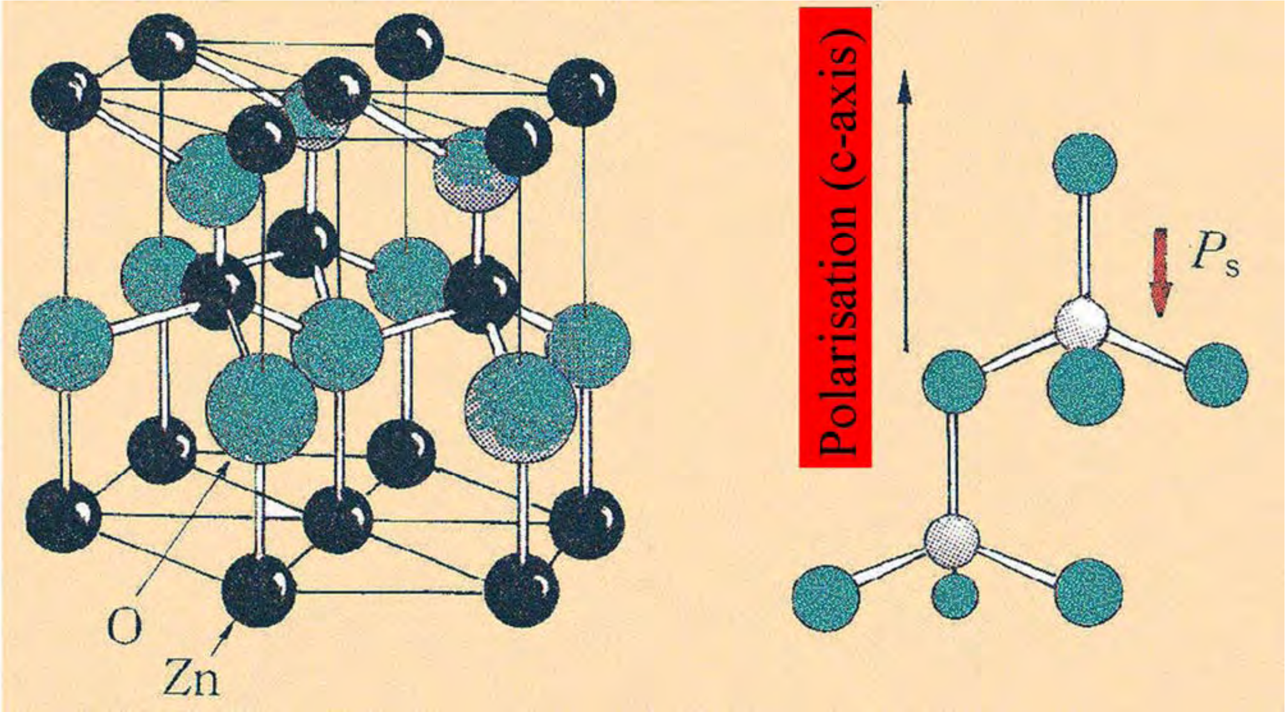

Figure 3.1 Hexagonal close packing lattice structure of ZnO single crystal

The lattice constant at 300 K of ZnO[11] is : A single ZnO crystal of size 10 mm x 10 mm and thickness 0.5 mm was employed for studying its second order NLO response via SHG. The ZnO single crystal, purchased from MTI corp., was fabricated by hydro-thermal process[12]. The process of its fabrication is depicted following in figure 3.2 :

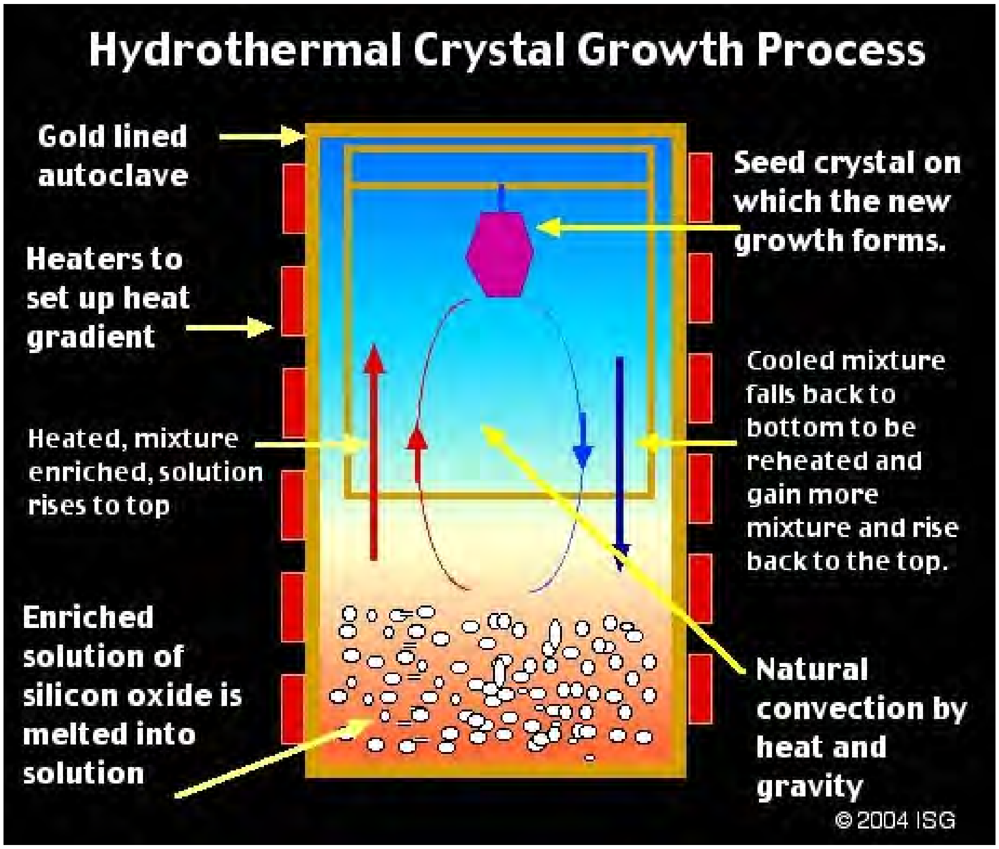

Extracted from:http://emeralds.alexandrite.ch/

Figure 3.2 Hydro-thermal fabrication process of ZnO single crystal

The orientation of the crystal growth is <0001> which infers that polar c-axis of lattice is normal to the crystal surface. X-ray diffraction measurement (Siemens D5000) of single crystal shown below in figure 3.3 confirm the perfect <0001> crystallinity of the ZnO single crystal sample.

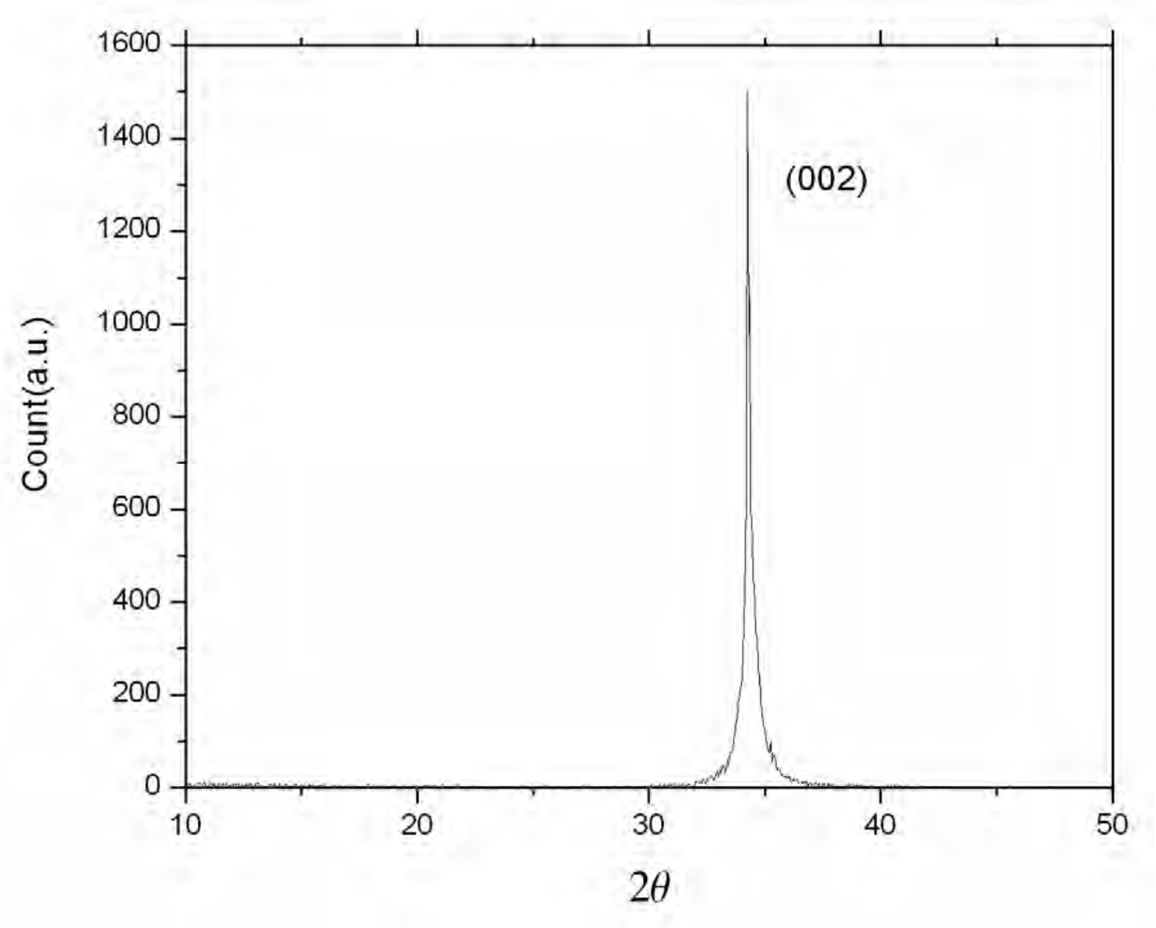

Figure 3.3 X-ray diffraction (XRD) measurement of ZnO single crystal

3.1.2 Second Harmonic Generation (SHG) of Zinc oxide single crystal

From late 60's to early 70's, B. F. Levine[13], C. Flytzanis *et al.*[14] and R. C. Miller *et al.*[15, 16] did a lot of pioneering works on second order NLO properties of II-VI semiconductors including ZnO. Second order NLO susceptibilities of ZnO and their relative signs were obtained theoretically and experimentally. For ZnO single crystal, with the assignment of laboratory z-axis as the crystal polar c-axis, the 6mm point group symmetry[17] gives 3 non-vanishing second order NLO susceptibilities $\chi^{(2)}_{zxx}$, $\chi^{(2)}_{xzx}$ and $\chi^{(2)}_{zzz}$. Their values are : $\chi^{(2)}_{zxx} = \chi^{(2)}_{xzx} \sim 4$ pm/V and $\chi^{(2)}_{zzz} \sim -14$ pm/V.

For the determination of second order NLO susceptibilities of the ZnO single crystal, SHG measurement at p-in/p-out configuration was performed for obtaining curve fitting value of second order NLO susceptibilities of ZnO single crystal. Detail of experimental setup of SHG measurement is presented in section 4.2 of chapter 4. A x-cut quartz crystal (L=2.0 mm, $\chi^{(2)}_{eff}$=0.6 pm/V) was used as calibration reference. SHG signal (p-in/p-out) as function of incident angle θ_{in} to normal (z-axis) and its data fitting according to equation 1.22 is shown in figure 3.4 :

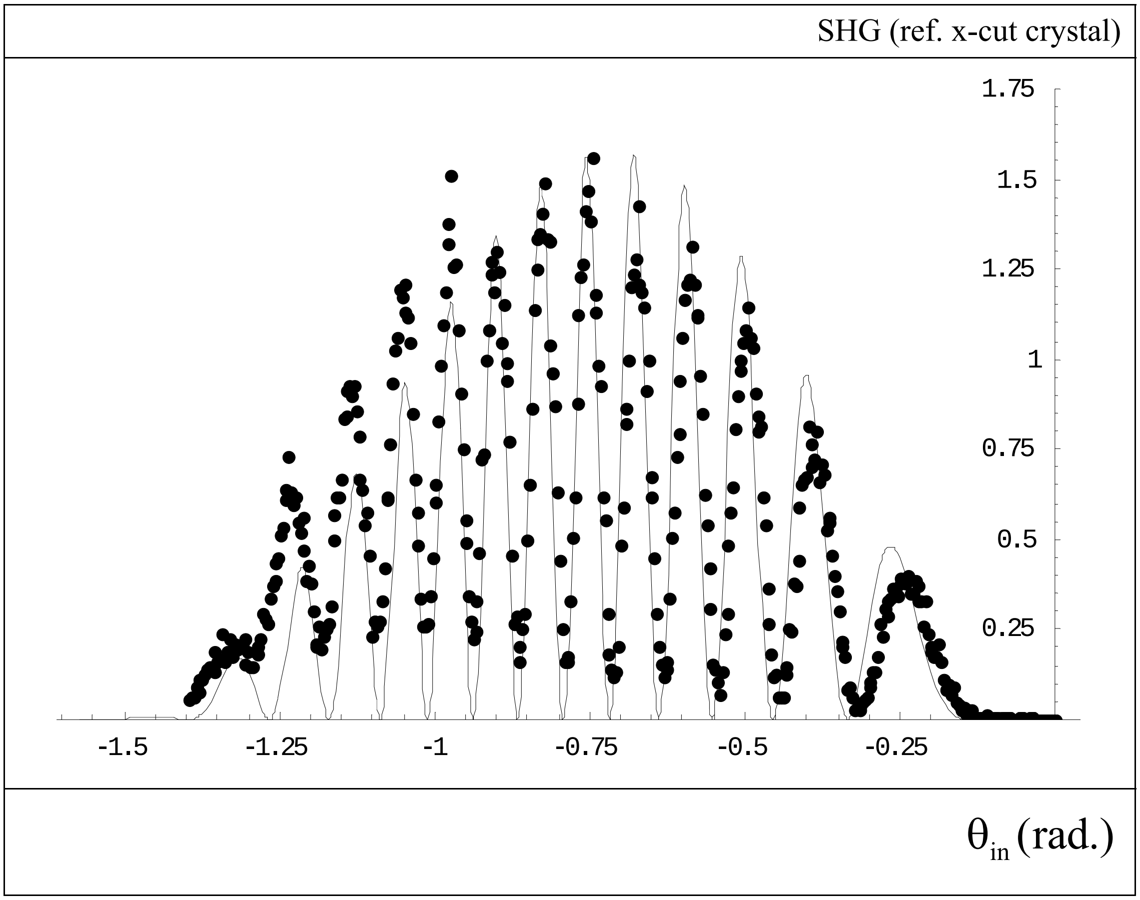

Figure 3.4 SHG (p-in/p-out) vs incident angle θ_{in} (rad.) of ZnO single crystal and its data fitting (solid line)

The fitting values of second order NLO susceptibilities $\chi^{(2)}_{zzz}$, $\chi^{(2)}_{xzx}$ and $\chi^{(2)}_{zxx}$ are shown in table 3.1 together with the results from theoretical calculation :

	Theoretical calculation	Experimental result
$\chi^{(2)}_{zzz}$ (pm/V)	-14	-16.54
$\chi^{(2)}_{xzx}$ (pm/V)	4	4.06
$\chi^{(2)}_{zxx}$ (pm/V)	4	4.46

Table 3.1 Theoretical and experimental values of second order NLO susceptibilities of ZnO single crystal

According to table 3.1, the experimental values of $\chi^{(2)}$ obtained in our SHG measurement are consistent to those results obtained from theoretical calculation based on bound charge approximation[13, 18] in quantum mechanical calculation. In the following section, we will pass from milli-scale ZnO crystal to nano-scale ZnO crystal, studying further the second order NLO response from ZnO nano-structure.

3.2 Second order NLO response of as-grown ZnO nanorod

ZnO nano-structures such as nanowire, nanorod and nanoring offer numerous possibilities for applications in micro-optoelectronic field.

Frequency conversion with nano-structures plays an important role in nano-optoelectronic device applications. Saykally *et al*[19]. measured microscopic second and third order NLO susceptibilities of a single ZnO nanorod by near-field scanning optical microscopy (NSOM). In this section, we present the optical SHG measurement of macroscopic second-order NLO susceptibilities ($\chi^{(2)}_{zzz}$ and $\chi^{(2)}_{zxx}$) of ZnO nanorods grown on quartz substrate by hydro-thermal method. Until now, macroscopic second order NLO property of well aligned ZnO nanorod thin-films has not been reported in detail.

Furthermore, second-order NLO susceptibilities were also obtained and compared regarding to the structural parameters (Aspect ratio) of as-grown ZnONR. The effect of gas annealing and dielectric property of environment of ZnONR to its second order NLO susceptibilities will also be addressed and discussed.

3.2.1 Fabrication of ZnO nano-structure

A layer of ZnO nanocrystal nucleation site was coated on quartz substrate as a seed for nanorod growth. ZnO nanocrystal nucleation site was directly formed on substrates by thermally decomposing zinc acetate ($Zn(C_2H_3O_2)_2$) (Aldrich) at 350 ºC. Before employing zinc acetate for preparing ZnO nanocrystal nucleation sites, researchers[20, 21] used ZnO nanoparticles (~ 30 nm) for the introduction of the ZnO nanocrystal nucleation sites on quartz substrate. For our experiments, nucleation sites of ZnONR samples were all prepared by zinc acetate.

With the ZnO nucleation site, ZnO nanorods were then grown on the seeded substrates with equi-molar solution of zinc nitrate hexahydrate ($Zn(NO_3)_2 \cdot 6H_2O$), hexamethylenetetramine ($C_6H_{12}N_4$) and 5-7 mM of polyethylenimine (Aldrich, 50 wt.% sol. in water) at 90 degrees in a vacuum oven. The growth times were 0.25 hr, 0.75 hr, 2.5 hrs, 5 hrs and 7.5 hrs respectively. During ZnO crystal growth, samples were rinsed with de-ionized water occasionally in order to remove the residual salt on the surface for attaining higher quality (such as higher NR orderness, lower dispersion of of NR's length and NR's diameter distribution) of ZnONR sample. At last, ZnONR samples were then dried at 100 ºC. The synthesis route of ZnONR, seeded by ZnO nanocrystal or zinc acetate respectively, is shown in figure 3.5. ZnONR density on quartz substrate is 150~200 μm^{-2}. Length and diameter of ZnONR depends largely on the time of crystal growth and the concentration of the forming solution.

However, ZnONR samples grown from ZnO nanoparticle (nanocrystal) nucleation site show higher dispersive distribution of rod density and rod geometry comparing to that grown from ZnO acetate nucleation site. It can be visualized from the SEM images of figure 3.6. Generally speaking, the orderness, density and uniformity of ZnONR obtained from ZnO nano-particle seeding is less satisfactory than that obtained from ZnO acetate. For more systematic studies of ZnONR, more uniform ZnONR prepared with ZnO acetate, would be used in all of the following sections for their optical and material characterizations.

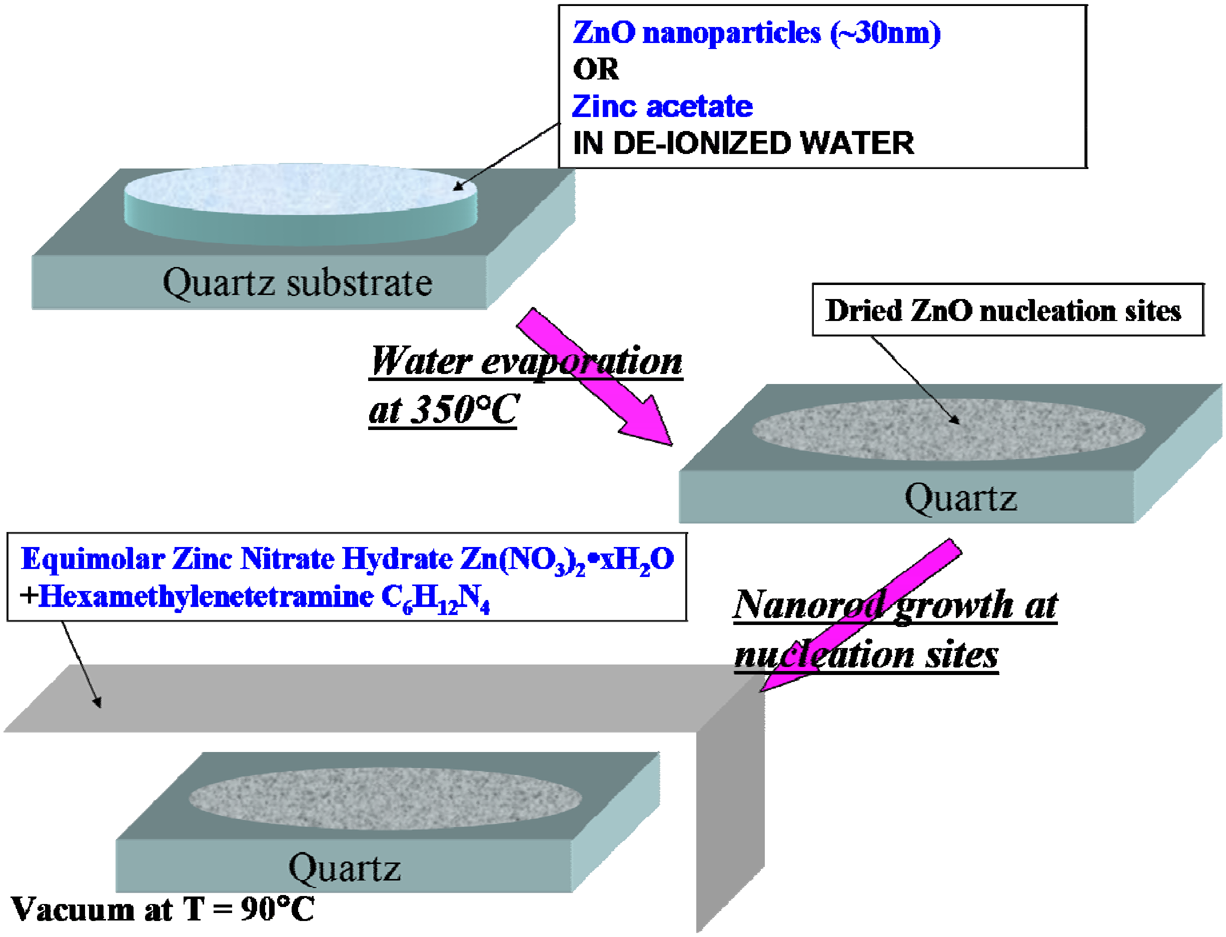

Figure 3.5 Synthesis route ZnONR seeded by ZnO nanoparticle or Zinc acetate : Quartz substrate is firstly seeded either with zinc oxide nanoparticles or zinc acetate. ZnO nanorods were then grown on the seeded substrates with equi-molar solution of zinc nitrate hexahydrate ($Zn(NO_3)_2•6H_2O$) and hexamethylenetetramine ($C_6H_{12}N_4$) at 90 degrees in a vacuum oven. The growth times were 0.25 hr, 0.75 hr, 2.5 hrs, 5 hrs and 7.5 hrs respectively. During crystal growth, ZnONR samples were then rinsed with de-ionized water occasionally in order to remove the residual salt on the surface. At last, samples were then dried at 100 ºC for complete removal of water

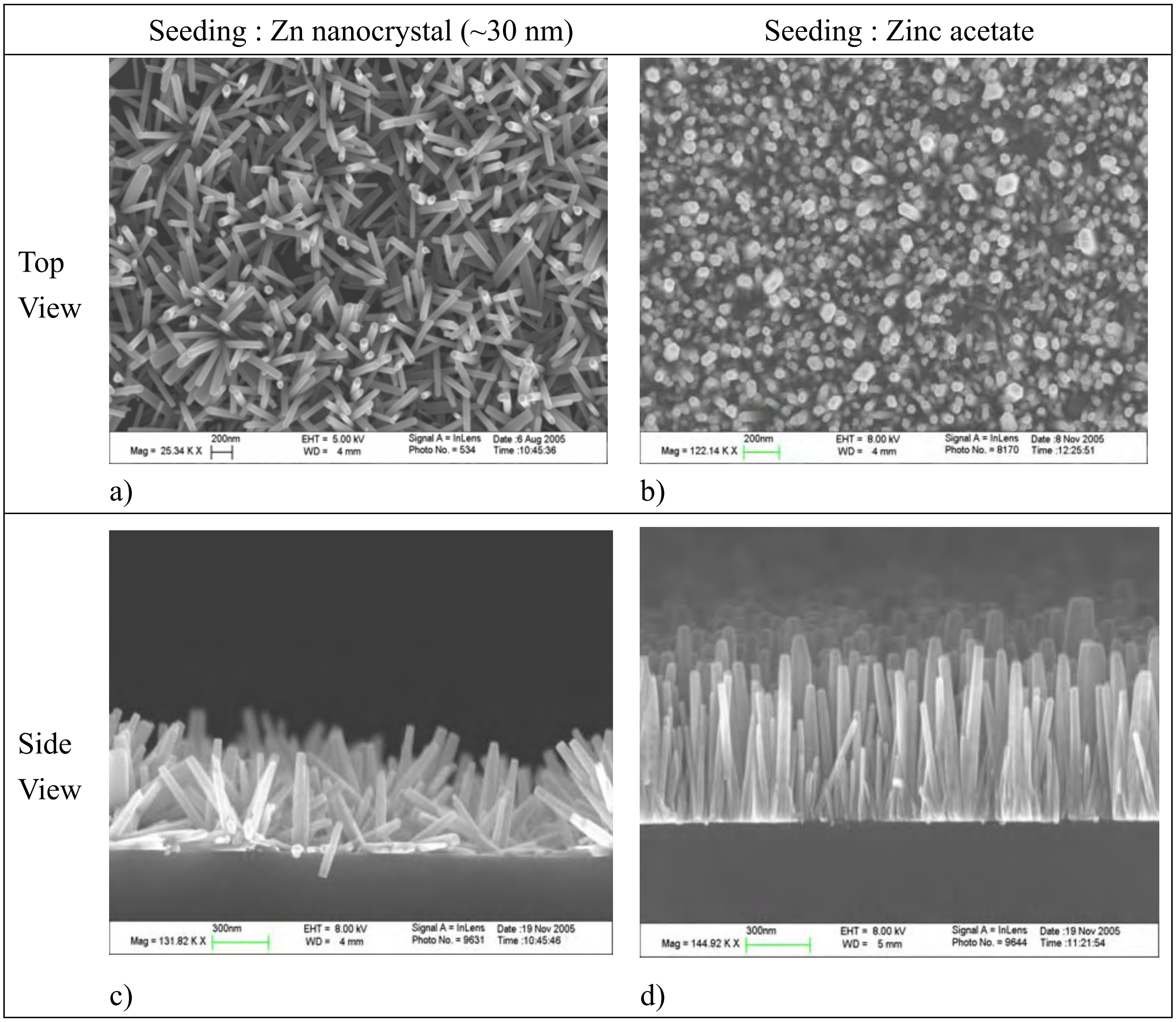

Figure 3.6 SEM images of ZnONR grown from Zn nanocrystal seed (80 mins growth) or ZnO acetate seed (45 mins growth) : a) top-view of ZnONR from Zn nanocrystal seed. b) top-view of ZnONR from Zn acetate seed. c) side-view of ZnONR from Zn nanocrystal seed. d) side-view of ZnONR from Zn acetate seed

3.2.2 Characterization of as-grown ZnONR

Geometric features (rod length and diameter) of ZnONR depend on duration of NR growth. An average (most probable) value of rod length $\overline{\ell}$ and rod diameter $\overline{d}$ are approximated by obtaining Gaussian distribution of rod length and rod diameter of ZnONR samples under different duration of growth from their SEM image. Length and diameter of approximately 500 NR were taken into account for the estimation of length and diameter distribution. NR density is around 200 μm^{-2}. Duration of the NR growth and their corresponding average rod length $\bar{\ell}$, diameter $\bar{d}$ and aspect ratio $\wp = \frac{\bar{\ell}}{\bar{d}}$ are presented in table 3.2 below :

Growth time (hr)	ave. nanorod diameter $\bar{d}$ (nm)	ave. nanorod length $\bar{\ell}$ (nm)	Aspect ratio $\wp$
0.25	**10**	**57**	**5.7**
0.75	**20**	**150**	**7.5**
2.5	**31**	**245**	**7.9**
5	**55**	**511**	**9.2**
7.5	**62**	**667**	**10.8**

Table 3.2 Average nanorod's diameter, length and aspect ratio of nanorod grown for different duration (estimation from around 500 NRs from samples under different duration of NR growth)

Transmission spectra obtained with spectroscopy Perkin-Elmer Lambda 19 of ZnONR samples were taken at normal incidence and are given in figure 3.7. It appears that the visible transmission near the band-edge decreases with increasing NR length, which is relevant of scattering in the transmission region.

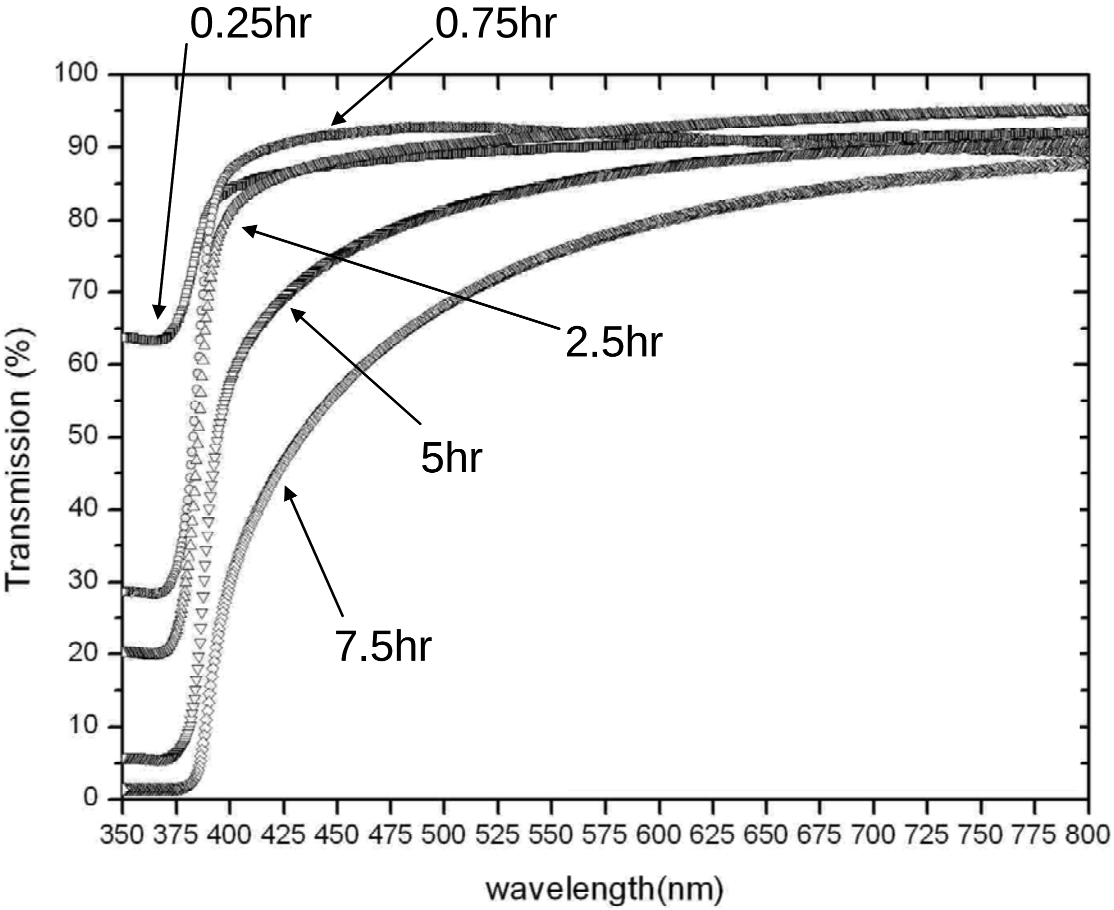

Figure 3.7 Transmission spectra of ZnONR samples grown for different duration (hr)

In addition, Photoluminescence (PL) properties of as-grown ZnONR samples were reported recently emerging some PL emissions at yellow, red and green light regions. Such visible PL emissions, as shown in figure 3.8, were not observed in ZnO bulk single crystal. Researchers[21-28] ascribed such visible light PL emissions to the defect effect which are situated both in the bulk and on the surface of the ZnONR. In the forthcoming section, effect of various defect population and its characteristics as well as its second order NLO properties will be discussed more in detail.

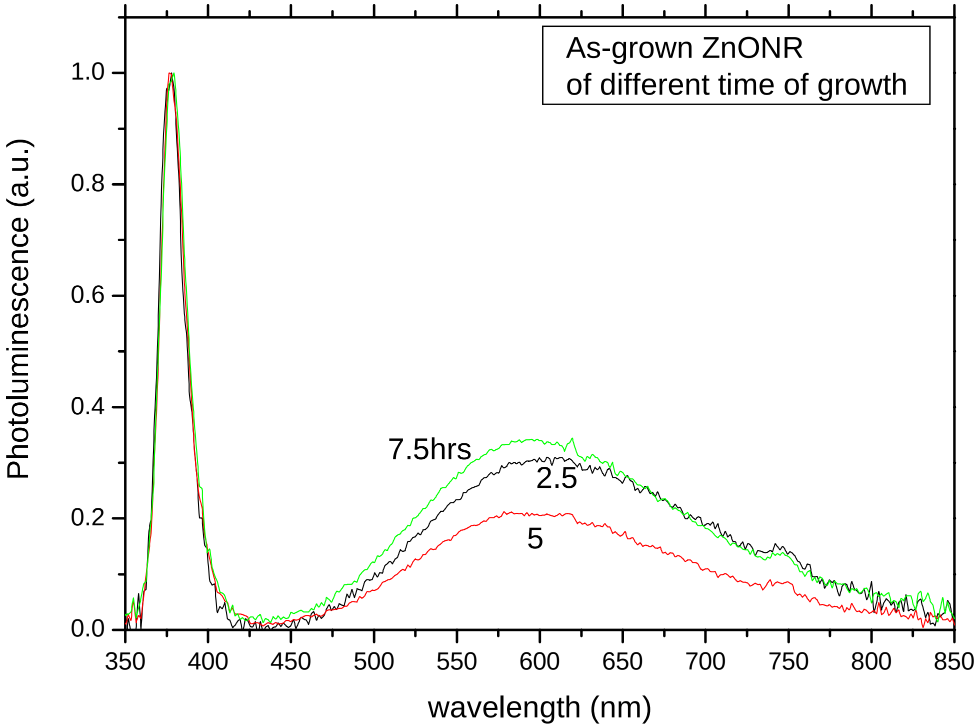

Figure 3.8 Photoluminescence (PL) of as-grown ZnONR
upon different time (2.5 hrs, 5 hrs and 7.5 hrs) of preparation

As same as ZnO single crystal, ZnONR is a polar crystal. In order to characterize and compare the second order NLO properties of ZnO single crystal and ZnONR, we would have to access the crystalline structure of ZnONR. XRD measurement was performed on ZnONR which indicates that ZnONR crystal rod grows uniformly (at growth direction <0001> as that of the ZnO single crystal) with high crystallinity as shown below in figure 3.9. In addition with the hexagonal columniform feature of SEM image for ZnONR, we could confirm that ZnONR grow longitudinally along polar c-axis. According to figure 3.9, we notice that there are three small peaks which do not exist in XRD spectra of ZnO <0001> single crystal. We attribute them to the imperfect orientation of nanorods normal to the substrate surface which leads to XRD signal from other crystal facets.

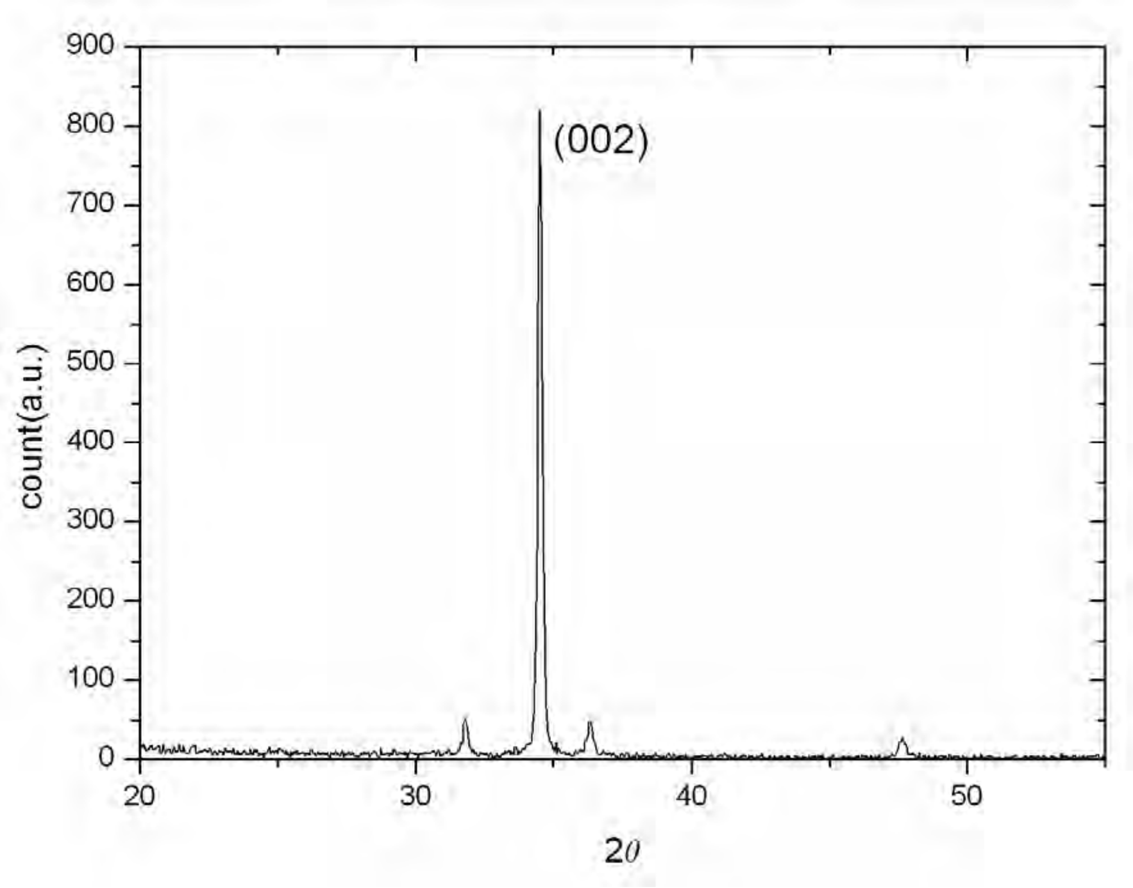

Figure 3.9 X-ray diffraction (XRD) spectra of ZnONR grown for 5 hrs (on silicate substrate)

3.2.3 SHG of as-grown ZnONR

Second Harmonic Generation (SHG) of ZnONR was measured at room temperature and under atmospheric pressure by the Maker fringes technique to determine the macroscopic second-order nonlinear optical (NLO) susceptibilities ($\chi^{(2)}_{zzz}$ and $\chi^{(2)}_{zxx}$) of the samples. Description of the experimental setup for SHG measurement can be found in the section 4.2. A schematic diagram of the SHG measurement setup is shown in Figure 4.5. A Q-switched Nd:YAG laser (Quantel YG-580) provided the fundamental beam (λ = 1064 nm, 8 ns) at frequency of 10 Hz. Second Harmonic (SH) signal from ZnONR samples was detected by a photo-multiplier tube (PMT, Hamamatsu R1828-01) and then further processed with a signal integrating oscilloscope. A Zinc oxide <0001> single crystal was used to provide SHG referencing and to minimize the experimental error due to fundamental beam energy fluctuations.

The SH signal power from ZnO nanorod samples can be expressed as[29] :

$$P_{2\omega} = \frac{32\pi^3}{cA} \frac{[t_{af}^1]^4 [t_{fs}^2]^2 [t_{sa}^2]^2}{{n_{2\omega}}^2 {c_{2\omega}}^2} P_\omega^2 \left(\frac{2\pi l}{\lambda}\right)^2 e^{-2\delta_{2\omega}} \frac{\sin^2\Psi + \sinh^2\delta_{2\omega}}{\Psi^2 + {\delta_{2\omega}}^2} \chi_{eff}^{(2)2} \tag{3.1}$$

Where : l is thickness of sample (NR length), [$\mathbf{t}^i_{jk}$] are the Fresnel transmission coefficients of fundamental (ω) and SH (2ω) beams at different interfaces; A is the area of the laser beam spot; $\delta_{2\omega}$ is the absorption coefficient times length at SH of the samples; $\Psi=(2\pi l/\lambda)(n_\omega\cos\theta_\omega - n_{2\omega}\cos\theta_{2\omega})$ is the phase mismatch parameter; P_ω and $P_{2\omega}$ are the power of incident fundamental beam and SH output beams; d_{eff} is the effective second-order nonlinear optical (NLO) coefficient. Some research groups employed the SHG equation by Jerphagnon and Kurtz[30] to analyze SHG signal from ZnO crystalline thin films. Instead, we employed the SHG equation (equation 1.22) suggested by Herman and Hayden which accounts for absorption of the SH beam which might not be negligible for ZnO nanorod samples, as shown in Figure 3.7. We have already shown in section 1.4 that sample absorption accounts greatly on the correct determination of second order NLO susceptibilities. In addition with Kleinman's non-resonant-interaction approximation[31, 32], the number of non-vanishing second-order NLO coefficients is reduced to two: $\chi_{zzz}^{(2)}$ and $\chi_{zxx}^{(2)}$.

A s-polarized fundamental beam was sent to the samples at different incident angles (*θ*) relative to the surface normal (z-axis). A p-polarized SH output signal was then measured. Under this scheme (s-in/p-out), the effective nonlinear optical coefficient $\chi_{eff}^{(2)}$ is expressed as :

$$\chi_{eff}^{(2)} = \chi_{zxx}^{(2)} \sin\theta_{2\omega} \tag{3.2}$$

In s-in/p-out configuration, $\chi_{eff}^{(2)}$ depends only on $\chi_{zxx}^{(2)}$. By fitting the SH signal data, we thus obtain the value of the NLO coefficient $\chi_{zxx}^{(2)}$, which can be introduced into data fitting in the p-in/p-out configuration. In this second configuration, the effective nonlinear optical coefficient $\chi^{(2)}_{\text{eff}}$ depends on both $\chi^{(2)}_{\text{zxx}}$ and $\chi^{(2)}_{\text{zzz}}$:

$$\chi^{(2)}_{\text{eff}} = \chi^{(2)}_{\text{zxx}}\left(\sin\theta_{2\omega}\cos^2\theta_{\omega} + \cos\theta_{2\omega}\sin2\theta_{\omega}\right) + \chi^{(2)}_{\text{zzz}}\sin\theta_{2\omega}\sin^2\theta_{\omega} \qquad (3.3)$$

Figure 3.10a-e shows the SHG intensities versus incident angle (θ) of as-grown ZnO nanorods with different growth time in s-in/p-out and p-in/p-out configurations and their experimental data fittings according to equations 3.1-3.3.

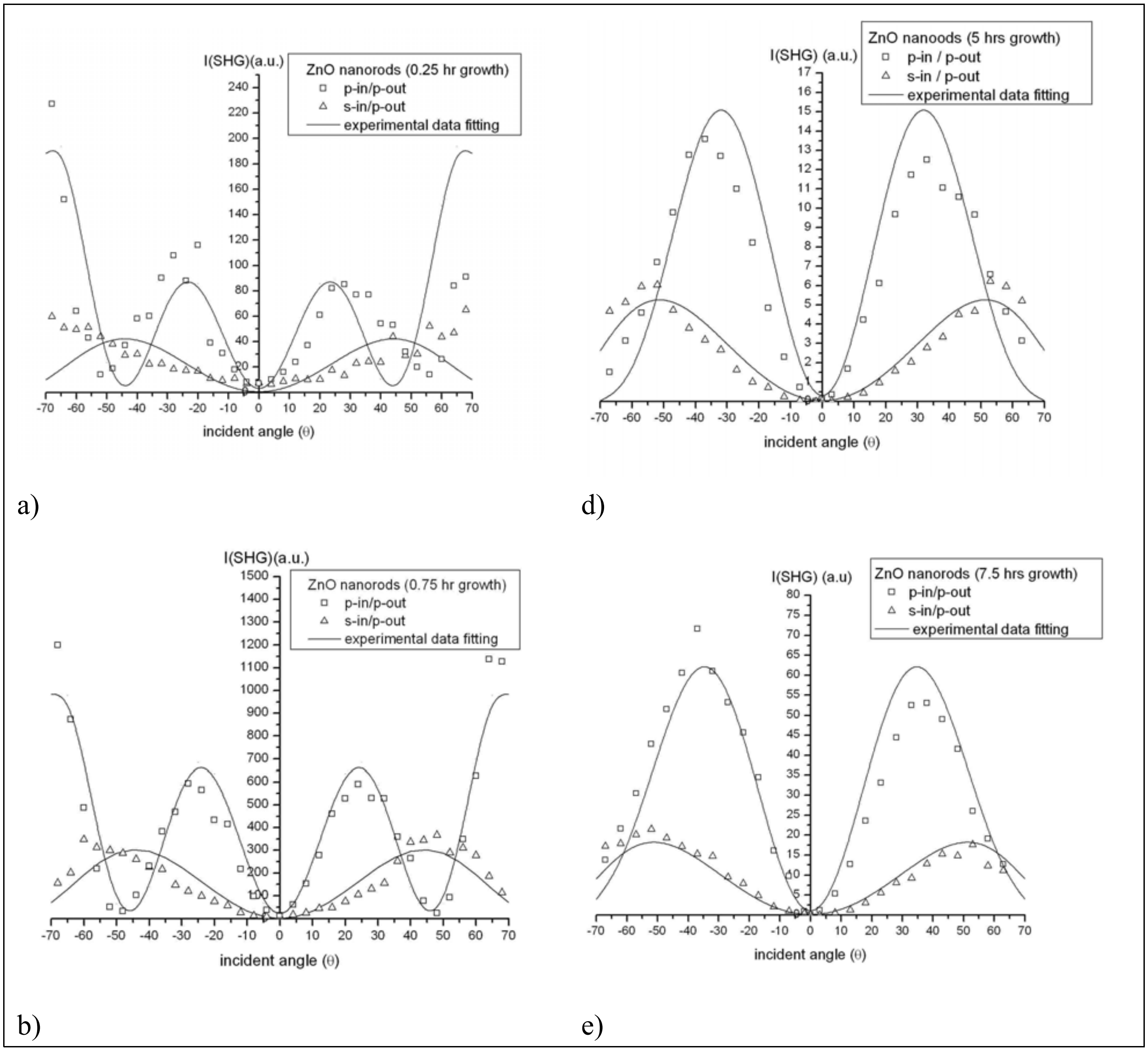

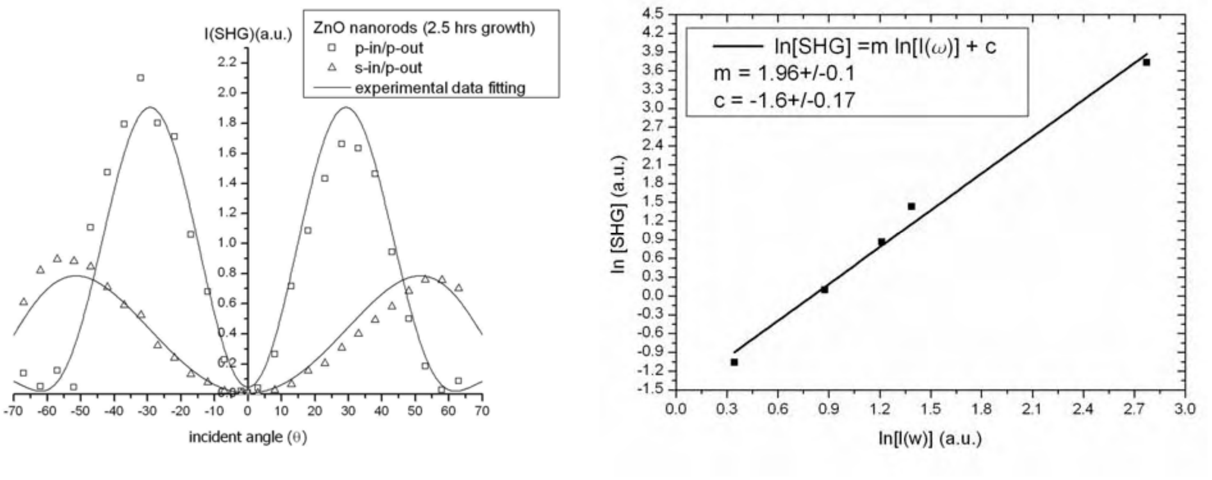

c) f)

Figure 3.10 SHG (s-in/p-out, p-in/p-out) with respect to incident angle θ_{in} of as-grown ZnONR of different duration of NR growth : a) 0.25 hr b) 0.75 hr c) 2.5 hrs d) 5 hrs e) 7.5 hrs f) Ln-Ln plot and its linear fitting of SH intensity with respect to fundamental intensity

In figure 3.10f, SHG signal in function of fundamental power $I(\omega)$ was expressed in In-In plot for linear line fitting. Value of fitting line slope was close to 2 (m = 1.96) confirming the validity of SHG measurement (see figure 3.10f). Second order NLO susceptibilities were obtained from the data fitting of the s-in/p-out and p-in/p-out SHG measurements of as-grown ZnONR and the fitting values are given in table 3.3 :

Growth time (hr)	**ave. nanorod diameter $\bar{d}$ (nm)**	**ave. nanorod length $\bar{\ell}$ (nm)**	**Aspect ratio $\wp$**	$\chi^{(2)}_{zzz}$ **(pm/V)**	$\chi^{(2)}_{zxx}$ **(pm/V)**	$\left\|\frac{\chi^{(2)}_{zxx}}{\chi^{(2)}_{zzz}}\right\|$
0.25	**10**	**57**	**5.7**	**-15.6**	**0.28**	**0.018**
0.75	**20**	**150**	**7.5**	**-25.6**	**0.76**	**0.03**
2.5	**31**	**245**	**7.9**	**-31.4**	**1.56**	**0.082**
5	**55**	**511**	**9.2**	**-28.8**	**2.88**	**0.10**
7.5	**62**	**667**	**10.8**	**-36**	**5.76**	**0.16**

Table 3.3 Fitting values of second order NLO susceptibilities of ZnONR grown from 0.25 hr to 7.5 hrs

According to data fitting of $\chi^{(2)}$ in table 3.3, geometry of NR determines the relative magnitude of the $\chi^{(2)}$ components. The higher the aspect ratio, the bigger the ratio of the 2 non-zero $\chi^{(2)}$ components $\left|\frac{\chi^{(2)}_{zxx}}{\chi^{(2)}_{zzz}}\right|$. The correlation between the aspect ratio and $\left|\frac{\chi^{(2)}_{zxx}}{\chi^{(2)}_{zzz}}\right|$ of NR has been previously reported[11] but not well understood. We would discuss its possible cause in the fore-coming sections.

3.2.4 High SHG response of as-grown ZnONR

Second order NLO susceptibilities of ZnO thin films (with thicknesses ranging from 50 nm to 1000 nm) which were fabricated by different techniques, were studied by SHG in the past few years by different research groups[33-43]. Apart from Zhang *et al.*[43], all reported that the most significant second order NLO susceptibility ($\chi^{(2)}_{zzz}$) has its magnitude ranging from 2 pm/V to 20 pm/V and the ratio of the two NLO susceptibilities $\left|\frac{\chi^{(2)}_{zxx}}{\chi^{(2)}_{zzz}}\right|$ ranging from 0.1 to 0.35, depending on the thickness, the crystallinity and the fabrication condition of the ZnO thin films. Zhang *et al*. found that $\chi^{(2)}_{zzz}$ and $\chi^{(2)}_{zxx}$ could be as high as 160 pm/V and 30 pm/V respectively, for sputtered ZnO thin films. Saykally *et al*. measured the second and third order NLO susceptibilities of single ZnO nanorod : they obtained $\chi^{(2)}_{zzz}$ around 6 pm/V, with the $\left|\frac{\chi^{(2)}_{zxx}}{\chi^{(2)}_{zzz}}\right|$ ratio between 0.25 and 0.5, depending on nanorod dimension.

According to SHG results of as-grown ZnONR in table 3.3, $\chi^{(2)}_{zzz}$ and $\chi^{(2)}_{zxx}$ range from -15.6 to -36 pm/V and 0.28 to 5.76 pm/V, with increasing aspect ratio $\wp$ of NR. The magnitude of $\chi^{(2)}$ is comparable to that of other ZnO nanostructures mentioned in the above paragraph. Although most of the researchers observe the SHG enhancement of nanostructures, no direct evidence to indicate the origin of such SHG enhancement. Contributions to SHG enhancement of nanostructure are not easily to be traced experimentally because nano-grain size and geometry are usually tremendously dispersed and random in orientation. However, with the uniform and order ZnONR that we fabricated for SHG studies, origin of such nanograin SHG enhancement can be investigated more deeply and it will be elaborated more in the next section.

Some researchers[11] believe that high SHG response of nano-scale ZnO is originated from surface NLO contribution $\chi^{(2)}_{\mathrm{suf}}$ due to multiple folds of surface. However, according to the SHG measurement of ZnONR in both configurations (s-in/p-out & p-in/p-out), Signal level is zero at zero angle of incidence which contradicts completely to the hypothesis of NR surface contribution according to the symmetry analysis of non-zero components of $\chi^{(2)}_{\mathrm{suf}}$. So, we exclude the suggestion that SHG enhancement from $\chi^{(2)}_{\mathrm{suf}}$ originated from dielectric discontinuation at surface boundary of NR.

In addition, as pointed out by Levine, Miller and Nordland in the late 60's, for polar crystals like ZnO, the two NLO coefficients $\chi^{(2)}_{\mathrm{zzz}}$ and $\chi^{(2)}_{\mathrm{zxx}}$ possess opposite signs : this was confirmed by Buinitskaya *et al*[44]., Wang *et al*.[33], Zhang *et al*. and Neumann *et al*.[35]. On the contrary, Cao *et al*.[36] and Liu *et al*.[37] found that $\chi^{(2)}_{\mathrm{zzz}}$ and $\chi^{(2)}_{\mathrm{zxx}}$ have the same sign. They have opposite signs in our ZnONR samples (Table 3.3) : this indicates simply that our NR samples crystallized in Wurtzite structure during the growth period.

3.2.5 Different SHG contributions from as-grown ZnONR

From the above SHG data fitting presented in table 3.3, $\chi^{(2)}$ appears to be greatly enhanced in ZnONR. As we should point out an important point that unlike ZnO bulk single crystal, volume ratio υ ($N\left(\frac{\overline{d}}{2}\right)^2\pi$) of ZnONR is lower than 1 (υ = 1 for bulk perfect crystal) where N is the number density (μm^{-2}) of NR, SHG contribution from NR structure would be weaker than that from bulk single crystal by a factor of υ. For instance, volume ratio υ of as-grown ZnONR of 5 hrs growth is : $\upsilon = N\left(\frac{\bar{d}}{2}\right)^2 \pi = 0.39$. The SHG contribution from second order NLO susceptibilities of nanoscale ZnO single crystal rods becomes :

$$\chi^{(2)}_{zxx,NR} = \upsilon\chi^{(2)}_{zxx} = 0.39x4 = 1.56pm/V \tag{3.4}$$

$$\chi^{(2)}_{zzz,NR} = \upsilon\chi^{(2)}_{zzz} = 0.39x-14 = -5.46pm/V \tag{3.5}$$

If the SHG response of ZnONR is only originated from bulk second order NLO susceptibilities of the NRs, SHG response of s-in/p-out and p-in/p-out configurations should be close to the solid line fittings of figure 3.11. However, as shown in the figure, for the case of 5-hrs as-grown ZnONR, experimental and SHG data fitting are having big disagreement which exists for ZnONR with different aspect ratio and different growth time. Experimental SHG response is higher than that from bulk SHG contribution of ZnONR. It shows clearly that SHG response from ZnONR is not only due to bulk second order NLO susceptibilities of ZnO single crystal, but is also attributed to other nonlinear optical process. In the following paragraph, we would discuss another mechanism in NR contributing to high SHG response of the ZnONR.

In addition to the bulk SHG response of ZnONR due to the nature of polar crystal of ZnO, we suggest that there is a EFISH-type SHG contribution from NR. Due to the geometrical feature of NR (needle-shape) and the potential gradient in the quartz|ZnONR|air system, photo-induced charge transfer and they accumulate at both end of NR respectively as shown in figure 3.12a. In figure 3.12b, energy level of the ZnONR system is shown and interfacial charge transfer due to energy level difference is shown as well.

5-hrs as-grown ZnONR $\overline{\ell} = 0.511\mu\text{m}, \overline{\text{d}} = 0.055\mu\text{m}$, N=200$\mu$m^{-2}	$\chi^{(2)}_{\text{zxx,NR}} = 1.56\text{pm/V}, \chi^{(2)}_{\text{zzz,NR}} = -5.46\text{pm/V}$ SHG(a.u.)
s-in/p-out	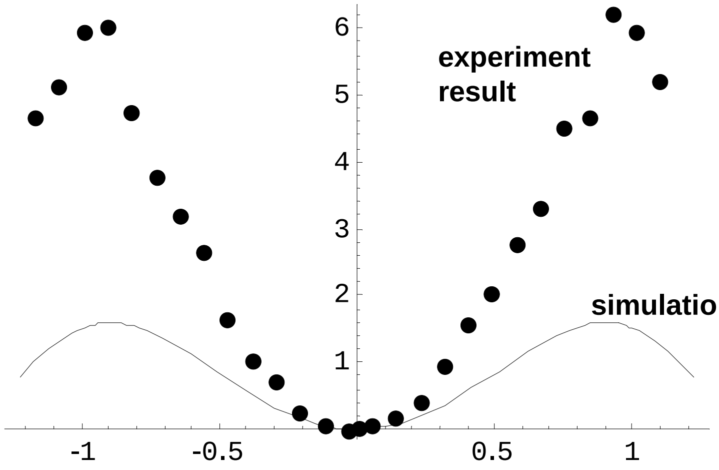
p-in/p-out	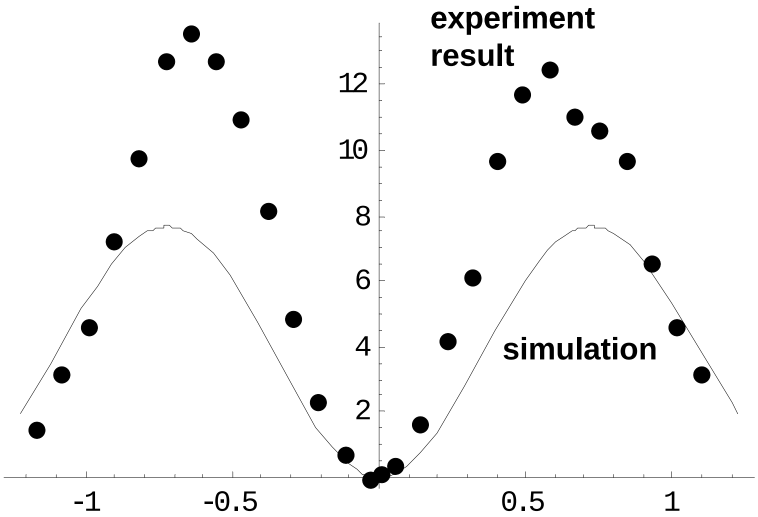
	incidentθ_{in} (rad.)

Figure 3.11 Experiment result of SHG response from 5hrs as-grown ZnONR and the simulation of SHG response due to bulk second order susceptibility contribution

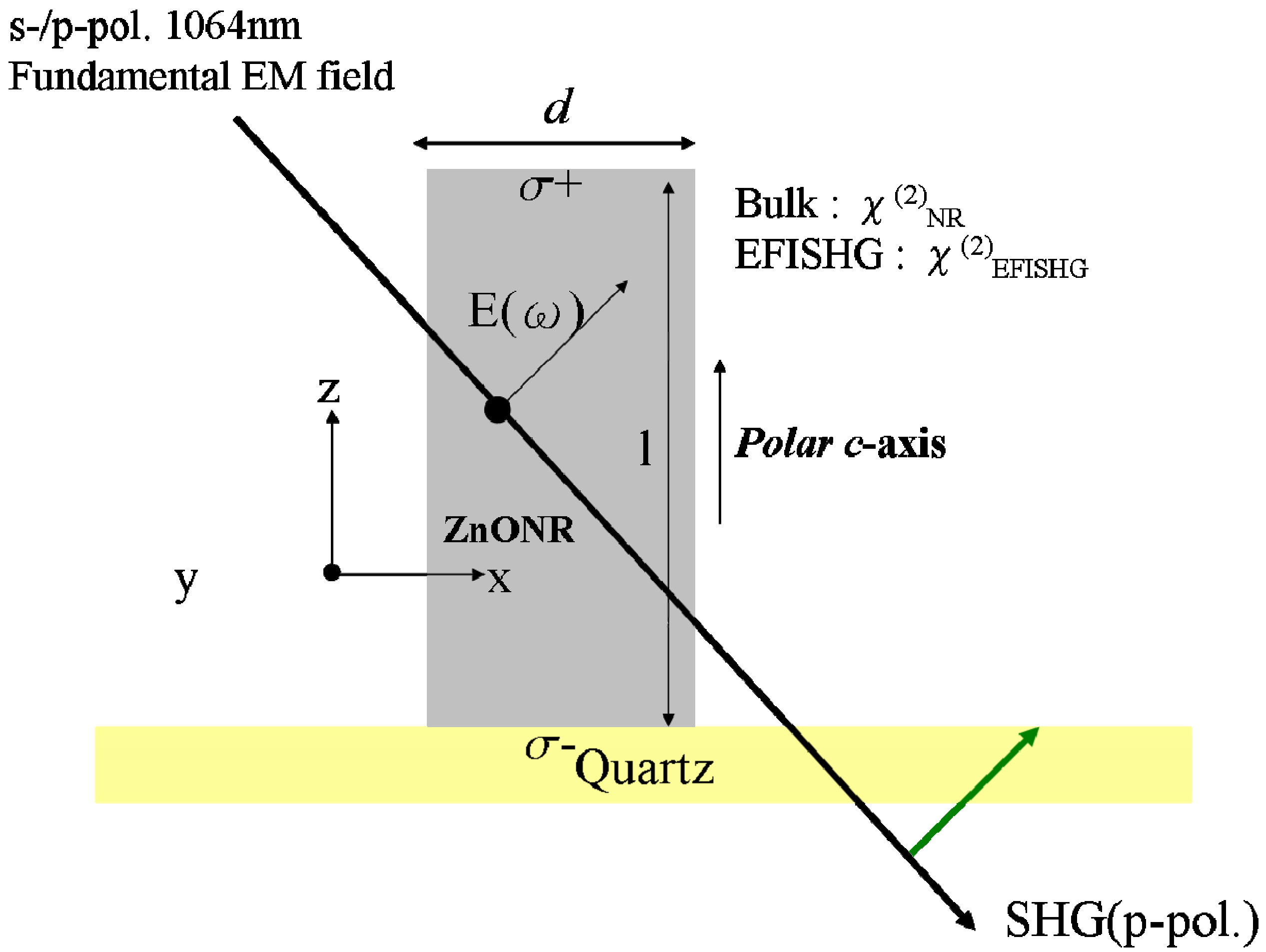

Figure 3.12a Bulk and EFISHG contributions to SHG response of ZnONR

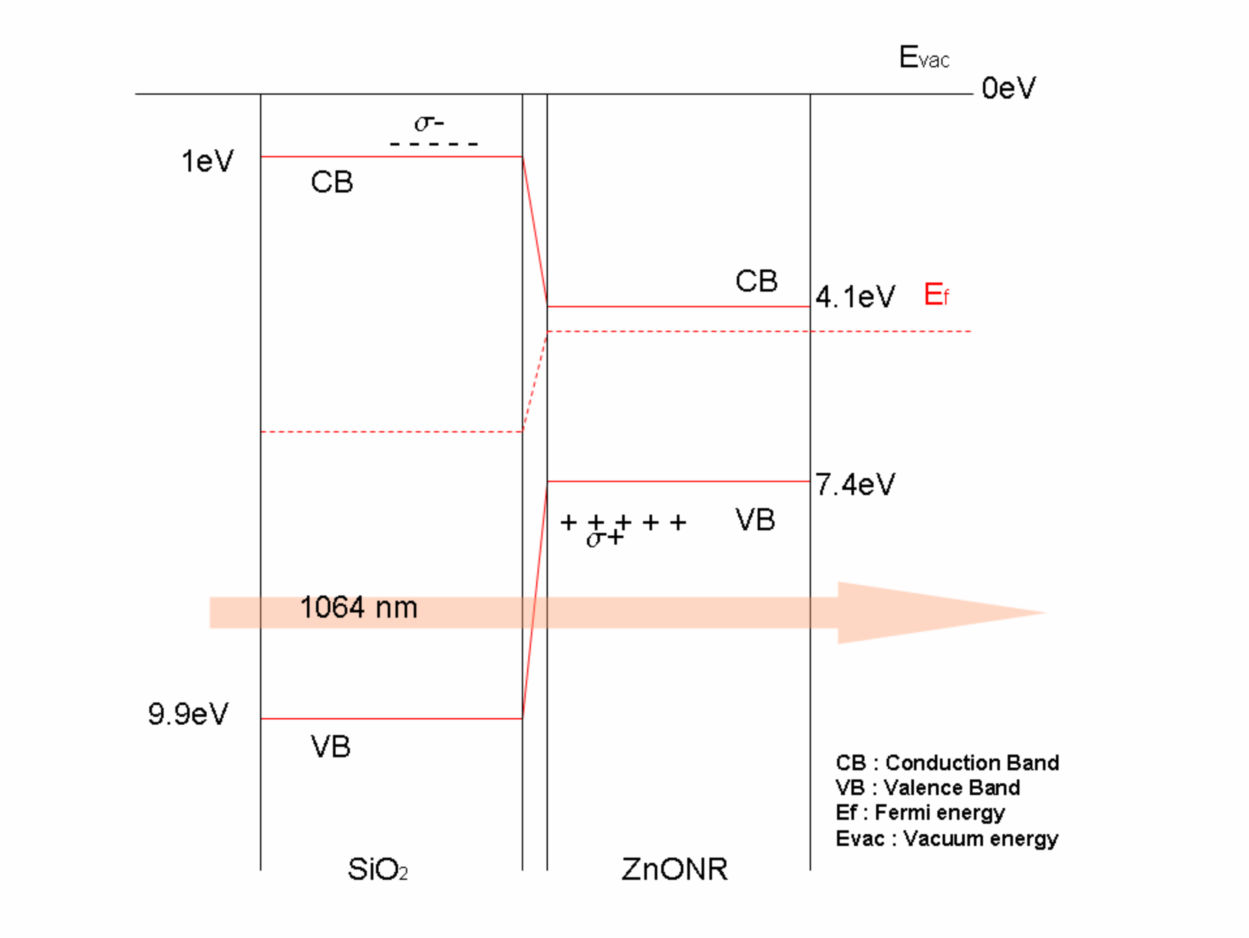

Figure 3.12b Energy level diagram of ZnONR (on quartz) and the photo-induced interfacial charge transfer upon illumination

Charge accumulation at both ends of ZnONR is brought by the photo-induced charge transfer. Static electric field E_σ is established across NRs which gives EFISHG effect :

$$P_{2\omega,\mathrm{EFISHG}} \sim \chi^{(3)}_{\mathrm{EFISHG}} E_\sigma E_\omega^2 \tag{3.6}$$

For EFISHG-type second order NLO susceptibilities, 6mm point group[45] is valid for the assignment of non-vanishing components of $\chi^{(3)}_{\mathrm{EFISHG}}$. For 6mm point group symmetry, there are only 3 non-zero components : $\chi^{(3)}_{zxx,\mathrm{EFISHG}} = \chi^{(3)}_{xzx,\mathrm{EFISHG}}, \chi^{(3)}_{zzz,\mathrm{EFISHG}}$. In general, the effective second order NLO susceptibility $\chi_{\text{eff}}^{(2)}$ in s-in/p-out and p-in/p-out cases can be represented as :

1) s-in/p-out :

$$\chi_{\text{eff}}^{(2)} = \chi_{\text{zxx,NR}}^{(2)} + \nu\chi_{\text{zxx,EFISHG}}^{(3)} E_{\sigma} \tag{3.7}$$

2) p-in/p-out :

$$\chi_{\text{zzz}}^{(2)} = \chi_{\text{zzz,NR}}^{(2)} + \nu\chi_{\text{zzz,EFISHG}}^{(3)} E_{\sigma} \tag{3.8}$$

With bulk SHG contribution being fixed from SHG measurement of ZnONR at s-in/p-out and p-in/p-out, EFISHG-type SHG contribution can be obtained and the fitting is as shown in figure 3.13 :

5-hrs as-grown ZnONR $\bar{\ell} = 0.55\mu\text{m}, \bar{d} = 0.055\mu\text{m}$	SHG(a.u.)
s-in/p-out	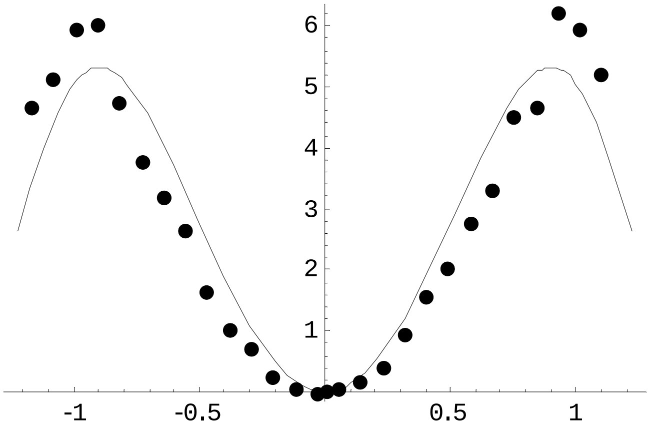

p-in/p-out	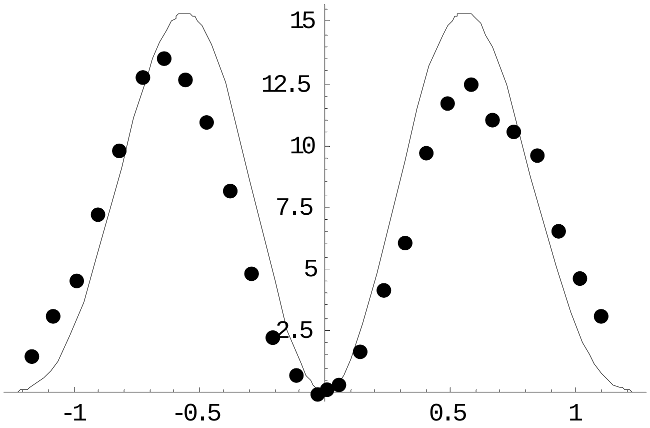
	incidentθ_{in} (rad.)

Figure 3.13 SHG response of 5hrs as-grown ZnONR with data fitting taking into account the bulk and the EFISHG-type second order NLO susceptibilities of NRs

From the theoretical data fitting of s-in/p-out and p-in/p-out SHG measurements of 5-hrs as-grown ZnONR, we obtain $\chi^{(3)}_{zxx,EFISHG}E_{\sigma}$ = 1.66 pm/V and $\chi^{(3)}_{zzz,EFISHG}E_{\sigma}$ = -28.3 pm/V. We could be able to figure out charge accumulation σ at NR's two ends if intrinsic third order NLO susceptibilities $\chi^{(3)}_{zxx,EFISHG}, \chi^{(3)}_{zzz,EFISHG}$ are known. Big difference between $\chi^{(3)}_{zxx,EFISHG}E_{\sigma}$ (1.66 pm/V) and $\chi^{(3)}_{zzz,EFISHG}E_{\sigma}$ (-28.3 pm/V) indicate that quantity of the accumulated charge σ, from where electric field E_{σ} is created ($E_{\sigma} \sim \sigma$), depends strongly on the polarization of fundamental EM field. Charge conductivity of ZnONR is strongly enhanced along the longitudinal axis (z-axis) of NR. This has already been justified from the strong field emission (FE) properties of ZnONR[46-49]. For instance, the turn-on voltage of ZnO nanowire can be as low as 6 Vμm^{-1} with current density of 0.1 μAcm^{-2}. Charge conduction and accumulation are greatly enhanced in ZnONR. When applying electric field along ZnONR, current density along NR can be greatly enhanced.

For s-polarized EM field excitation (SHG in s-in/p-out case), charge conduction along longitudinal z-axis of ZnONR is not greatly enhanced because EM field is polarized at x-axis. But for p-polarized EM field (SHG in p-in/p-out case), charge conduction and accumulation can be highly enhanced with p-polarized EM field (non-zero z-component) which facilitates the charge transport at ZnONR surface and the charge accumulation at NR's ends.

As reported in previous paragraph, the magnitude of $\chi^{(3)}_{zxx,EFISHG}E_{\sigma}$ and $\chi^{(3)}_{zzz,EFISHG}E_{\sigma}$ of the 5-hrs as-grown ZnONR are close to 1.66 pm/V and 28.3 pm/V respectively. From p-in/p-out SHG measurement, we estimate local electric field strength E_{σ} established across NR due to photo-induced charge accumulation using $\chi^{(3)}_{zzzz}$ value obtained by Larciprete M. C. *et al.*[41] according to equation 3.8 ($\chi^{(3)}_{zzzz} \sim 2x10^{-18}\frac{m^2}{V^2}$ measured at $\lambda = 1904$ nm) :

$$\left|E_{\sigma}\right| \bullet 0.4 \bullet 2 \bullet 10^{-18}\frac{m^2}{V^2} \sim 20 \bullet 10^{-12}\frac{m}{V} \sim 20V\mu m^{-1}$$

Local electric field strength E_{σ} across NR can be as high as 20 Vμm^{-1} (2x10^{7} Vm^{-1}). With the estimated electric field strength E_{σ}, we could further calculate the charge density σ at both NR ends.

Considering the situation as shown below and we apply Gauss's law : $E = \frac{\sigma(\text{bulk})}{\tilde{\varepsilon}}$, where $\tilde{\varepsilon}$ is the effective dielectric constant of the ZnONR sample deduced from effective-medium theory[50, 51] : $\tilde{\varepsilon} \sim \varepsilon_{air} + \nu\left[\frac{3\varepsilon_{ZnO}}{2\varepsilon_{air} + \varepsilon_{ZnO}}\right]\left(\varepsilon_{ZnO} - \varepsilon_{air}\right)$. For 5-hr growth ZnONR as an example :

$$\sigma = \frac{E\tilde{\varepsilon}}{\nu} = \frac{2 \bullet 10^{7} \bullet 2.5 \bullet 10^{-11}}{0.39} = 1.3 \bullet 10^{-3}Cm^{-2} = 8 \bullet 10^{11}\frac{e}{cm^2}$$

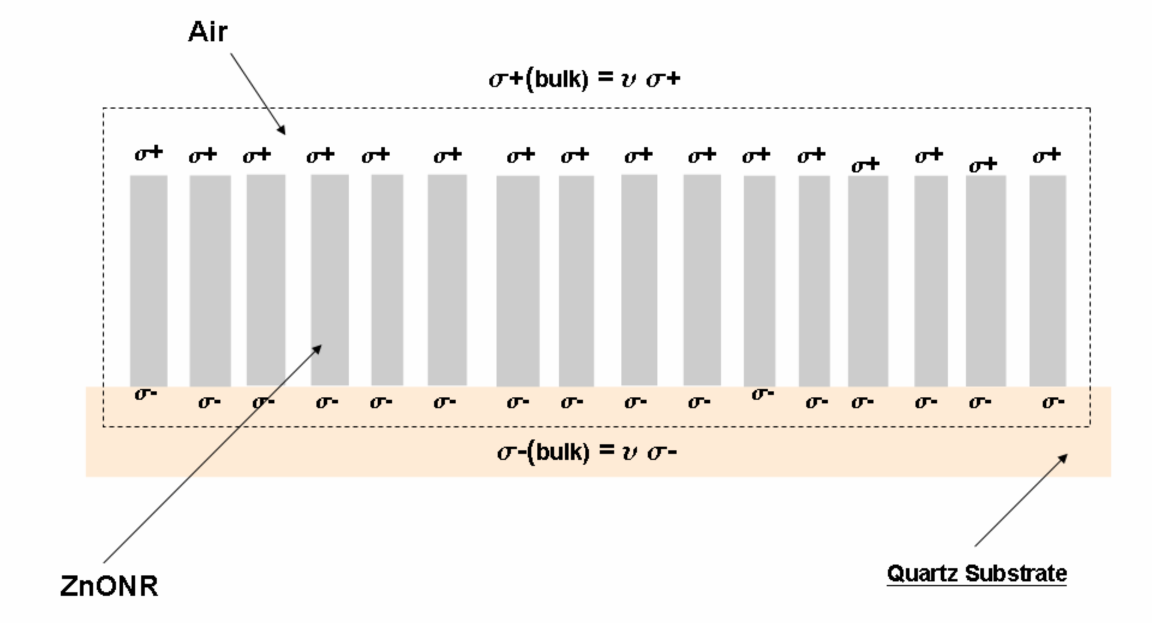

From the above calculation, we estimate that surface charge density σ during SHG measurement could attain 10^{12} ecm^{-2} which is high enough to enhance the SHG effect measured.

We have to stress that one limitation of this estimation is attributed to an accurate determination of the third order NLO susceptibility of ZnO. However, the emergence of such considerable potential difference across NR could be further justified by any surface potential sensitive technique like Kelvin Probe. We are working on surface voltage measurement to quantify the above electric field effect on ZnoNR SHG. More detailed description of the mechanism of Kelvin Probe will be given in the chapter 4.

3.2.6 Evidence of EFISHG contribution to SHG response of ZnONR

For verifying contribution EFISHG-type SHG to high SHG response of ZnONR, we investigated SHG variation of 5-hrs as-grown ZnONR sample with respect to the change of dielectric property of the environment of ZnONR. With the change of dielectric constant of environment, the capability of photo-induced charge accumulation σ at NR's ends change correspondingly. Simply speaking, charge accumulation σ is proportional linearly to dielectric property of environment :

$$\sigma = k\varepsilon \tag{3.9}$$

where k is the proportionality constant and ε is dielectric permittivity of the environment. The more the charge accumulation, the higher the EFISHG-type SHG contribution. To verify the validity of EFISHG-type SHG in ZnONR, we introduced organic solvents of different dielectric constants and monitored variation SHG response. Introducing different organic solvent would not affect the bulk SHG contribution from ZnONR but the charge accumulation capability at the NR's ends as mentioned. Experimental setup for this EFISHG-type SHG contribution is shown in figure 3.14 :

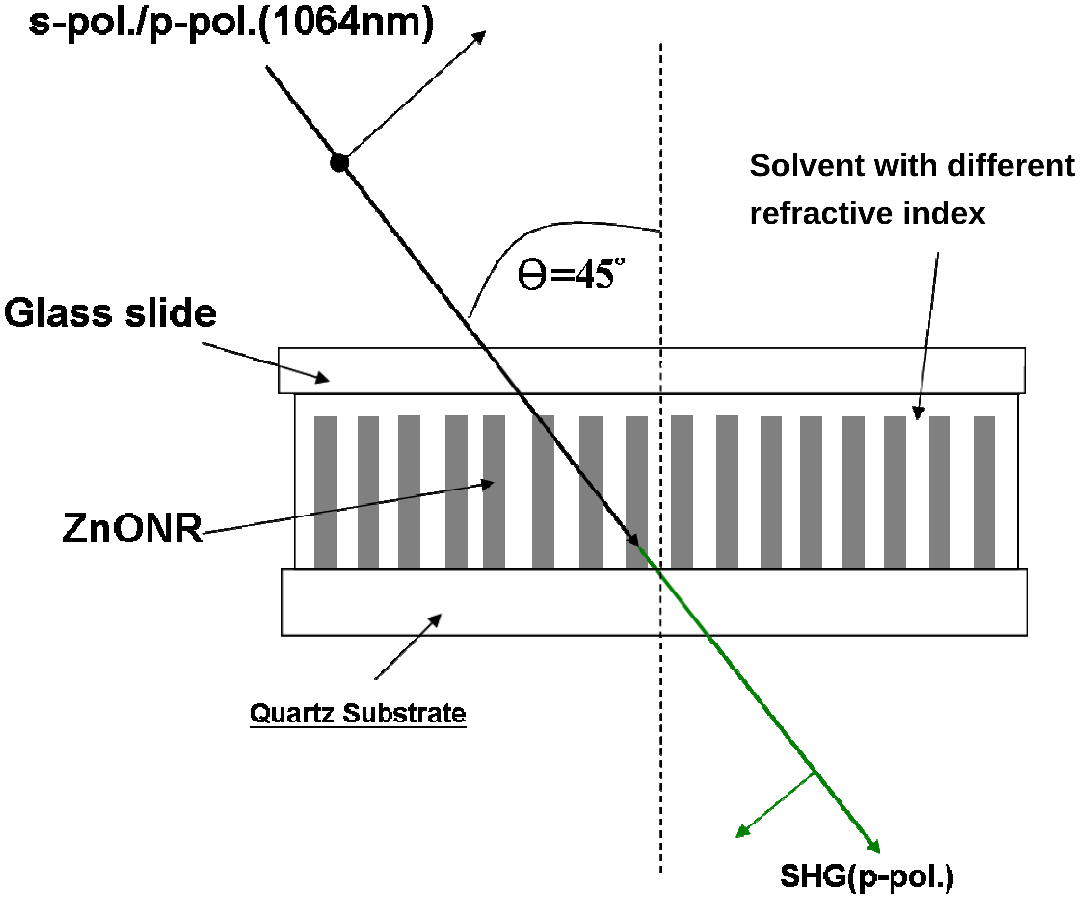

Figure 3.14 Experimental setup for the study of EFISHG-type SHG contribution using different organic solvents

5-hrs as-grown ZnONR samples (length ~ 500 nm, rod density ~ 200 μm^{-2}) were placed horizontally and organic solvents of different dielectric constant ϵ were introduced on samples. Then samples were covered with transparent glass slide for preventing the evaporation of the volatile solvents. Dielectric permittivities of different organic solvents employed are listed in table 3.4.

Organic solvent	Dielectric permittivity ϵ
air	1
Water (H_2O)	1.77
Acetone	1.87
DMF	2.16
Paraffin oil	2.19
Chlorobenzene	2.31
Carbon disulfide (CS_2)	2.66

Table 3.4 Dielectric permittivity of different organic solvent

Fundamental EM fields of s-pol. and p-pol. were incident onto ZnONR at the incident angle of 45° and p-pol. SHG signal was measured for samples immersed in different organic solvents. The SHG signals (normalized to SHG signal of NR in the air) of s-in/p-out and p-in/p-out are shown below in figure 3.15 :

s-in/p-out	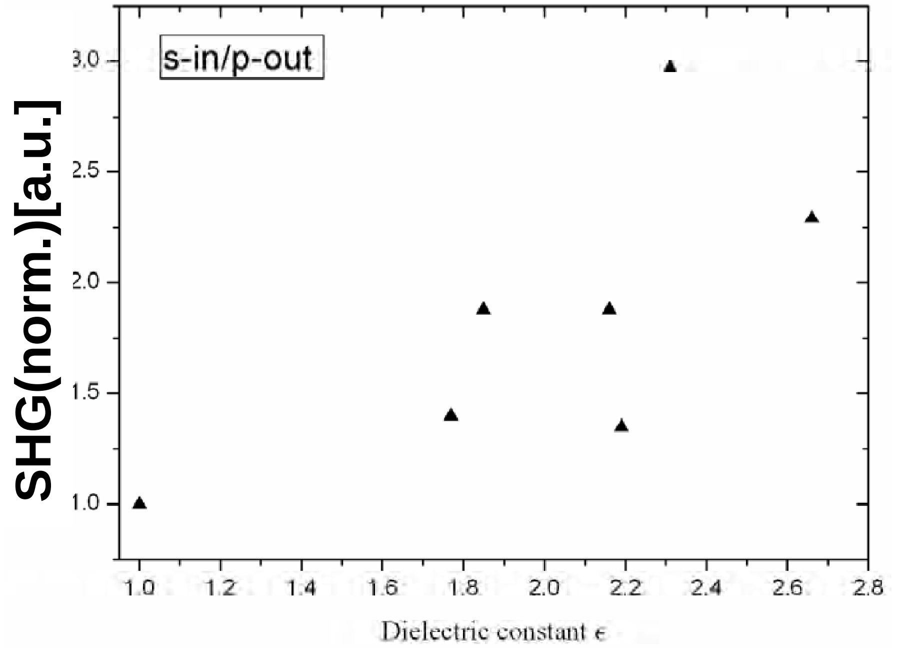

p-in/p-out	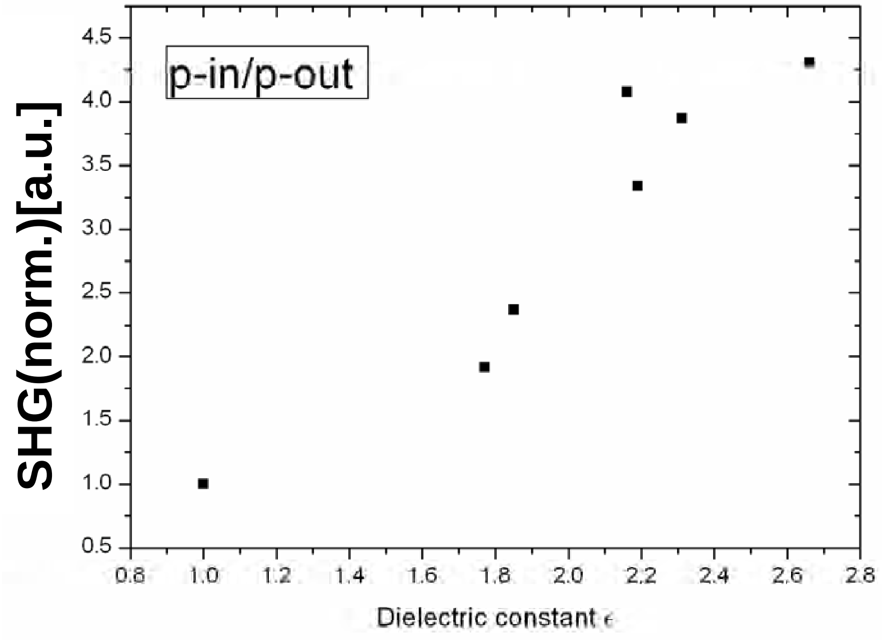

Figure 3.15 SHG response of ZnONR samples immersed at different organic solvents of different dielectric constant

Referring to figure 3.15. For both s-in/p-out and p-in/p-out cases, SHG signal at 45° angle of incidence show the trend of increase with the increase of dielectric permittivity ϵ of environment where NRs were immersed in. In addition, we performed a control experiment on the ZnO <0001> single crystal. Change of dielectric parameters of environment of ZnO single crystal, on the contrary, did not alternate the SHG signal from ZnO single crystal. These dielectric constant matching experiments give complimentary support (Referring back to section 3.2.5) that high SHG response from ZnONR does not originate from surface SHG $\chi^{(2)}_{\text{surface}}$ (which was extensively studied by Philippe M. Guyot-Sionnest *et al.*[52]). If high SHG response of ZnONR sample comes from the NR surface, the dielectric constant matching condition of ZnONR to the surrounding media (host) would diminish the high SHG response. However, according to our dielectric matching SHG experiment results (figure 3.15), SHG response increases with increasing dielectric constant of host media.

This results conclude that the SHG enhancement of ZnONR is originated from the EFISHG-type SHG contribution due to high charge conductivity along NR surface and high capability of charge accumulation of at NR's ends.

3.3 Second order NLO response of annealed ZnONR

As demonstrated in the previous section that SHG response of ZnONR relates closely to charge conductivity at NR surface and the capability of charge accumulation at NR's ends. We would like to study SHG response of ZnONR annealed differently. Indentical as-grown ZnONR samples (rod density ~ 200 μm^{-2}, $\overline{\ell} \sim 700\text{nm}, \overline{\text{d}} \sim 55\text{nm}$) were annealed in a tube furnace at different temperatures (200°C, 400°C and 600°C) in reducing agent : forming gas (90% N_2/10% H_2) or at 600°C in oxidizing agents : Air (Relative humidity ~ 55-60%) and oxygen. The annealing duration was about 30 minutes. The annealing gas flow rate was 0.1 lm^{-1} and the pressure was ~ 1 Torr.

Crystalline properties of as-grown ZnONR, prepared at the hydrothermal process described in above, are different to that of ZnO single crystal when the crystal defects both in bulk and on the NR surface. Various studies including photoluminescence PL, X-ray diffraction XRD, positron annihilation spectroscopy (PAS) and Raman spectroscopy reveal that different kinds of defects decrease in number when the samples are annealed under different conditions. Charge conductivity of NR is greatly affected by defects' population and they have been studied to field emission (FE) of ZnONR. Researchers[53, 54] showed that with improving ZnONR crystallinity and decreasing defects' population by gas annealing, current density (mAcm^{-2}) increase prominently. It reflects that NR conductivity is boosted up upon annealing. With lesser defects on NR surface, charge transfer can be highly enhanced and so to the FE capability. They showed that with annealing, current density of NR could be higher boosted up under the same applied voltage which, in the other words, means that charge can be transferred and accumulated easier.

Figure 3.16 below indicates SHG response from as-grown and different annealed ZnONR samples and their SHG data fitting.

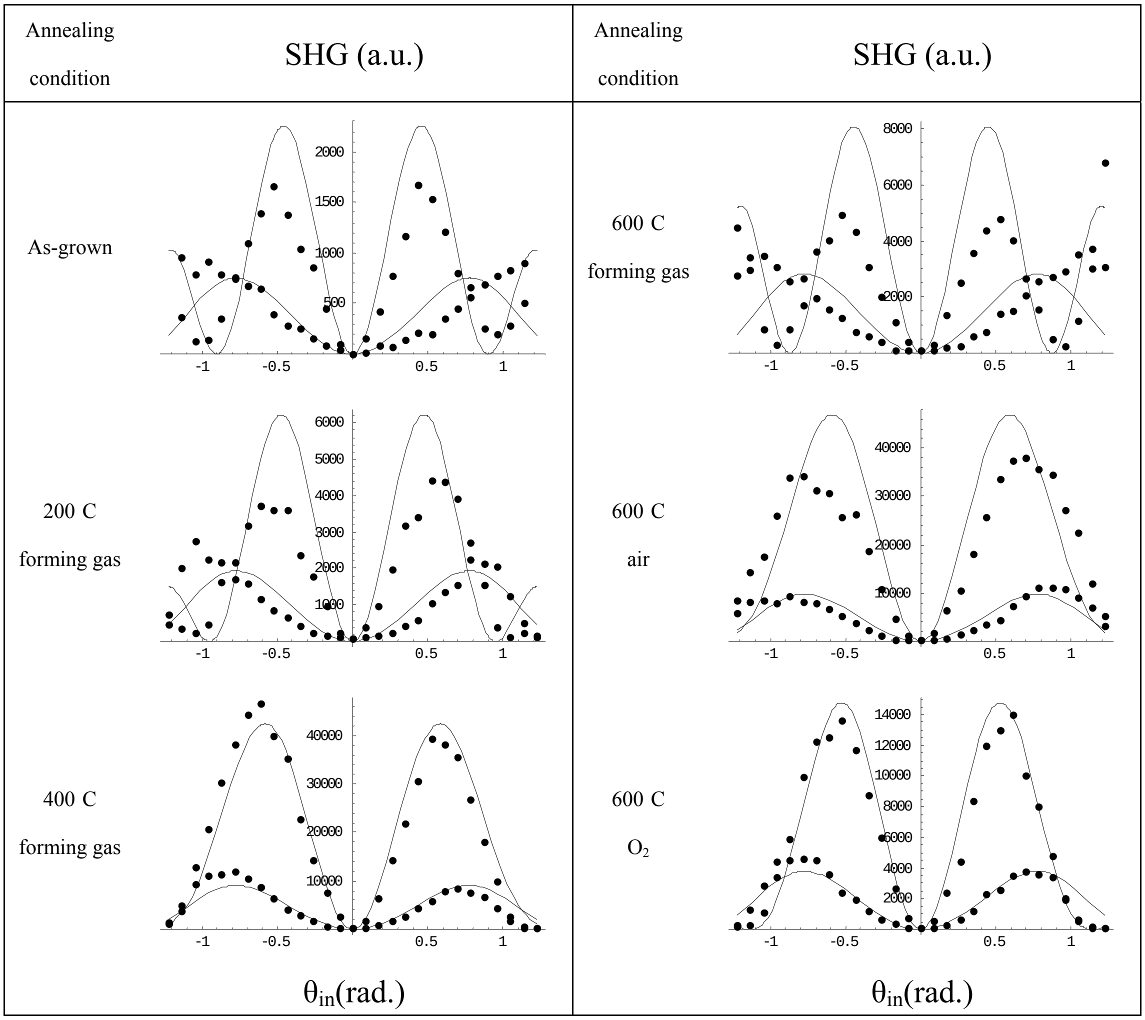

Figure 3.16 Second Harmonic Generation (SHG) of ZnONR annealed at different condition and their data fitting (the data set with higher magnitude is from p-p SHG measurement where another is from s-p measurement)

According to the data fitting, SHG response was enhanced in all cases of annealed ZnONR samples. The value of the $\chi^{(2)}_{zxx}$ and $\chi^{(2)}_{zzz}$ compared with those of as-grown ZnONR sample are presented in table 3.5 :

Annealing condition	$\chi^{(2)}_{zxx}$ (norm.)	$\chi^{(2)}_{zzz}$ (norm.)
As-grown	1	1
200°C forming gas	1.28	1.16
400°C forming gas	2.76	1.47
600°C forming gas	1.54	1.63
600°C air	2.87	1.47
600°C oxygen	1.79	1.25

Table 3.5 Second order NLO susceptibilities $\chi^{(2)}$ of annealed ZnONR samples with the reference to as-grown ZnONR sample

Referring to the above table, second order NLO susceptibilities from ZnONR increases with the annealing of ZnONR sample under all conditions. It shows preliminarily that the decrease in surface/bulk defects populations, which increases NR conductivity, facilitates charge generation and accumulation (higher EFISHG-type SHG contribution). However, the details of the effects of different defects to capability of charge transfer and accumulation have to be further studied.

3.4 Chapter summary

We have discussed second order NLO susceptibility of polar inorganic crystal zinc oxide ZnO of crystal size from mm to nm. ZnO single crystal of orientation <0001> was studied with Second Harmonic Generation (SHG) and its second order NLO response obtained is consistent to the previous results of standard theoretical calculation and experimental results. However, as the size of ZnO crystal diminishes to nano-scale (Nano-Rod NR), its second order NLO response alters tremendously.

We compared the relative sign and the magnitude of non-vanishing second order

NLO susceptibilities between mm-scale single crystal and nm-scale single crystal (NR). We find that effective second order NLO response of nano-scale single crystal (NR) is far higher than that of mm-scale single crystal. In addition, such increase in second order NLO response depends critically on the geometry of the nm-scale single crystal : big enhancement along longitudinal axis (polar c-axis) of NR. We propose that effective charge conductivity along NR's surface facilitates charge separation at NR's ends which creates a relatively large local electric field across NR. Large second order NLO response is due to significant contribution from electric field induced second harmonic generation (EFISHG) effect.

We did an estimation of the electric field strength established across NRs for 5-hrs as-grown ZnONR. Its magnitude could be as high as around 20 $V\mu m^{-1}$ as calculated from the experimental value of third order NLO susceptibility obtained. The charge density at NRs' ends due to photoexcitation is estimated to be around 10^4 Ccm^{-2}. Such existence of local electric field strength due to charge accumulation at NRs' ends is justified further in the SHG experiment of as-grown ZnONR immersed in different dielectric environment. Higher SHG response for ZnONR at environment of higher dielectric constant indicates that the charge accumulation at NRs' ends is improved giving bigger EFISHG contribution to the measured SHG signal.

At last, we presented SHG measurement of ZnONR annealed at different gas like air, N_2 and O_2. Researchers generally accept that gas annealing minimizes the number of different defects at the surface and in the bulk respectively and thus, it would strengthen the charge conductivity at surface and to improve charge accumulation at NRs' ends. SHG results of annealed ZnONR samples show that SHG response of all annealed ZnONR samples increase with respect to as-grown sample. However, relation between SHG enhancement and the annealing condition is still not fully understood.

Chapter references

1. H. Cao, J. Y. Xu, D. Z. Zhang, S. H. Chang, S. T. Ho, E. W. Seelig, X. Liu, and R. P. H. Chang, "Spatial confinement of laser light in active random media," Physical Review Letters **84**(24), 5584-5587 (2000).
2. E. M. Wong and P. C. Searson, "ZnO quantum particle thin films fabricated by electrophoretic deposition," Applied Physics Letters **74**(20), 2939-2941 (1999).
3. M. H. Huang, Y. Y. Wu, H. Feick, N. Tran, E. Weber, and P. D. Yang, "Catalytic growth of zinc oxide nanowires by vapor transport," Advanced Materials **13**(2), 113-116 (2001).
4. M. H. Huang, S. Mao, H. Feick, H. Q. Yan, Y. Y. Wu, H. Kind, E. Weber, R. Russo, and P. D. Yang, "Room-temperature ultraviolet nanowire nanolasers," Science **292**(5523), 1897-1899 (2001).
5. W. U. Huynh, J. J. Dittmer, and A. P. Alivisatos, "Hybrid nanorod-polymer solar cells," Science **295**(5564), 2425-2427 (2002).
6. J. B. Baxter and E. S. Aydil, "Nanowire-based dye-sensitized solar cells," Applied Physics Letters **86**(5) 053114 (2005).
7. M. Law, L. E. Greene, J. C. Johnson, R. Saykally, and P. D. Yang, "Nanowire dye-sensitized solar cells," Nature Materials **4**(6), 455-459 (2005).
8. S. C. Lyu, Y. Zhang, H. Ruh, H. J. Lee, H. W. Shim, E. K. Suh, and C. J. Lee, "Low temperature growth and photoluminescence of well-aligned zinc oxide nanowires," Chemical Physics Letters **363**(1-2), 134-138 (2002).
9. Y. Cui, Q. Q. Wei, H. K. Park, and C. M. Lieber, "Nanowire nanosensors for highly sensitive and selective detection of biological and chemical species," Science **293**(5533), 1289-1292 (2001).
10. C. Dekker, "Carbon nanotubes as molecular quantum wires," Physics Today **52**(5), 22-28 (1999).
11. Y. Lu and J. Zhong, *Zinc Oxide-Based Nanostructures*, Semiconductor Nanostructures for Optoelectronic Applications (ARTECH HOUSE, INC., 2004).
12. K. Maeda, M. Sato, I. Niikura, and T. Fukuda, "Growth of 2 inch ZnO bulk single crystal by the hydrothermal method," Semiconductor Science And Technology **20**(4), S49-S54 (2005).

13. B. F. Levine, "Electrodynamical Bond-Charge Calculation Of Nonlinear Optical Susceptibilities," Physical Review Letters **22**(15), 787 (1969).

14. C. Cojan, G. P. Agrawal, and C. Flytzanis, "Optical-Properties Of One-Dimensional Semiconductors And Conjugated Polymers," Physical Review B **15**(2), 909-925 (1977).
15. R. C. Miller, "optical second harmonic generation in piezoelectric crystals," Applied Physics Letters **5**(1) 17-19 (1964).
16. R. C. Miller and W. A. Nordland, "Absolute Signs Of Second-Harmonic Generation Coefficients Of Piezoelectric Crystals," Physical Review B **2**(12), 4896-& (1970).

17. Y. R. Shen, *The Principles of Nonlinear Optics* (John Wiley & Sons, Inc., USA, 1984).
18. B. F. Levine, "Bond-Charge Calculation Of Nonlinear Optical Susceptibilities For Various Crystal-Structures," Physical Review B **7**(6), 2600-2626 (1973).
19. J. C. Johnson, H. Q. Yan, R. D. Schaller, P. B. Petersen, P. D. Yang, and R. J. Saykally, "Near-field imaging of nonlinear optical mixing in single zinc oxide nanowires," Nano Letters **2**(4), 279-283 (2002).

20. L. E. Greene, M. Law, D. H. Tan, M. Montano, J. Goldberger, G. Somorjai, and P. D. Yang, "General route to vertical ZnO nanowire arrays using textured ZnO seeds," nano letters **5**(7), 1231-1236 (2005).
21. D. Li, Y. H. Leung, A. B. Djurisic, Z. T. Liu, M. H. Xie, S. L. Shi, S. J. Xu, and W. K. Chan, "Different origins of visible luminescence in ZnO nanostructures fabricated by the chemical and evaporation methods," Applied Physics Letters **85**(9), 1601-1603 (2004).
22. Y. Harada and S. Hashimoto, "Enhancement of band-edge photoluminescence of bulk ZnO single crystals coated with alkali halide," Physical Review B **68**(4), 045421 (2003).
23. N. Y. Garces, L. Wang, L. Bai, N. C. Giles, L. E. Halliburton, and G. Cantwell, "Role of copper in the green luminescence from ZnO crystals," Applied Physics Letters **81**(4), 622-624 (2002).
24. S. A. Studenikin and M. Cocivera, "Time-resolved luminescence and photoconductivity of polycrystalline ZnO films," Journal Of Applied Physics **91**(8), 5060-5065 (2002).
25. N. Y. Garces, N. C. Giles, L. E. Halliburton, G. Cantwell, D. B. Eason, D. C. Reynolds, and D. C. Look, "Production of nitrogen acceptors in ZnO by thermal annealing," Applied Physics Letters **80**(8), 1334-1336 (2002).

26. B. X. Lin, Z. X. Fu, and Y. B. Jia, "Green luminescent center in undoped zinc oxide films deposited on silicon substrates," Applied Physics Letters **79**(7), 943-945 (2001).
27. N. Ohashi, T. Nakata, T. Sekiguchi, H. Hosono, M. Mizuguchi, T. Tsurumi, J. Tanaka, and H. Haneda, "Yellow emission from zinc oxide giving an electron spin resonance signal at g=1.96," Japanese Journal Of Applied Physics Part 2-Letters **38**(2A), L113-L115 (1999).
28. K. Vanheusden, C. H. Seager, W. L. Warren, D. R. Tallant, and J. A. Voigt, "Correlation between photoluminescence and oxygen vacancies in ZnO phosphors," Applied Physics Letters **68**(3), 403-405 (1996).
29. W. N. Herman and L. M. Hayden, "Maker Fringes Revisited - 2nd-Harmonic Generation From Birefringent Or Absorbing Materials," Journal Of The Optical Society Of America B-Optical Physics **12**(3), 416-427 (1995).
30. Kurtz, "A powder technique for the Evaluation of Nonlinear Optical Materials," Journal Of Applied Physics **39**(8), 3798 (1968).
31. D. A. Kleinman, "Nonlinear Optical Susceptibilities of Covalent Crystals," Physical Review B **2**(8), 3139 (1970).
32. D. A. Kleinman, "Nonlinear Dielectric Polarization in Optical Media," Physical Review **126**(6), 1977 (1962).

33. G. Wang, G. T. Kiehne, G. K. L. Wong, J. B. Ketterson, X. Liu, and R. P. H. Chang, "Large second harmonic response in ZnO thin films," Applied Physics Letters **80**(3), 401-403 (2002).
34. M. C. Larciprete, D. Passeri, F. Michelotti, S. Paoloni, C. Sibilia, M. Bertolotti, A. Belardini, F. Sarto, F. Somma, and S. Lo Mastro, "Second order nonlinear optical properties of zinc oxide films deposited by low temperature dual ion beam sputtering," Journal Of Applied Physics **97**(2), 023501 (2005).
35. U. Neumann, R. Grunwald, U. Griebner, G. Steinmeyer, and W. Seeber, "Second-harmonic efficiency of ZnO nanolayers," Applied Physics Letters **84**(2), 170-172 (2004).
36. H. Cao, J. Y. Wu, H. C. Ong, J. Y. Dai, and R. P. H. Chang, "Second harmonic generation in laser ablated zinc oxide thin films," Applied Physics Letters **73**(5), 572-574 (1998).
37. C. Y. Liu, B. P. Zhang, N. T. Binh, and Y. Segawa, "Second harmonic generation in ZnO thin films fabricated by metalorganic chemical vapor deposition," Optics Communications **237**(1-3), 65-70 (2004).

38. X. Q. Zhang, Z. K. Tang, M. Kawasaki, A. Ohtomo, and H. Koinuma, "Second harmonic generation in self-assembled ZnO microcrystallite thin films," Thin Solid Films **450**(2), 320-323 (2004).

39. G. Wang, G. K. L. Wong, and J. B. Ketterson, "Redetermination of second-order susceptibility of zinc oxide single crystals," Applied Optics **40**(30), 5436-5438 (2001).

40. A. Mitra and R. K. Thareja, "Dependence of second harmonic generation on size of nanocrystallites of ZnO," Modern Physics Letters B **15**(15), 515-521 (2001).

41. M. C. Larciprete, D. Haertle, A. Belardini, M. Bertolotti, F. Sarto, and P. Gunter, "Characterization of second and third order optical nonlinearities of ZnO sputtered films," Applied Physics B-Lasers And Optics **82**(3), 431-437 (2006).

42. U. Neumann, R. Grunwald, U. Griebner, G. Steinmeyer, M. Schmidbauer, and W. Seeber, "Second-harmonic performance of a-axis-oriented ZnO nanolayers on sapphire substrates," Applied Physics Letters **87**(17), 171108 (2005).

43. X. Q. Zhang, Z. K. Tang, M. Kawasaki, A. Ohtomo, and H. Koinuma, "Resonant exciton second-harmonic generation in self-assembled ZnO microcrystallite thin films," Journal Of Physics-Condensed Matter **15**(30), 5191-5196 (2003).

44. G. Buinitskaya, L. Kulyuk, V. Mirovitskii, E. Rusu, E. Mishina, and N. Sherstyuk, "ZnOsingle crystal and epitaxial thin film studied by second harmonic generation and photoluminescence," Superlattices And Microstructures **39**(1-4), 83-90 (2006).

45. S. V. Popov, Y. P. Svirko, and Z. N. I., *Susceptibility tensors for nonlinear optics*, Optics and Optoelectronicss Series (Institute of Physics Publishing, 2004).

46. H. Y. Yang, S. P. Lau, S. F. Yu, L. Huang, M. Tanemura, J. Tanaka, T. Okita, and H. H. Hng, "Field emission from zinc oxide nanoneedles on plastic substrates," nanotechnology **16**(8), 1300-1303 (2005).

47. C. X. Xu and X. W. Sun, "Field emission from zinc oxide nanopins," Applied Physics Letters **83**(18), 3806-3808 (2003).

48. S. H. Jo, J. Y. Lao, Z. F. Ren, R. A. Farrer, T. Baldacchini, and J. T. Fourkas, "Field-emission studies on thin films of zinc oxide nanowires," Applied Physics Letters **83**(23), 4821-4823 (2003).

49. C. J. Lee, T. J. Lee, S. C. Lyu, Y. Zhang, H. Ruh, and H. J. Lee, "Field emission from well-aligned zinc oxide nanowires grown at low temperature," Applied Physics Letters **81**(19), 3648-3650 (2002).

50. C. Brosseau and P. Talbot, "Effective permittivity of nanocomposite powder compacts," Ieee Transactions On Dielectrics And Electrical Insulation **11**(5), 819-832 (2004).
51. J. W. Haus, R. Inguva, and C. M. Bowden, "Effective-Medium Theory Of Nonlinear Ellipsoidal Composites," Physical Review A **40**(10), 5729-5734 (1989).
52. P. M. Guyot-Sionnest, "Optical Second Harmonic Generation And Infrared-Visible Sum Frequency Generation As Surface Probes," (University of California, Berkeley, USA, 1987).
53. Q. Zhao, X. Y. Xu, X. F. Song, X. Z. Zhang, D. P. Yu, C. P. Li, and L. Guo, "Enhanced field emission from ZnO nanorods via thermal annealing in oxygen," Applied Physics Letters **88**(3), 033102 (2006).
54. A. B. Djurisic, "Influence of annealing on stimulated emission in ZnO nanorods," Applied Physics Letters **89**(18), 183112 (2006).

CHAPTER 4
SHG OF CENTRO-SYMMETRIC ORGANIC ELECTRONIC MATERIALS

Organic electronic materials such as fullerene derivatives (C_{60}, C_{70} etc…), Rubrene[1, 2], NPB, Alq3, PEDOT:PSS and copper phthalocyanine (CuPc) are extensively studied for opto-electronic applications in as transitor and photo-voltaic cell fabrications[3, 4]. Understanding photo-electronic physics at surface/interface and bulk of these materials is the key issue for the advance/improvement of device design and performance of these ideal materials.

In this chapter, photo-electronic properties of fullerene (C_{60}) and copper phthalocyanine (CuPc) are investigated and reported with the aid of Second Harmonic Generation (SHG). These candidates are chosen because of the mystery that these centro-symmetric materials give relatively high second order NLO effect according to literatures[5-16]. There are disputes over the origin of the SHG mechanism from these centro-symmetric organic electronic materials. We give experimental results of SHG of C_{60} and CuPc and give a possible mechanism of high second order NLO effect of these materials which will be relevant for understanding transitor and photo-voltaic behaviors of various electronic materials. SHG is used as a diagnostic tool for studying interfacial electronic effect of C_{60} and CuPc.

C_{60} (fullerene) is widely studied in different fields such as superconductivity[17], photo-voltaic cell[18] because of its ultra-fine π conjugation which leads to a high conductivity and a high abundance of charge carrier. Ease of synthesis of C_{60}[19] makes it possible for the optical and the electrical characterization of C_{60} solid film which are essential for its further application in solid state electronic devices. Full-conjugated Metallo-phthalocyanine[20] (Pc) like copper phthalocyanine (CuPc) is also essential in organo-electronic application as its chemical and electronic properties can be highly tailored by substituting different metal in core or at benzene branch.

Three dimensional soccer-ball-like C_{60} possesses inversion symmetry and they configure themselves as face-center-cubic (f.c.c.) lattice structure at room temperature[21]. Macroscopically, C_{60} forms a centro-symmetric bulk structure. Its structure is shown in figure 4.1. Planar CuPc is also centro-symmetric molecule which possesses inversion center (D_{4h} symmetry). Under different temperature, they configure themselves into short-range α-crystalline structure or β-crystalline structure[22-24]. The chemical structure is shown below in figure 4.2.

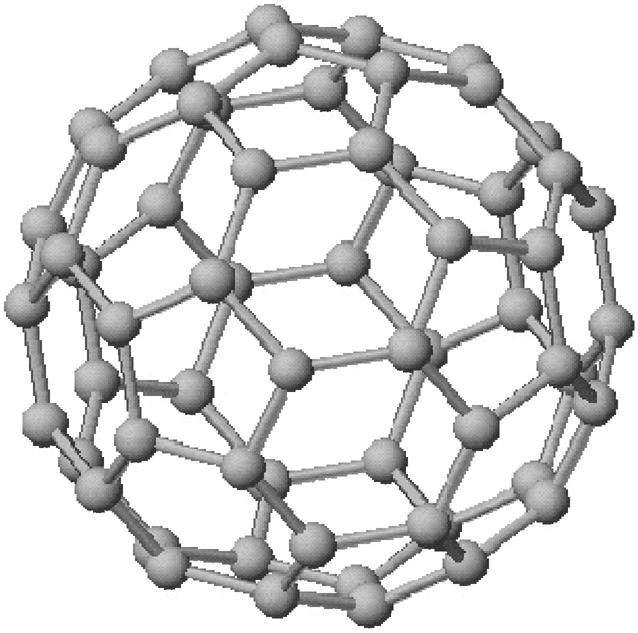

Figure 4.1 Structure of fullerene C_{60}

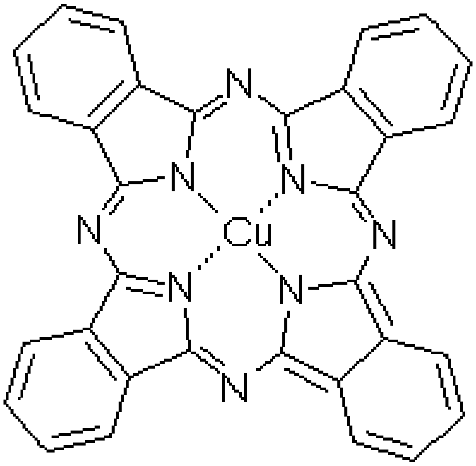

Figure 4.2 Structure of copper phthalocyanine CuPc

For centro-symmetric system, second-order nonlinear effect from the electric-dipole contribution vanishes as we have discussed in chapter 1. However, in 1991, H. Hoshi *et al.*[12] and X. K. Wang *et al.*[11] reported substantial second harmonic generation (SHG) from pristine C_{60} thin film. The second group reported that value of second order optical nonlinearity $\chi^{(2)}{}_{zzz}$ was around 1 pm/V for C_{60} thin films with thickness from 70 nm to

300 nm. In 1993, K. Kumagai *et al.*[14] was the first to measure high second order NLO susceptibility ($\chi^{(2)}_{zxx}$ ~ 20 pm/V) from CuPc of thickness from 4 nm to 200 nm. H. Hoshi *et al.*[15] further reported experimental evidence of high second order NLO susceptibility of the CuPc films.

Several research groups[6, 13, 15, 25-29] further discussed and proposed the mechanism of bulk SHG from centro-symmetric C_{60} and CuPc films as higher order electromagnetic effects such as electric-quadruple effect, magnetic dipole effect and magnetic dipole coupling on the basis of experimental and theoretical studies. These high order effects can be generally expressed as $E_{2\omega,i} = \sum_i \Gamma_{ijkl} E_j \partial_k E_l$ which was discussed in chapter 1. These higher order NLO mechanisms are of magnitude approximately $k \cdot d$ times smaller than pure second order effect ($E_{2\omega,i} = \sum_i \Delta_{ijk} E_j E_k$) where k is the wave number at fundamental wavelength and d is the molecular size of molecules. F. Kajzar *et al.*[30] reported that SHG of C_{60} was enhanced in multilayer structure composed of TPP or TPN. They attributed this effect to permanent interfacial charge transfer between C_{60} and the adjacent layer materials which was more or less justified by the presence of photo-induced charge transfer between conducting polymer and C_{60}[31]. Recently, L. Lozzi *et al.*[3] studied photo-induced charge hopping across interface of C_{60} and CuPc by soft x-ray photoemission spectroscopy. Obviously there is a necessity to review and revisit the origin of second order NLO effect in these centro-symmetric organic materials.

In this chapter, we present SHG results of pristine C_{60} thin film (from 10 nm to 150 nm) on 2 different substrates, glass or poly(methyl methacrylate) PMMA. In addition, SHG result of CuPc thin film (from 10 nm to 150 nm) on glass substrate is also presented. Large SHG effect of C_{60} and CuPc are showed and the origin of bulk second harmonic generation of C_{60} and CuPc are discussed more in detail.

4.1 Samples preparation

Samples were prepared according to the following procedures : C_{60} and CuPc, purchased from Aldrich company, were deposited on glass substrate or glass substrate spin-coated with 1μm-PMMA by vacuum evaporation using a thermal evaporation plant attached to a MBRAUN 200B glove box. The C_{60} and CuPc deposition were performed under pressure of around 10^{-6} mb at a rate of 0.1-0.2 nms^{-1} monitored by an Edwards FTM 7 quartz oscillator for film thickness measurement. C_{60} and CuPc films from 10 nm to 150 nm were deposited according to different evaporation time. Substrates were kept at room temperature during deposition.

Their absorption spectrum of C_{60} and CuPc at thickness of 10 nm are shown in figure 4.3 as below :

C60	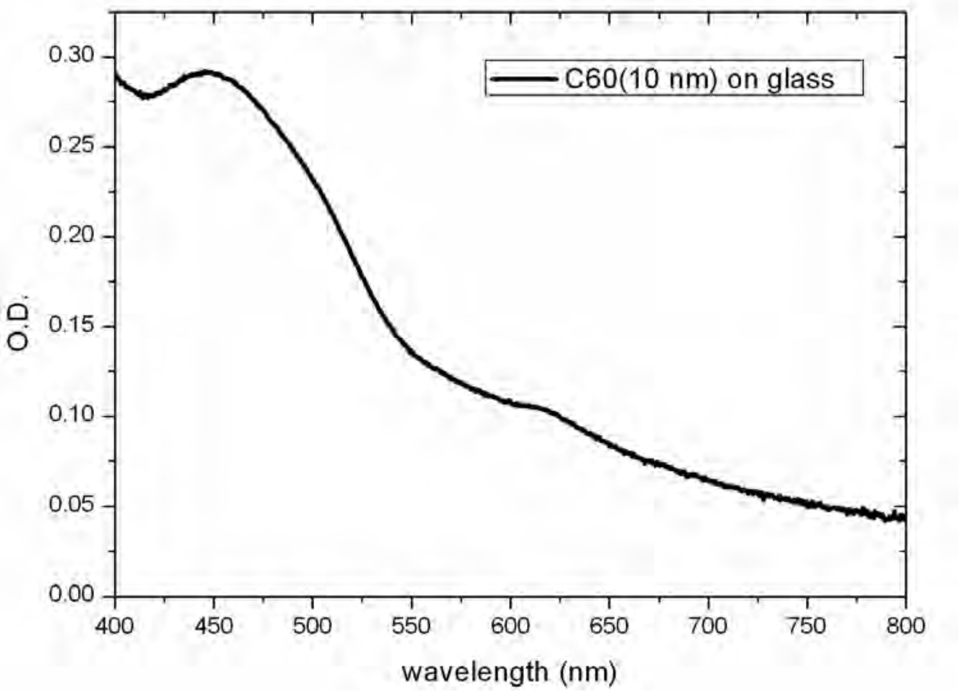

CuPc	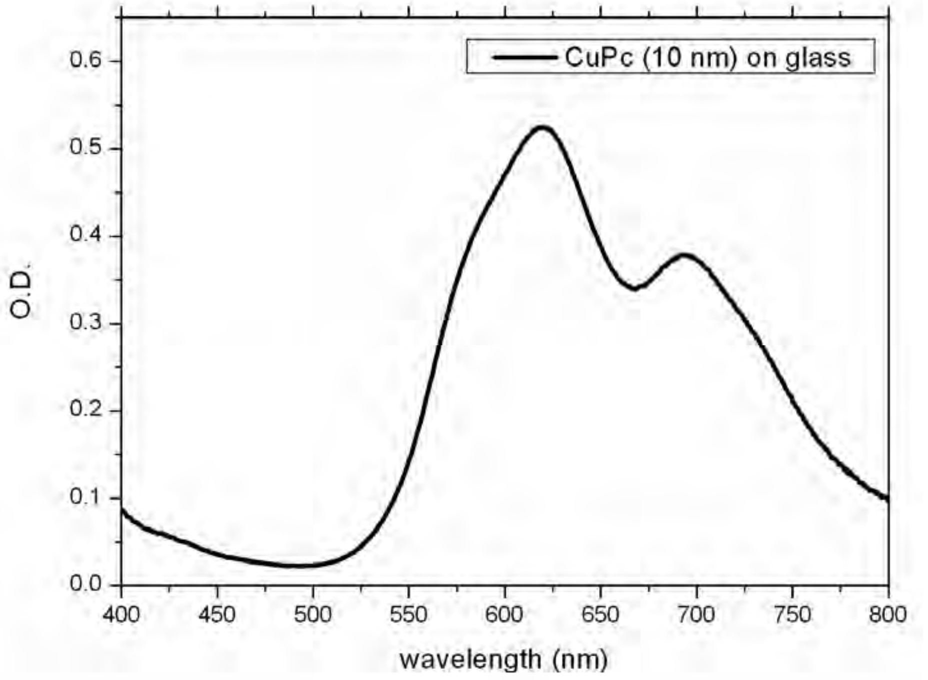

Figure 4.3 Absorption spectrum of C_{60} and CuPc of 10 nm thick on glass substrate

4.2 Second Harmonic Generation measurement

Second Harmonic Generation (SHG) measurement was performed for C_{60} thin films in forward and backward geometries (as shown in figure 4.4) at room temperature and pressure. For CuPc, SHG was done in forward geometry.

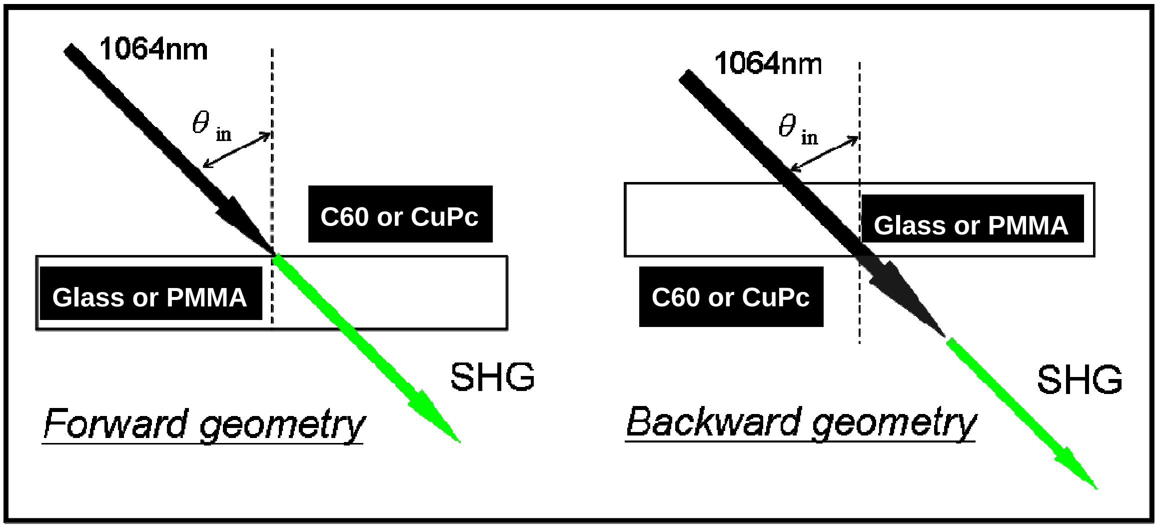

Figure 4.4 Forward and backward geometries of second harmonic generation (SHG) measurement on organic films

Schematic diagram of SHG measurement is shown in figure 4.5. Q-switch Nd:YAG laser of fundamental wavelength (λ) of 1064 nm was used as the source for SHG. Repetition rate of pulse was 3000 Hz and its power was around 300 mW. Weakly focusing s/p-polarized fundamental beam was introduced to samples and p-polarized SHG signal of with respect to different incident angle (θ_{in}) were recorded by photo-multiplier and then further processed with photon counting acquisition system. At the same time SHG signal from referencing NLO active material is obtained in the reference arm. To cancel out the impact of laser energy variations during experiment, sample SHG value has been normalized by division with a count from reference channel. To perform absolute measurements we used a x-cut quartz crystal (L=2.0 mm, $\chi^{(2)}_{eff}$=0.6 pm/V) as calibration reference. For each particular sample measurement, an instrument response function is determined by recording the Maker fringe from the x-cut quartz placed at the sample position.

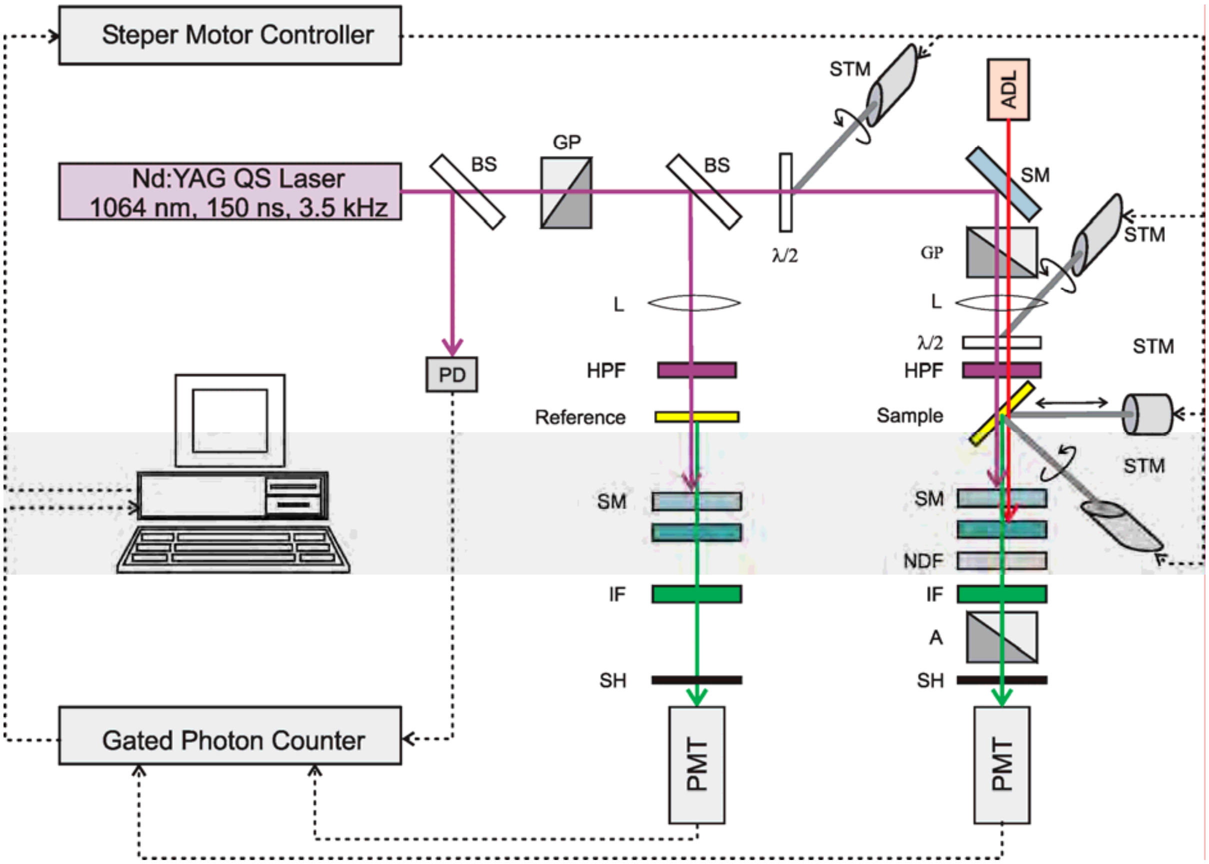

Figure 4.5 Schematic diagram of second harmonic generation (SHG) measurement. Computerized stepper motors (STM) are responsible for adjusting polarizations of EM fields and measurement geometry of sample. SHG signals from reference and from sample are simultaneously recorded by photo-multiplier tubes (PMT) and processed to gated photon counter. GP : glan polarizer, BS : beam splitter, HPF : high pass filter, L : lens, SM : selective mirror, NDF : neutral density filter, A : analyzer, IF : infrared filter, SH : shutter

4.3 Second Harmonic Generation results and discussions

4.3.1 Bulk second order NLO susceptibility

Second-harmonic generation (SHG) signal of p-polarization from samples was analyzed with SHG equation derived by W. N. Herman *et al.*[32] :

$$I_{SHG}^{p-p} = \frac{32\pi^3}{cA} \frac{\left[t^{1p}\right]^4 \left[t^{2p}\right]^2}{n_2{}^2 c_2{}^2} I_1{}^2 \left(\frac{2\pi L}{\lambda}\right)^2 (\chi^{(2)}{}_{eff})^2 e^{-2\delta_2} \frac{\sin^2\psi + \sinh^2\delta_2}{\psi^2 + \delta_2{}^2} \qquad (4.1)$$

where c is speed of light in vacuum, [$t^{i,p}$] are Fresnel transmission coefficients of p-polarized fundamental (i=1) and second harmonic (i = 2) EM fields, A is area of laser spot, n_i are refractive index of C_{60} or CuPc, I_1 is intensity of fundamental EM field (λ = 1064 nm), L is sample thickness, $\chi^{(2)}_{eff}$ is effective 2nd order nonlinear optical (NLO) susceptibility, δ_2 is absorption coefficient of C_{60} or CuPc at 532 nm, Ψ is the phase mismatch factor : $\left(\frac{2\pi L}{\lambda}\right)\left(n_1c_1 - n_2c_2\right)$ and c_i = $\sqrt{1-\left(\frac{\sin^2\theta'_{in}}{n_i^2}\right)}$ where θ'_{in} is the angle of incidence to C_{60} or CuPc thin film. Absorption of C_{60} or CuPc at 1064 nm is negligible. Pristine C_{60} or CuPc are centro-symmetric and we assume that they possess symmetry (6mm point group symmetry[33]) with respect to sample's surface normal (z-axis). Under this consideration, only $\chi^{(2)}_{zxx}$ and $\chi^{(2)}_{zzz}$ are non-zero independent 2nd order NLO susceptibilities (assume $\chi^{(2)}_{zxx} = \chi^{(2)}_{xzx}$). Figure 4.6a and 4.6b show respectively SHG $I^{p\text{-}p}_{SHG}$(norm.) (normalized to SHG signal of reference x-cut crystal) from C_{60} in p-polarized fundamental input (p-in)/p-polarized SHG output (p-out) measurement at different incident angle θ_{in}(rad.) and their best data fittings according to equation 4.1. SHG measurements were done in forward and backward geometries. Figure 4.7 below show SHG result of CuPc in p-in/p-out measurement configuration in forward geometry :

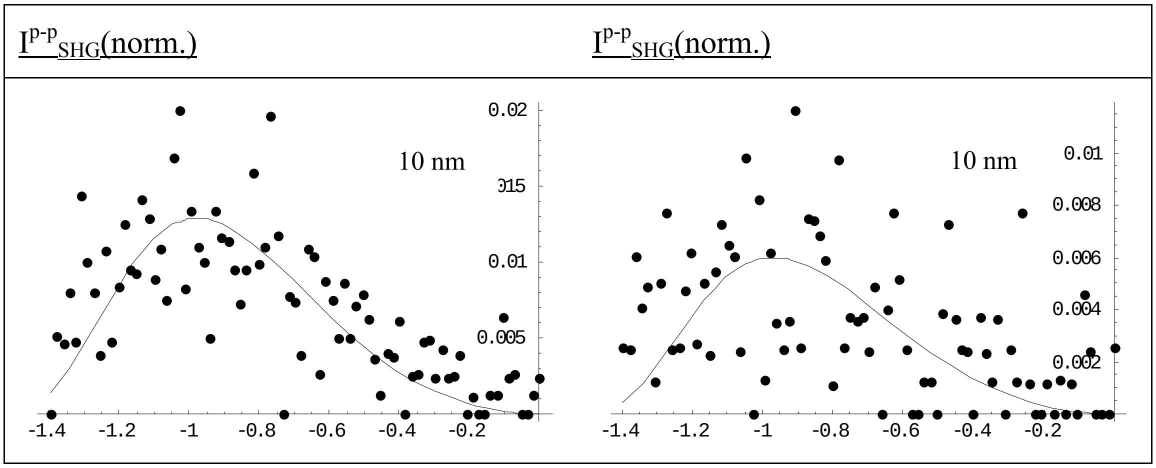

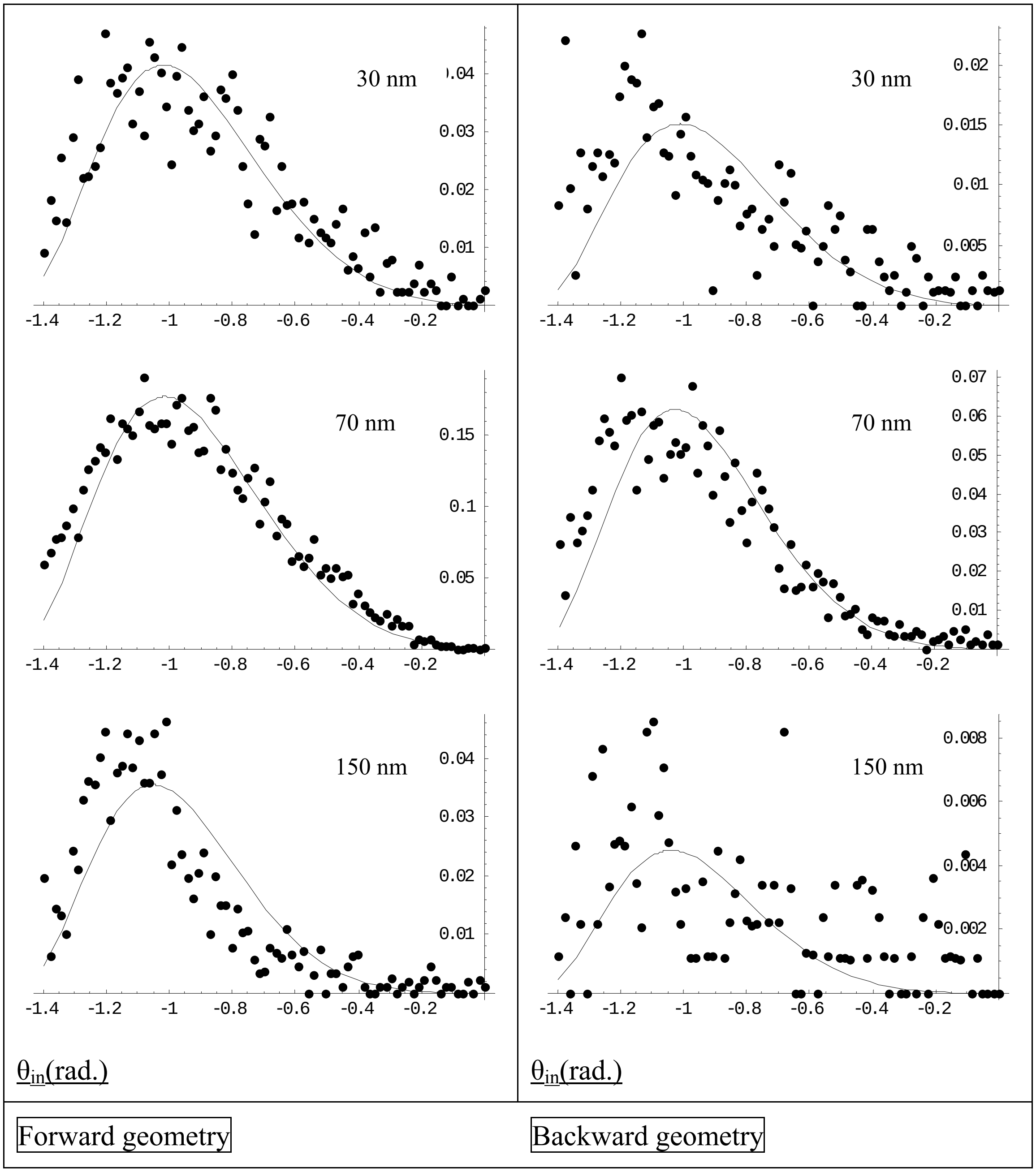

Figure 4.6a Second harmonic generation (SHG) and data fitting of C_{60} (thickness from 10 nm to 150 nm) on glass at p-in/p-out configuration in forward and backward geometries : I^{p-p}_{SHG}(norm.) vs θ_{in}(rad.)

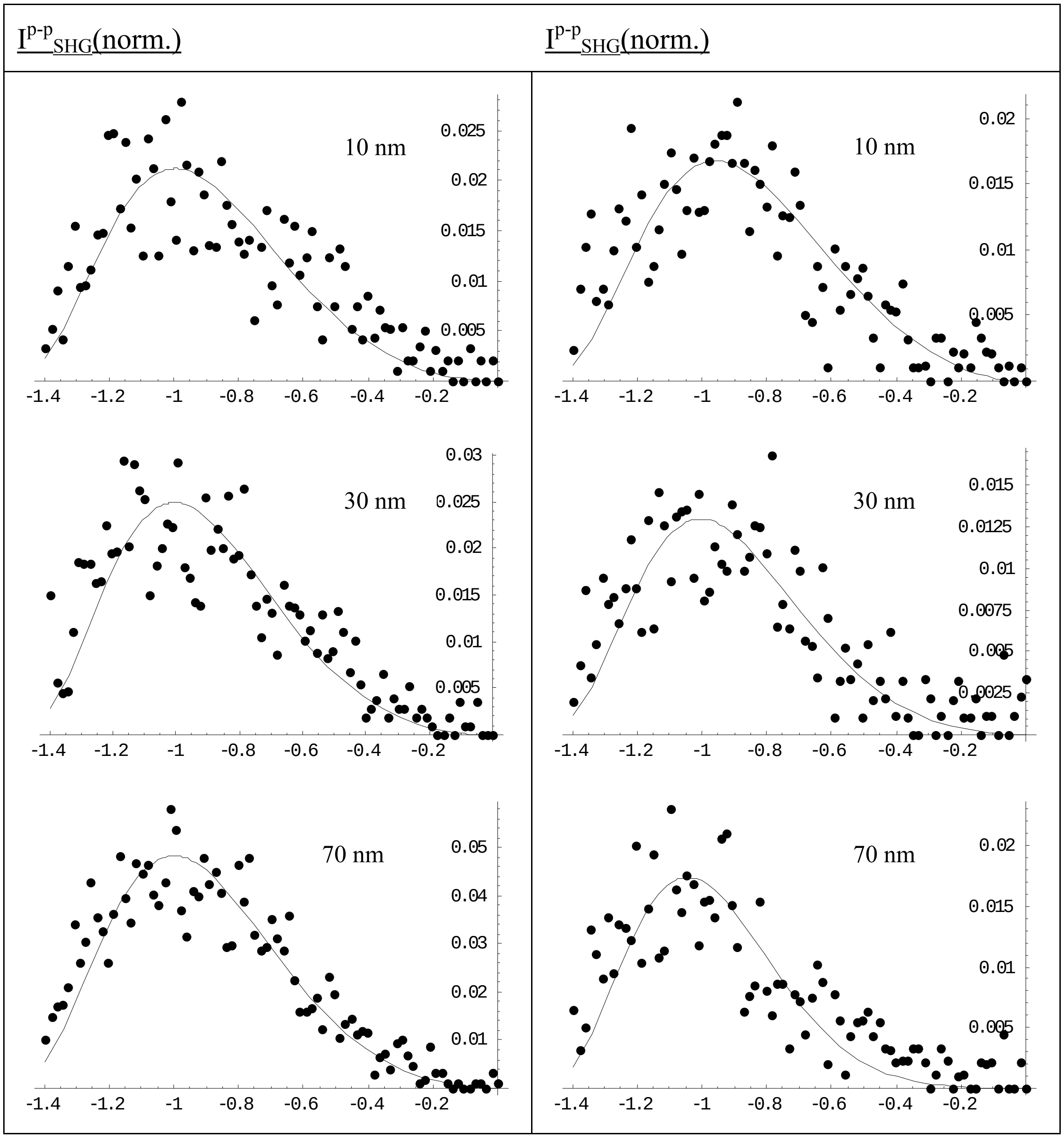
I^p-p_SHG(norm.)
I^p-p_SHG(norm.)
10 nm
0.025
0.02
0.015
0.01
0.005
-1.4 -1.2 -1 -0.8 -0.6 -0.4 -0.2
10 nm
0.02
0.015
0.01
0.005
-1.4 -1.2 -1 -0.8 -0.6 -0.4 -0.2
30 nm
0.03
0.025
0.02
0.015
0.01
0.005
-1.4 -1.2 -1 -0.8 -0.6 -0.4 -0.2
30 nm
0.015
0.0125
0.01
0.0075
0.005
0.0025
-1.4 -1.2 -1 -0.8 -0.6 -0.4 -0.2
70 nm
0.05
0.04
0.03
0.02
0.01
-1.4 -1.2 -1 -0.8 -0.6 -0.4 -0.2
70 nm
0.02
0.015
0.01
0.005
-1.4 -1.2 -1 -0.8 -0.6 -0.4 -0.2

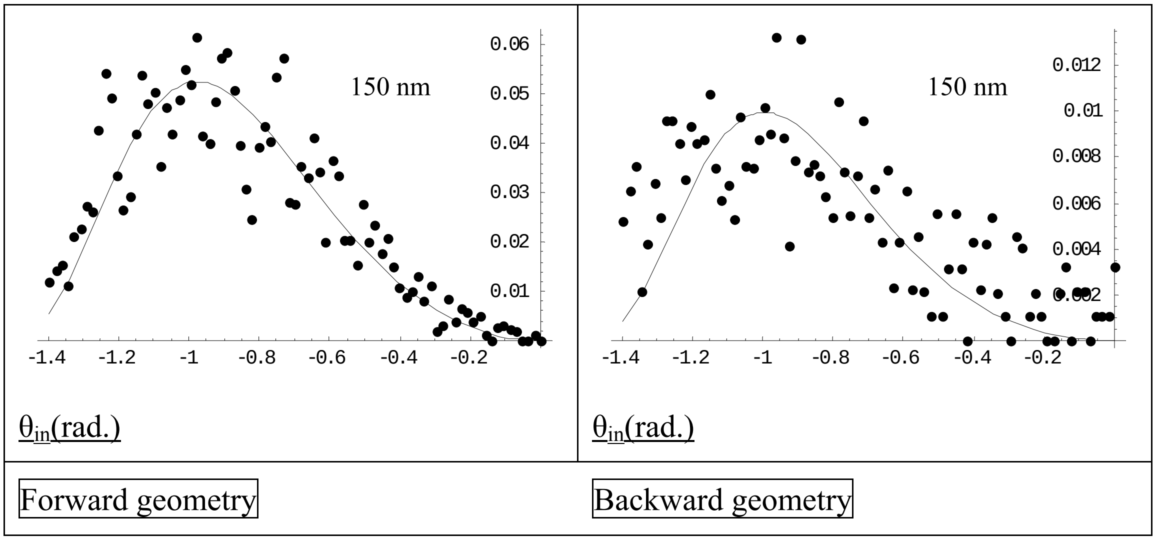

Figure 4.6b Second harmonic generation (SHG) and data fitting of C_{60} (thickness from 10 nm to 150 nm) on PMMA at p-in/p-out configuration in forward and backward geometries : $I^{p\text{-}p}_{SHG}$(norm.) vs θ_{in}(rad.)

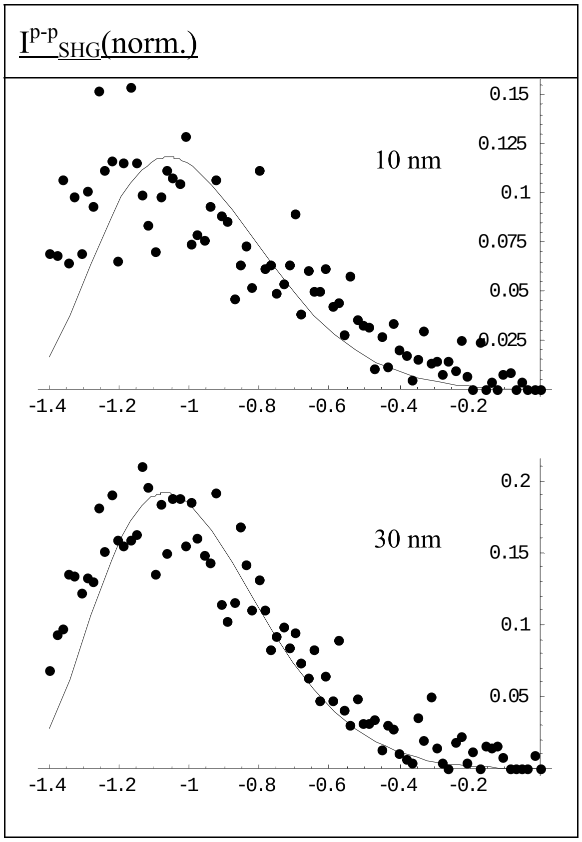

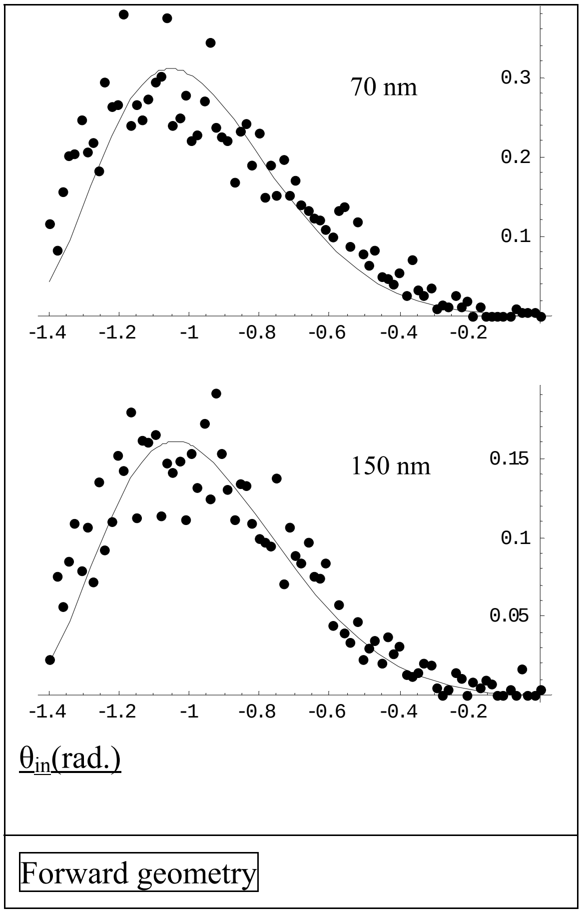

Figure 4.7 Second harmonic generation (SHG) and data fitting of CuPc (thickness from 10 nm to 150 nm) on glass at p-in/p-out configuration in forward geometry : $I^{p\text{-}p}_{SHG}$(norm.) vs θ_{in}(rad.)

Second order NLO susceptibilities $\chi^{(2)}_{zxx}$, $\chi^{(2)}_{zzz}$ obtained from data fitting are tabulated in table 4.1 and table 4.2. The second order optical nonlinearity is an order of magnitude higher than the previous findings by other researchers.

For C_{60} film of 10 nm, $\chi^{(2)}_{zzz}$ attains a significant value of around 50 pm/V. $\chi^{(2)}$ obtained for C_{60} on glass (C_{60}|glass) or on PMMA (C_{60}|PMMA) in forward and backward geometries measurement have, in general, slight difference. We attribute it to different bulk-invariant SHG contributions from interfaces : C_{60}|PMMA, C_{60}|glass or C_{60}|air. In addition, for CuPc film of 10 nm, $\chi^{(2)}_{zzz}$ attains a significant value of around 35 pm/V.

Sample&thickness(L)	Forward geometry		Backward geometry	
C_{60}|glass	$\chi^{(2)}_{zxx}$(pm/V)	$\chi^{(2)}_{zzz}$(pm/V)	$\chi^{(2)}_{zxx}$(pm/V)	$\chi^{(2)}_{zzz}$(pm/V)
10 nm	11.7	31.7	13	34.3
30 nm	4.6	26.5	4.1	26.2
70 nm	3.3	23.6	2.8	27.2
150 nm	0.6	7.0	0.8	4.0
C_{60}|PMMA	$\chi^{(2)}_{zxx}$(pm/V)	$\chi^{(2)}_{zzz}$(pm/V)	$\chi^{(2)}_{zxx}$(pm/V)	$\chi^{(2)}_{zzz}$(pm/V)
10 nm	9.9	46.1	15.4	50.2
30 nm	2.8	18.6	3.6	23.0
70 nm	1.4	10.3	1.8	15.1
150 nm	1.0	4.3	0.8	3.8

Table 4.1 SHG data fitting of 2nd order nonlinear susceptibilities $\chi^{(2)}_{zxx}$ and $\chi^{(2)}_{zzz}$ of C_{60} on glass or on PMMA in forward and backward geometries respectively

Sample&thickness(L)	Forward geometry	
CuPc|glass	$\chi^{(2)}_{zxx}$(pm/V)	$\chi^{(2)}_{zzz}$(pm/V)
10 nm	1.5	34.7
30 nm	0.52	15.9
70 nm	0.42	8.02
150 nm	0.18	2.7

Table 4.2 SHG data fitting of 2nd order nonlinear susceptibilities $\chi^{(2)}_{zxx}$ and $\chi^{(2)}_{zzz}$ of CuPc on glass in forward geometry

$\chi^{(2)}$ from C_{60} of the SAME thickness (L) on different substrates (glass or PMMA) are different which gives an insight on the interface-related mechanism of bulk SHG. In addition, inverse proportional relation of C_{60}/CuPc thickness (L) to $\chi^{(2)}$ reveals that bulk

SHG response from bulk C_{60}/CuPc could not be explained simply by higher order effects $E_{2\omega,i} = \sum_{i} \Gamma_{ijkl} E_j \partial_k E_l$ which gives L^2 dependence to SHG signal $I_{SHG} \alpha L^2 \Gamma_{eff} I_{\omega}^{2}$. The possible interfacial-related SHG mechanism will be discussed in the following section.

4.3.2 Limited spontaneous charge transfer across organic films and substrate

We propose that the bulk SHG response of C_{60} or CuPc thin film originates from interfacial charge transfer at interface of n-type C_{60} or p-type CuPc semiconductor and intrinsic semi-conducting glass or PMMA substrates. Electrons or holes are injected to substrate and counter charges are accumulated in the bulk C_{60} or CuPc. It is illustrated in figure 4.8.

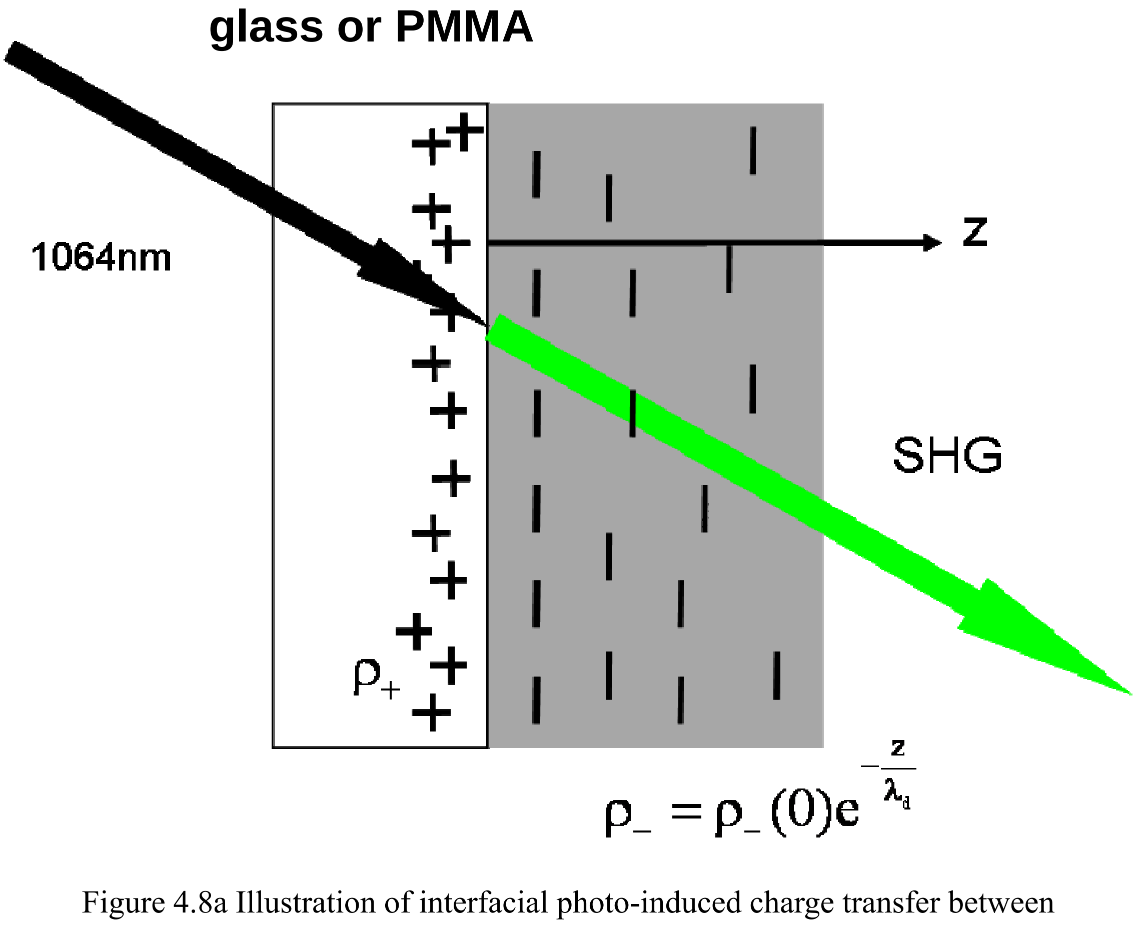

Figure 4.8a Illustration of interfacial photo-induced charge transfer between glass or PMMA and C_{60}

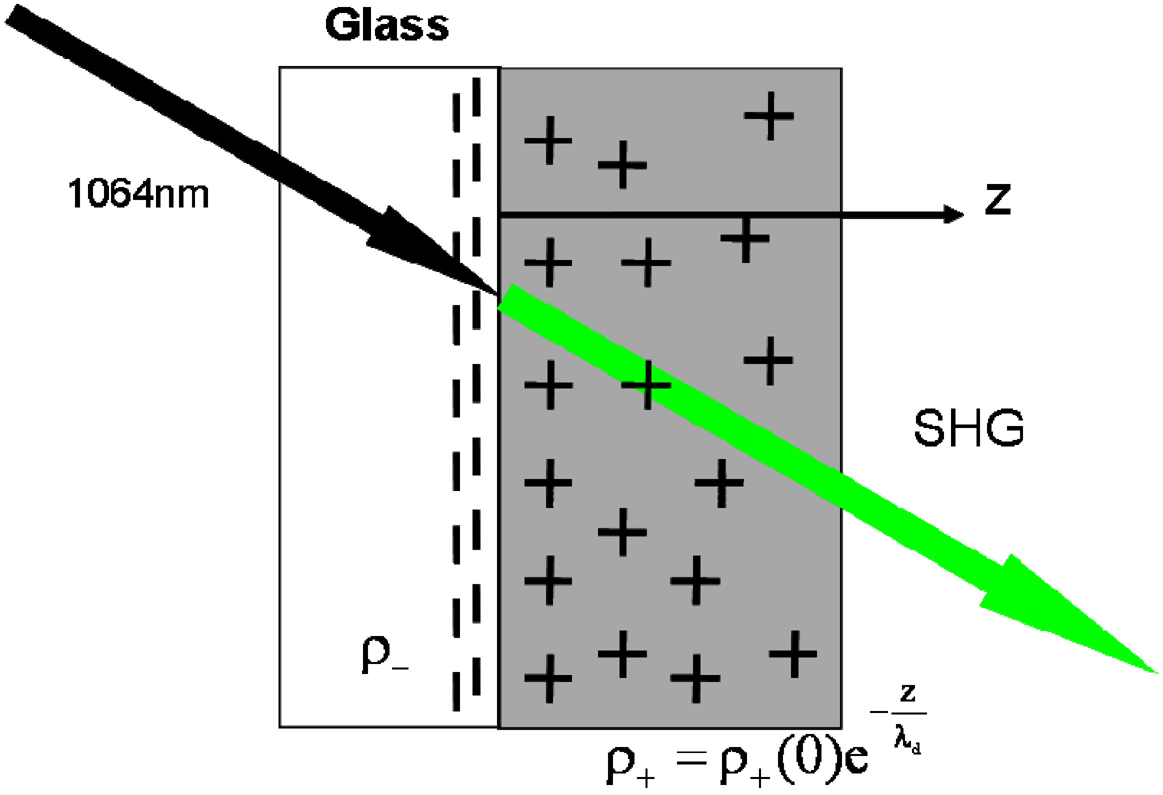

Figure 4.8b Illustration of interfacial photo-induced charge transfer between glass and CuPc

We assume that a thin sheet of electrons/holes (surface charge density : σ_- or σ_+) accumulates on the surface of substrates (Glass or PMMA). Electrons or holes are hosted in bulk volume of C_{60} or CuPc with surface charge density distribution : $\sigma_{-or+}(z) = \sigma_{-or+}(0)e^{-\left(\frac{z}{\lambda_d}\right)}$ where λ_d resembles Debye screening length which measures the ease of electron or hole diffusion in C_{60} or CuPc. Charge conservation gives $\sigma_{-or+} = \int_0^\infty \sigma_{+or-}(0)e^{-\left(\frac{z}{\lambda_d}\right)}dz$ and electron or hole density distribution in C_{60} or CuPc can be expressed as :

$$\sigma_{-or+}(z) = \frac{\sigma_{+or-}}{\lambda_d}e^{-\left(\frac{z}{\lambda_d}\right)} \tag{4.2}$$

Applying Gauss's law, the quasi-static electric field strength inside C_{60} or CuPc at the distance of z_0 nm from the substrate|film interface due to the spontaneous charge separation can be expressed as :

$$E(z_0) = \frac{1}{2\varepsilon}\left(\sigma_{-or+} - \int_0^{z_0} \frac{\sigma_{-or+}}{\lambda_d} e^{-\left(\frac{z}{\lambda_d}\right)} dz\right) \tag{4.3}$$

where ε is dielectric permittivity of medium. Model of the SHG from electric field induced second harmonic generation EFISHG is shown in figure 4.9 below :

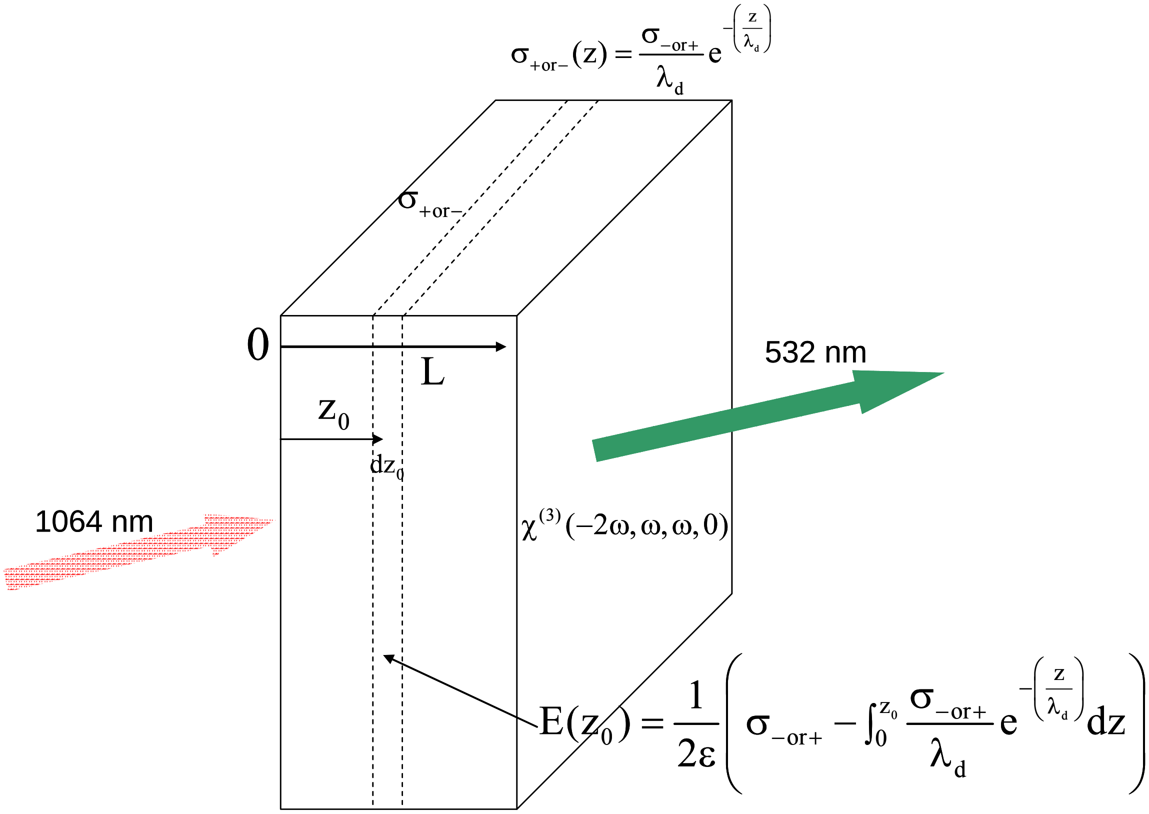

Figure 4.9 Model of SHG due to EFISHG from spontaneous interfacial charge transfer

With the expression of $E(z_0)$ in equation 4.3, second order NLO response from C_{60} or CuPc could be described as a electric-field-induced second harmonic generation (EFISHG) from bulk C_{60} or CuPc in forward geometry :

$$\chi^{(2)} = \int_0^L \chi^{(3)} E(z_0) \frac{1}{L} dz_0 = \frac{\sigma_{+\mathrm{or}-}}{2\varepsilon} \chi^{(3)} \int_0^L e^{-\left(\frac{z_o}{\lambda_d}\right)} \frac{1}{L} dz_0 \qquad (4.4)$$

$$\chi^{(2)} = \frac{\sigma_{+\mathrm{or}-}}{2\varepsilon} \chi^{(3)} \frac{\lambda_d \left(1 - e^{-\frac{L}{\lambda_d}}\right)}{L} \qquad (4.5)$$

where $\chi^{(3)}(-2\omega,\omega,\omega,0)$ is the 3rd order NLO susceptibility, L is sample thickness and we neglect the absorption at green for surface charge estimation.

To verify the validity of equation 4.5 for the understanding of bulk second order NLO response from C_{60} or CuPc, $\chi^{(2)}_{zzz}$ of C_{60} or CuPc on glass or on PMMA with different thickness (L) in forward geometry is approximated according to equation 4.5. Results are shown in figure 4.10a and figure 4.10b which give reasonable data fitting for thickness (L) dependence of second order NLO susceptibility.

It supports the hypothesis that a large SHG signal from centro-symmetric C_{60} or CuPc can be attributed to the EFISHG-type SHG due to the spontaneous charge transfer and the charge separation at C_{60} or CuPc|substrate interface.

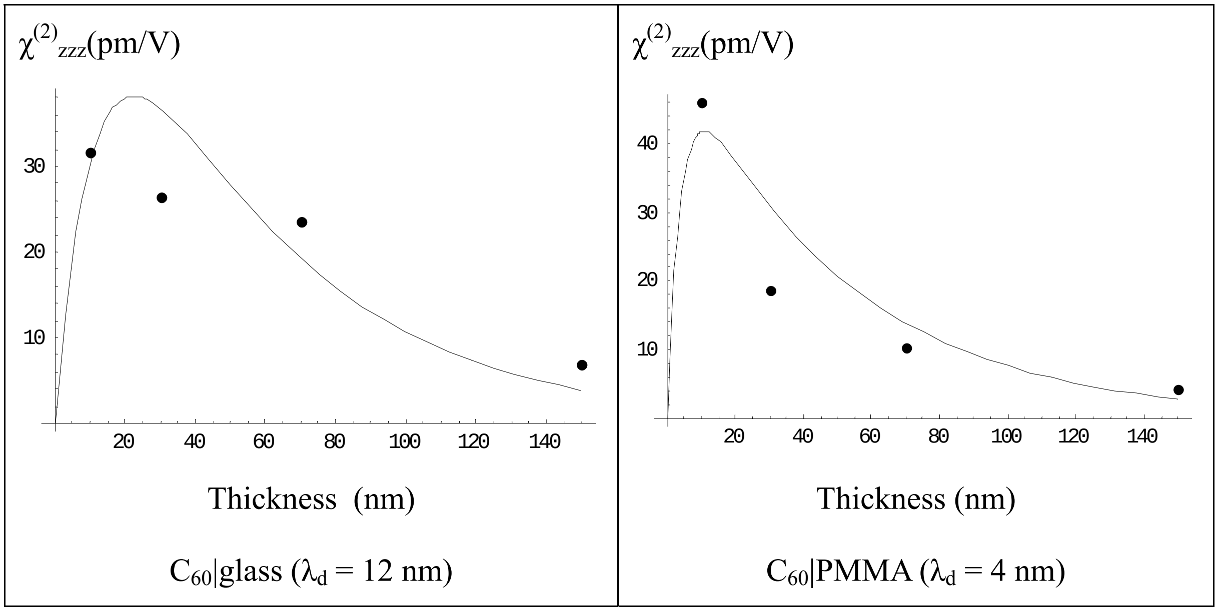

C_{60}|glass (λ_d = 12 nm)

C_{60}|PMMA (λ_d = 4 nm)

Figure 4.10a $\chi^{(2)}_{zzz}$ dependence to film thickness (L) on C_{60}|glass and C_{60}|PMMA with their solid line fitting according to equation 4.5

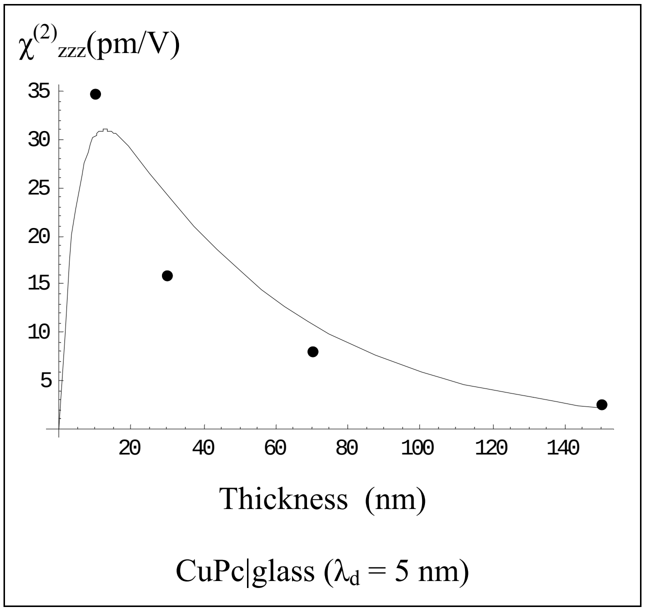

CuPc|glass (λ_d = 5 nm)

Figure 4.10b $\chi^{(2)}_{zzz}$ dependence to film thickness (L) on CuPc|glass with its solid line fitting according to equation 4.5

Amount of the accumulated charge $\int \sigma_{-\text{or}+} dV$ depends on charge trapping capacity of particular substrate material. The higher the capability of quasi-permanent photo-induced interfacial charge separation and trapping, the stronger the EFISHG-type second harmonic generation effect. According to the fitting of $\chi^{(2)}_{zzz}$ in function of the different thickness (nm) of C_{60} or CuPc on glass, Debye diffusion length[34] (λ_d) of C_{60} at glass interface doubles that of CuPc at glass interface upon spontaneous charge transfer.

4.3.3 Estimation of photo-induced interfacial charge transfer $\sigma_{+\text{or}-}$

From figure 4.10a and figure 4.10b, the fitting of $\chi^{(2)}_{zzz}$ in function of the sample thickness gives Debye diffusion length (λ_d) approximation and proportionality constant $\frac{1}{2\varepsilon}\sigma_{-\text{or}+}\chi^{(3)}$. We could estimate the amount of spontaneous charge transfer (σ_+ for n-type C_{60} and σ_- for p-type CuPc) from the proportionality constant $\frac{1}{2\varepsilon}\sigma_{-\text{or}+}\chi^{(3)}$ with the value of $\chi^{(3)}$ found previously.

For C_{60}|glass[30] : λ_d =12 nm and $\chi^{(3)} \sim 1.1 \bullet 10^{-18}\,\text{m}^2/\text{V}^2$.

$$\sigma_+ \sim 2.2 \bullet 10^{-4}\,\text{Cm}^{-2} \sim 2.2 \bullet 10^{-8}\,\text{Ccm}^{-2} \sim 1.4 \bullet 10^{11}\,\frac{\text{e}}{\text{cm}^2}$$

For C_{60}|PMMA : λ_d =4 nm and $\chi^{(3)} \sim 1.1 \bullet 10^{-18}\,\text{m}^2/\text{V}^2$.

$$\sigma_+ \sim 2.3 \bullet 10^{-3}\,\text{Cm}^{-2} \sim 2.3 \bullet 10^{-7}\,\text{Ccm}^{-2} \sim 1.4 \bullet 10^{12}\,\frac{\text{e}}{\text{cm}^2}$$

For CuPc|glass[35] : λ_d =5 nm and $\chi^{(3)} \sim 5.6 \bullet 10^{-20}\,\text{m}^2/\text{V}^2$

$$\sigma_- \sim 1.4 \bullet 10^{-2}\,\text{Cm}^{-2} \sim 1.4 \bullet 10^{-6}\,\text{Ccm}^{-2} \sim 8 \bullet 10^{12}\,\frac{\text{e}}{\text{cm}^2}$$

From above σ_{+or-} estimation of C60 or CuPc for the same measurement condition, it reveals that for CuPc, the amount of charge transfer at interface is an order higher than that for C_{60}. In addition, charge transfer depends on the nature of the substrate (glass/PMMA). Spontaneous interfacial charge transfer to PMMA is higher that that to glass (SiO_2) from C_{60}.

Preliminary work on EFISHG response of C_{60} gives further agreement to above discussion of C_{60} or CuPc SHG effect due to spontaneous interfacial charge transfer. A 30 nm thick C_{60} film was sandwiched between ITO electrodes for EFISHG measurement. Experimental result is shown in figure 4.11. With altering polarity (+/-) of various applied voltage (from -180 V to 180 V) to sample, EFISHG signal was recorded which was asymmetric with respect to polarity of applied external voltage. It proves that polar internal electric field is established across C_{60} due to our proposed mechanism of spontaneous interfacial charge transfer between C_{60} and substrates. Further studies is undergoing for quantifying the photo-induced charge transfer and trapping effect between C_{60}/CuPc and different substrates.

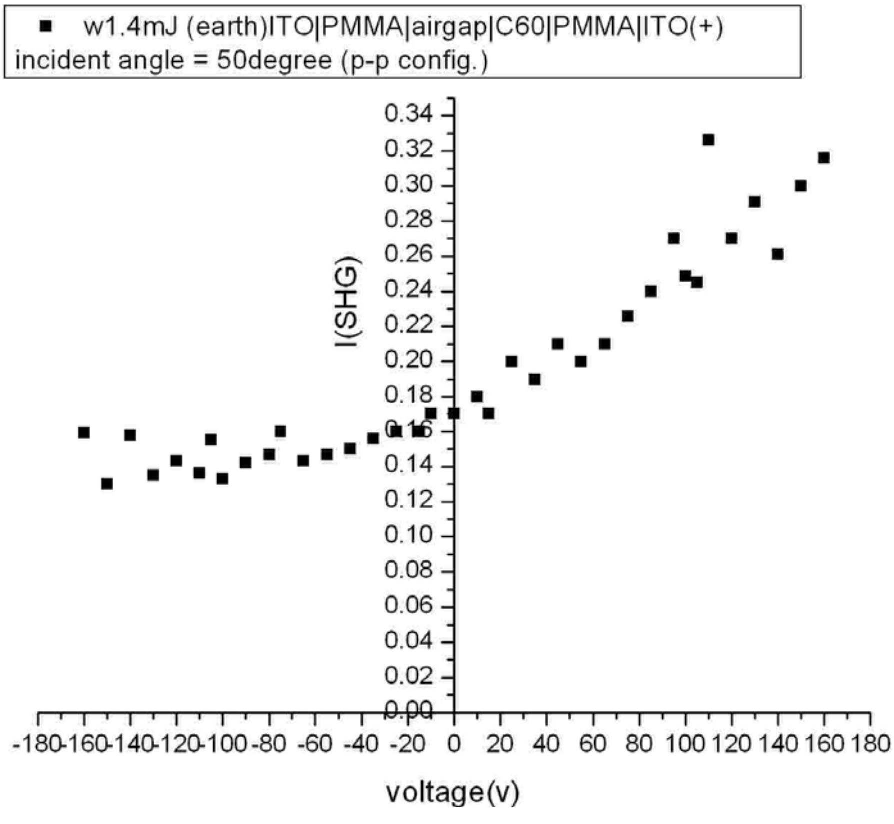

Figure 4.11 Asymmetric SHG signal response to external applied voltage on C60 thin film of 30 nm sandwiched by ITO electrodes

4.4 Quantitative study of charge diffusion at interface

In the previous section, we discussed the origin of SHG from the centro-symmetric C_{60} and CuPc. The EFISHG effect due to spontaneous interfacial charge separation between glass substrate and film is studied with SHG measurement which is contrary to the previous suggestions on the higher-order NLO effect. The interfacial charge separation would cause substantial change of surface voltage and this can be studied by Kelvin Probe technique[36-39].

As shown in figure 4.12 below, energy level diagram including Fermi level (E_F) of glass substrate (SiO_2), C_{60}, CuPc and electrode (Au) at open circuit. The difference of Fermi level between glass|film and electrode is donated as Contact Potential Difference (CPD). Fermi level of glass|film is adjusted due to spontaneous charge separation and thus, magnitude of CPD with reference to Au electrode is varied according to amount of charge transferred and accumulated. At closed circuit configuration, charges will be stored at capacitor for establishing a capacitance voltage of counter CPD in close-circuit for Fermi-level matching. Alternation of electrode probe-film distance d(t) by piezoelectric device leads to charging and discharging of capacitor. An external voltage source supplying voltage of V_{CPD} (equivalent to magnitude of CPD) to 'zero' circuit current giving a direct measurement of difference in Fermi level (CPD) and thus giving a quantitative measurement of Fermi leveling due to spontaneous interfacial charge transfer at glass/PMMA-film interface.

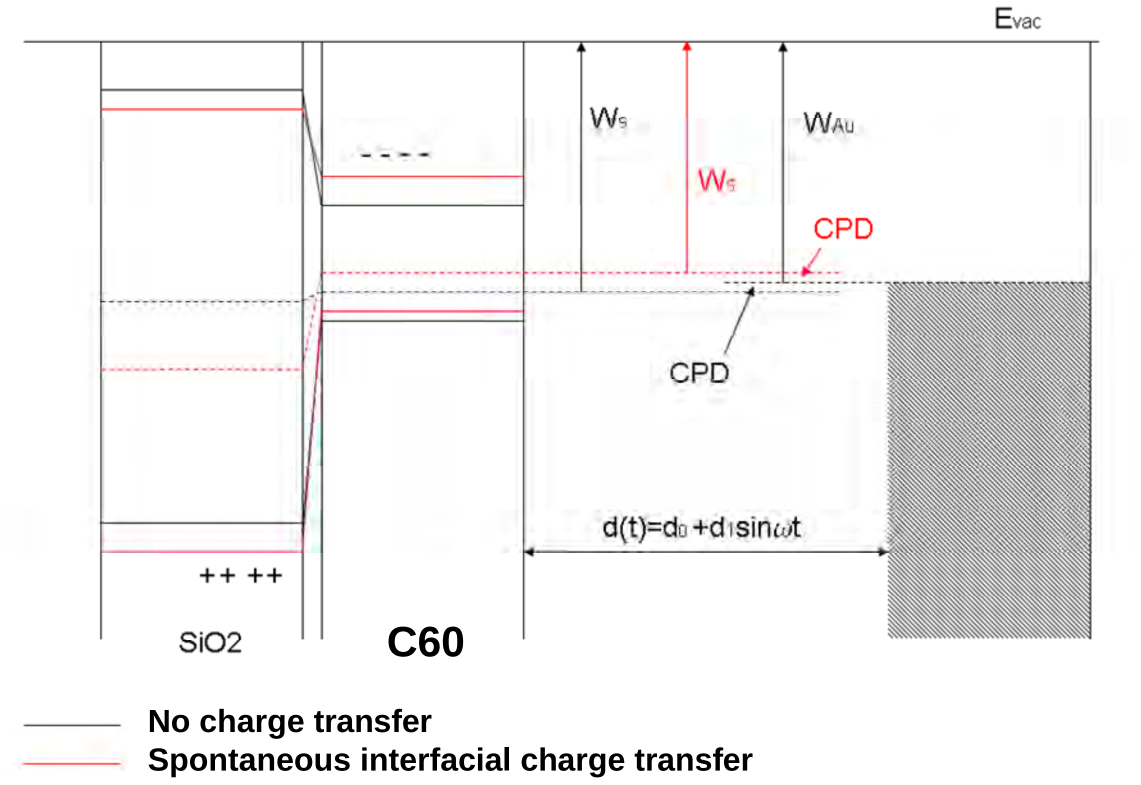

Figure 4.12a Energy level diagram of C_{60}|glass with gold electrode at a distance of d(t) with or without spontaneous interfacial charge transfer

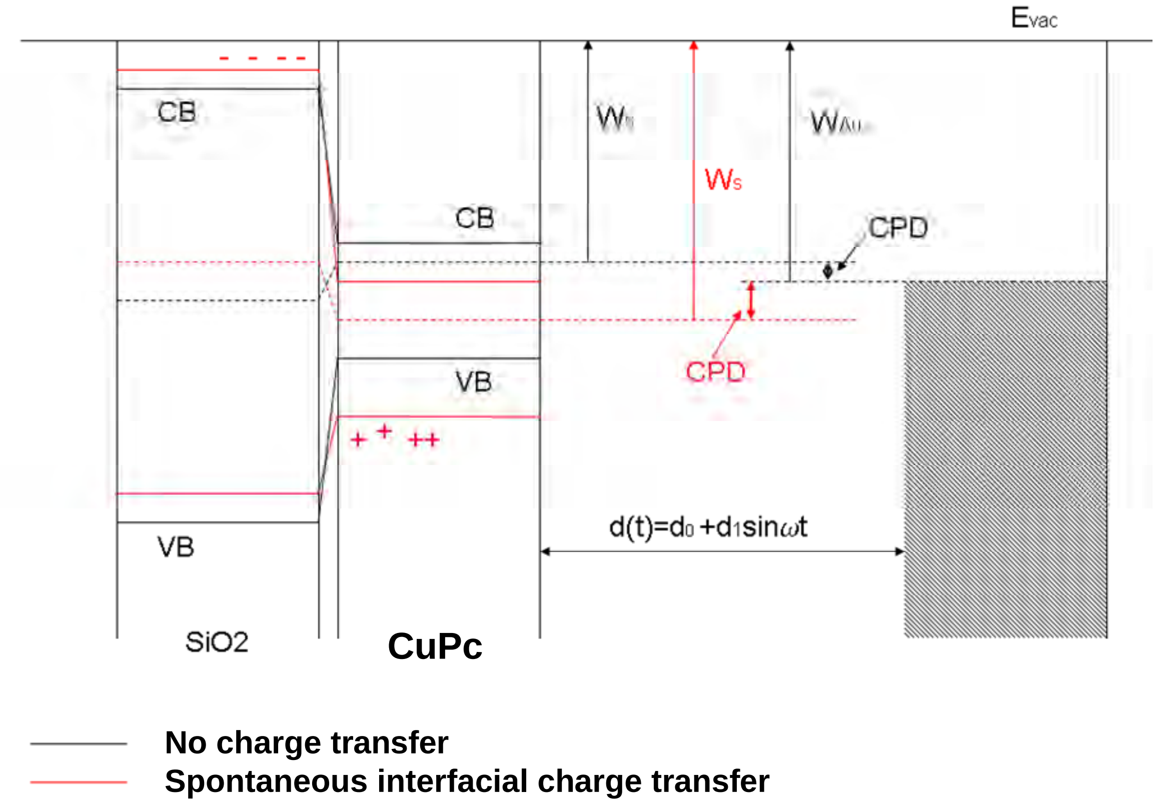

Figure 4.12b Energy level diagram of CuPc|glass with gold electrode at a distance of d(t) with or without spontaneous interfacial charge transfer

4.5 Chapter summary

Second order NLO response of centro-symmetric organic film of C_{60} and CuPc was discussed. Researchers proposed that the high NLO response from C_{60} and CuPc is mostly originated from higher-order NLO process. We performed SHG measurement of C_{60} and CuPc with different thickness (from 10 nm to 150 nm) on glass or PMMA.

Second order NLO susceptibility $\chi^{(2)}$ of samples is of an order higher than the previous findings. Thickness dependence of sample to $\chi^{(2)}$ shows that SH response should not be probably originated significantly from other SHG mechanisms like electric-quadruple effect, magnetic dipole effect or magnetic dipole coupling effect. Furthermore, SH response of organic material (C_{60}) depends on substrate nature (glass or PMMA) which indicates that such large SHG response is closely related to interface electronic effect.

We suggest that large SH response from n-type semi-conducting C_{60} and p-type semi-conducting CuPc on intrinsic semiconductor (SiO_2 or PMMA) correspond largely to Electric Field Induced Second Harmonic Generation (EFISHG) due to electric field established across interface. Electric field induced across interface is caused by the spontaneous charge across interface of substrate and organic film (either n-type or p-type). Amount of charge transferred depends largely on materials and substrate nature (e.g. Fermi-level matching). The spontaneous surface charge density $\sigma_{-\text{or}+}$ was estimated with third order NLO susceptibility $\chi^{(3)}$ found from literatures.

For further understanding the EFISHG of C_{60} and CuPc which give large SHG effect from the 'charging' of substrate and organic film, we are going to perform surface voltage measurement called Kelvin Probe technique. With Kelvin Probe, it gives an opportunity to give quantitative analysis of amount of charge trapping both in film and in substrate during illumination. Kelvin probe mechanism was briefly introduced at the last section of this chapter.

Chapter references

1. C. Goldmann, C. Krellner, K. P. Pernstich, S. Haas, D. J. Gundlach, and B. Batlogg, "Determination of the interface trap density of rubrene single-crystal field-effect transistors and comparison to the bulk trap density," Journal Of Applied Physics 99(3), 034507 (2006).
2. H. Najafov, I. Biaggio, V. Podzorov, M. F. Calhoun, and M. E. Gershenson, "Primary photoexcitations and the origin of the photocurrent in rubrene single crystals," Physical Review Letters 96(5) ,056604 (2006).
3. L. Lozzi, S. Santucci, and S. La Rosa, "Photoemission investigation on copper phthalocyanine: fullerene blend film," Applied physics letters 88(13), 133505 (2006).
4. J. Nelson, S. A. Choulis, and J. R. Durrant, "Charge recombination in polymer/fullerene photovoltaic devices," Thin Solid Films 451-52, 508-514 (2004).
5. F. Kajzar, C. Taliani, R. Zamboni, S. Rossini, and R. Danieli, "Nonlinear optical properties of fullerenes," Synthetic Metals 77(1-3), 257-263 (1996).
6. K. Kuhnke, M. Epple, and K. Kern, "Second harmonic spectroscopy of fullerenes," Chemical Physics Letters 294, 241-247 (1998).
7. K. Kuhnke, R. Becker, and K. Kern, "Dynamics of second harmonic generation at the C60/quartz interface," Chemical Physics Letters 257, 569-575 (1996).
8. D. Wilk, D. Johannsmann, C. Stanners, and Y. R. Shen, "2nd-Harmonic Generation From C-60 Thin-Films At 1.064-Mu-M," Physical Review B **51**(15), 10057-10067 (1995).
9. S. J. Qin, W. M. You, and Z. B. Su, "2nd-Harmonic Generation From The Quadrupole Response In C-60 Films," Physical Review B **48**(23), 17562-17568 (1993).
10. F. Kajzar, C. Taliani, R. Zamboni, S. Rossini, and R. Danieli, "Nonlinear optical properties of sublimed C60 thin film," Synthetic Metals 54, 21-32 (1993).
11. X. K. Wang, T. G. Zhang, W. P. Lin, S. Z. Liu, G. K. Wong, M. M. Kappes, R. P. H. Chang, and J. B. Ketterson, "Large second harmonic response of C60 thin films," Applied Physics Letters 60, 810-812 (1991).
12. H. Hoshi, N. Nakamura, Y. Maruyama, T. Nakagawa, S. Suzuki, H. Shiromaru, and Y. Achiba, "Optical Second and Third harmonic generations in C60 film,"

Japanese journal of applied physics 30, L1397-L1398 (1991).

13. H. Hoshi, T. Yamada, K. Ishikawa, H. Takezoe, and A. Fukuda, "Anisotropic second-harmonic generation of electric quadrupolar origin in copper phthalocyanine films epitaxially grown by molecular-beam epitaxy," Physical Review B 53(19), 12663-12665 (1996).
14. K. Kumagai, G. Mizutani, H. Tsukioka, T. Yamauchi, and S. Ushioda, "2nd-Harmonic Generation In Thin-Films Of Copper Phthalocyanine," Physical Review B 48(19), 14488-14495 (1993).
15. H. Hoshi, T. Yamada, K. Kajikawa, K. Ishikawa, H. Takezoe, and A. Fukuda, "In-situ observation of SHG and its origin in vacuum deposited copper phthalocyanine film," Molecular Crystals And Liquid Crystals Science And Technology Section A-Molecular Crystals And Liquid Crystals 267, 1-6 (1995).
16. H. Hoshi, T. Yamada, K. Ishikawa, H. Takezoe, and A. Fukuda, "2nd-Harmonic Generation In Centrosymmetric Molecular Films - Analysis Under Anisotropic Conditions," Physical Review B 52(16), 12355-12365 (1995).
17. A. F. Hebard, M. J. Rosseinsky, R. C. Haddon, D. W. Murphy, S. H. Glarum, T. T. M. Palstra, A. P. Ramirez, and A. R. Kortan, "Superconductivity At 18-K In Potassium-Doped C-60," Nature **350**(6319), 600-601 (1991).
18. H. Hoppe and N. S. Sariciftci, "organic solar cells: an overview," journal of materials research 19(7), 1924-1945 (2004).
19. W. Kratschmer, K. Fostiropoulos, and D. R. Huffman, "The Infrared And Ultraviolet-Absorption Spectra Of Laboratory-Produced Carbon Dust - Evidence For The Presence Of The C-60 Molecule," Chemical physics letters 170(2-3), 167-170 (1990).
20. G. delaTorre, T. Torres, and F. AgulloLopez, "The phthalocyanine approach to second harmonic generation," Advanced Materials 9(3), 265 (1997).
21. P. A. Heiney, J. E. Fischer, A. R. McGhie, W. J. Romanow, A. M. Denenstein, J. P. McCauley, A. B. Smith, and D. E. Cox, "Orientational Ordering Transition In Solid C60," Physical Review Letters 66(22), 2911-2914 (1991).
22. O. D. Gordan, M. Friedrich, and D. R. T. Zahn, "The anisotropic dielectric function for copper phthalocyanine thin films," Organic Electronics 5(6), 291-297 (2004).
23. L. Lozzi, S. Santucci, S. La Rosa, B. Delley, and S. Picozzi, "Electronic structure of crystalline copper phthalocyanine," Journal Of Chemical Physics 121(4), 1883-1889 (2004).

24. O. Berger, W. J. Fischer, B. Adolphi, S. Tierbach, V. Melev, and J. Schreiber, "Studies on phase transformations of Cu-phthalocyanine thin films," Journal Of Materials Science-Materials In Electronics 11(4), 331-346 (2000).
25. Y. Luo, P. Norman, P. Macak, and H. Agren, "nonlinear optical susceptibilities of fullerene in the condensed phase," physica review B 61(4), 3060-3066 (2000).
26. K. Harigaya, "Nonlinear optical response from excitons in C-60, C-70, and higher fullerenes," Journal Of Luminescence 76-7, 652-654 (1998).
27. K. C. Rustagi, S. V. Nair, and L. M. Ramaniah, "Nonlinear optical response of fullerenes," Progress In Crystal Growth And Characterization Of Materials 34(1-4), 81-93 (1997).
28. J. R. Lindle, R. G. S. Pong, F. J. Bartoli, and Z. H. Kafafi, "Nonlinear-Optical Properties Of The Fullerenes-C-60 And Fullerenes-C-70 At 1.064-Mu-M," Physical Review B 48(13), 9447-9451 (1993).
29. Y. Wang and L. T. Cheng, "Nonlinear Optical-Properties Of Fullerenes And Charge-Transfer Complexes Of Fullerenes," Journal Of Physical Chemistry 96(4), 1530-1532 (1992).
30. F. Kajzar, Y. Okada-Shudo, C. Meritt, and Z. Kafafi, "Second- and third-order nonlinear optical properties of multilayer and composite C-60-based thin films," Synthetic Metals 94(1), 91-98 (1998).
31. N. S. Sariciftci, L. Smilowitz, A. J. Heeger, and F. Wudl, "Photoinduced Electron-Transfer From A Conducting Polymer To Buckminsterfullerene," Science 258(5087), 1474-1476 (1992).
32. W. N. Herman and L. M. Hayden, "Maker Fringes Revisited - 2nd-Harmonic Generation From Birefringent Or Absorbing Materials," Journal Of The Optical Society Of America B-Optical Physics 12(3), 416-427 (1995).
33. Y. R. Shen, *The Principles of Nonlinear Optics* (John Wiley & Sons, Inc., USA, 1984).
34. S. M. Sze, *Physics of Semiconductor Devices*, Second ed. (JOHN WILEY & SONS INC., 1981).
35. P.-A. Chollet, F. Kajzar, and J. Le Moigne, "Structure and nonlinear optical properties of copper phthalocyanine thin films," The SPIE Proceeding 1273, 87-98 (1990).
36. V. Palermo, M. Palma, and P. Samori, "Electronic characterization of organic thin films by Kelvin probe force microscopy," Advanced Materials 18(2), 145-164 (2006).
37. L. Kronik and Y. Shapira, "Surface photovoltage phenomena: theory, experiment,

and applications," Surface Science Reports 37(1-5), 1-206 (1999).

38. K. Besocke and S. Berger, "Piezoelectric driven Kelvin probe for contact potential difference studies," Review of Scientific Instruments 47(7), 840-842 (1976).

39. M. Pfeiffer, K. Leo, and N. Karl, "Fermi level determination in organic thin films by the Kelvin probe method," Journal of Applied Physics 80(12), 6880-6883 (1996).

GENERAL CONCLUSION

In chapter 2, we demonstrated the feasibility of Second Harmonic Generation (SHG) and All-Optical Poling (AOP) as an non-invasive sensitive diagnostic tools to study stability and nonlinearity of 2 different types of NLO azo-polymer system : Guest-Host and LBL.

Generally speaking, SHG monitors the first order NLO effect and so, SHG sensitivity to dye motion of NLO system would be much higher comparing to other techniques like Birefrigence (BR) or Electric Field Induced Second Harmonic Generation (EFISHG). With the development of AOP technique as a diagnostic tool, non-perturbated (dark) dipole motion (relaxation) in polymer matrices can be studied.

From the $\chi^{(2)}$ relaxation studies of polymers with different rigidity upon different extend of photo-induced isomerization during AOP, we verify that polymer viscosity surrounding azo-dye is strengthened. It is contrary to the commonly accepted argument that photo-isomerization would loosen NLO azo-polymer and the polar orientation stability of NLO azo-polymer becomes lower if the poling involves photo-isomerization (like PAP and AOP) instead of pure electric means (like CP and TAP). An explanation of polymer hardening upon photo-isomerization in AOP was given. Moreover, we found out that dipolar orientation stability of azo-dye in polymer is no longer governed only by the glass transition temperature of polymer host which has been already reported previously. Higher order polymer local relaxation (like beta relaxation) would affect the rotational stability of azo-dye in polymer.

We studied SHG of azo-dye-grafted NLO polymer, which was assembled with Layer-By-Layer (LBL) technique. We found that increasing number of self-assembling layer would decrease the alignment capability of grafted azo-dye molecules and we showed that the incorporation of salt in polyelectrolytes during LBL process can enhance azo-dye alignment. In addition, we developed a method (secondary poling by AOP) for studying the orientation stability of intrinsic azo-dye alignment in LBL film. With a ‘restoring torque’ model, we could compare and access stability of azo-dye alignment in LBL films which is potentially useful in the future as a diagnostic tool for study LBL film stability and forming mechanism.

In order understand further the effect of AOP (photo-induced isomerization) to polymer hardening, we would like to emply Positron Annihilation Spectroscopy (PAS) to study the free volume distribution in polymer upon different duration of AOP (photo-induced isomerization). Tracking the temporal change of polymer free volume upon AOP would indeed give deep insight of the polymer hardening feature by consecutive dipolar rotation and volumetric expansion (contraction).

In chapter 3, we discussed second order NLO susceptibility of polar inorganic crystal zinc oxide ZnO of crystal size from mm to nm. ZnO single crystal of orientation <0001> was studied with Second Harmonic Generation (SHG) and its second order NLO response obtained is approximate to standard theoretical estimation and previous experimental studies. However, if the size of ZnO crystal diminishes to nano-scale (Nano-Rod NR), its second order NLO response differs tremendously.

We compared the relative sign and the magnitude of non-vanishing second order NLO susceptibilities between mm-scale single crystal and nm-scale single crystal (NR). We find that effective second order NLO response of nano-scale single crystal (NR) is far higher than that of mm-scale single crystal. In addition, such increase in second order NLO response depends critically on the geometry of the nm-scale single crystal : Big enhancement along longitudinal axis (polar c-axis) of NR. We propose that effective charge conductivity along NR's surface facilitates charge separation at NR's ends which creates a relatively large local electric field across NR. Large second order NLO response is due to significant contribution from electric field induced second harmonic generation (EFISHG) effect.

We did an estimation of electric field strength established across NR for 5-hrs as-grown ZnONR sample. Its magnitude could be as high as 20 $V\mu m^{-1}$. Surface charge accumulation on the sample was also estimated. The existence of local electric field due to charge accumulation at NRs' ends is justified further in the SHG experiment of as-grown ZnONR sample immersed in different dielectric environment. Higher SHG response for ZnONR at environment of higher dielectric constant indicates that charge accumulation at NRs' ends is enhanced, giving bigger SHG from EFISHG contribution.

At last, we presented SHG measurement of ZnONR annealed at different gas like air, N_2 and O_2. Researchers generally accept that gas annealing minimizes the number of different defects at the surface and in the bulk respectively. This would strengthen the charge conductivity at surface and improve charge accumulation at NRs' ends. SHG results of annealed ZnONR samples show that SHG response of all annealed ZnONR samples increase with respect to an as-grown sample. However, the relation between SHG enhancement to nature of annealing gas is still not fully understood.

In chapter 4, second order NLO response of centro-symmetric organic film of C_{60} and CuPc was discussed. Researchers proposed that high NLO response from C_{60} and CuPc is originated from higer-order NLO process. We performed SHG measurement of C_{60} and CuPc with different thickness (from 10 nm to 150 nm) on glass or PMMA.

Second order NLO susceptibility $\chi^{(2)}$ of samples is of an order higher than the previous findings. Thickness dependence of sample to $\chi^{(2)}$ shows that SH response should not be probably originated significantly from other SHG mechanisms like electric-quadruple effect, magnetic dipole effect or magnetic dipole coupling effect. Furthermore, SH response of organic material (C_{60}) depends on substrate nature (glass or PMMA) which indicates that such large SHG response is closely related to interface electronic effect.

We suggest that large SHG response from n-type semi-conducting C_{60} and p-type semi-conducting CuPc on intrinsic semiconductor (SiO_2 or PMMA) correspond largely to Electric Field Induced Second Harmonic Generation (EFISHG) due to electric field established across interface. Electric field induced across interface is established due to the spontaneous interfacial charge transfer between substrate and organic film (either n-type or p-type). Amount of charge transferred depends largely on materials and substrate nature (e.g. Fermi-level matching). Accumulated charge density $\sigma_{-\mathrm{or}+}$ was estimated with third order NLO susceptibility $\chi^{(3)}$.

For further understanding the EFISHG of C_{60} and CuPc which give large SHG effect from the ‘charging’ of substrate and organic film, we are going to perform surface voltage measurement called Kelvin Probe technique. With Kelvin Probe measurement, we can study quantitatively the amount of charge trapping both in film and in substrate. Kelvin probe mechanism was briefly introduced at the last section of this chapter.

APPENDIX

I.1 All-Optical poling induced second order NLO susceptibility

For All-Optical Poling AOP of nonlinear optical NLO material as shown below in figure I.1, photo-induced second order nonlinear optical susceptibility $\chi_{ind}^{(2)}$ can be approximated as :

$$\chi_{ind}^{(2)} \sim \left\langle \left(E_{\omega}(\vec{k}_{\omega}) + E_{2\omega}(\vec{k}_{2\omega}) \right)^{3} \right\rangle_{t} \sim \mathrm{Re}\left(\overline{E}_{\omega}{}^{2} E_{2\omega} e^{-\frac{\alpha}{2}r} e^{-i\Delta\vec{k}\bullet\vec{r}} + \mathrm{c.c.} \right) \qquad (I.1)$$

$$\chi_{ind}^{(2)} \sim I_{\omega} I_{2\omega}{}^{0.5} e^{-\frac{\alpha}{2}r} \cos(\Delta k_{x} x + \Delta k_{z} z + \phi) \sim \chi_{eff}^{(2)} e^{-\frac{\alpha}{2}r} \cos(\Delta k_{x} x + \Delta k_{z} z + \phi) \qquad (I.2)$$

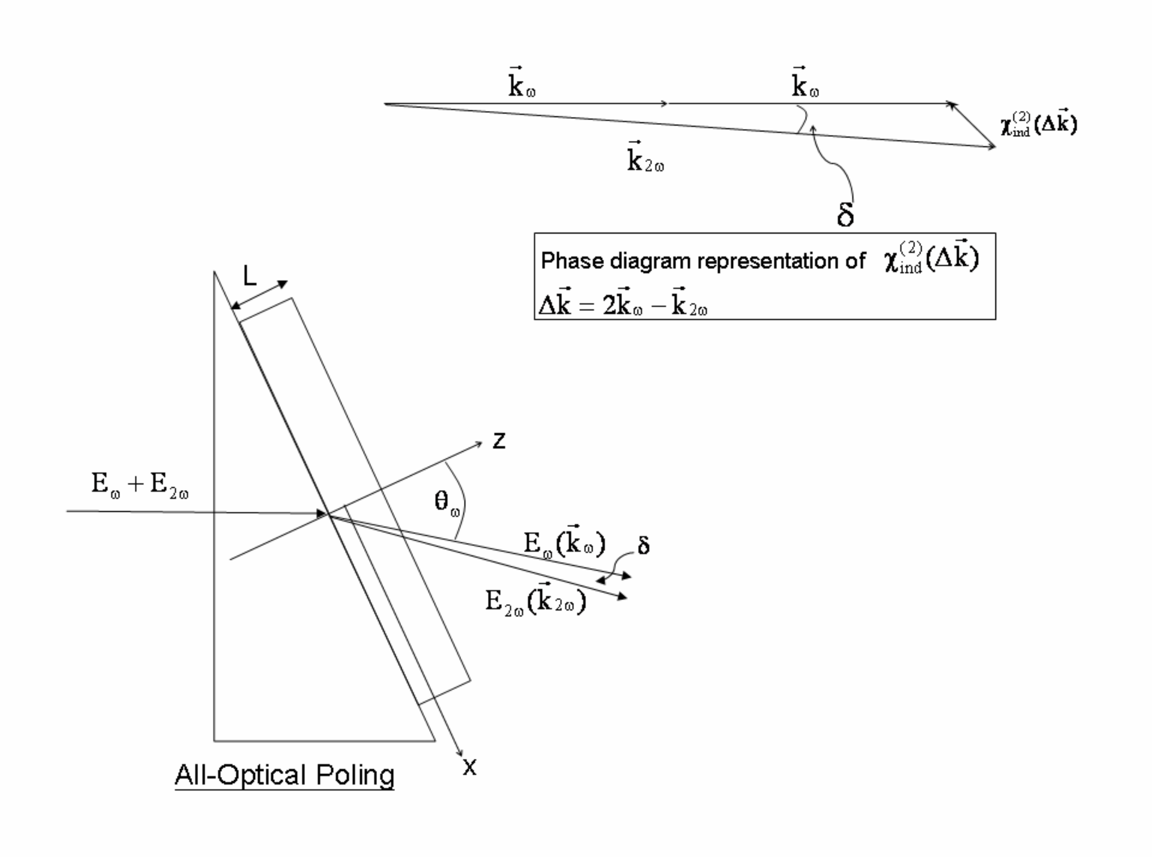

Figure I.1 All-Optical Poling and AOP-induced $\chi_{ind}^{(2)}$ grating where α is absorption coefficient at Second Harmonic SH frequency, ϕ is relative phase difference between fundamental and SH electromagnetic EM fields. Referring to equation I.2, due to the non-collinear EM waves propagation of E_{ω} and $E_{2\omega}$, $\chi^{(2)}_{\mathrm{ind}}$ is a 2-dimension grating function which vary accordingly to position in x-z space. Finite laser beam size (diameter d ~ 0.5 mm) for AOP leads to spatial averaging of $\left\langle \chi^{(2)}_{\mathrm{ind}} \right\rangle$:

$$\left\langle \chi^{(2)}_{\mathrm{ind}} \right\rangle \sim \chi^{(2)}_{\mathrm{eff}} e^{-\frac{\alpha}{2}r} \int_0^d \cos(\Delta k_x x + \Delta k_z z + \phi) dx \sim \chi^{(2)}_{\mathrm{eff}} e^{-\frac{\alpha}{2}r} \int_0^L \int_0^d \cos(\Delta k_x x + \Delta k_z z + \phi) dx dz \quad (I.3)$$

$$\left\langle \chi^{(2)}_{\mathrm{ind}} \right\rangle \sim \chi^{(2)}_{\mathrm{eff}} e^{-\frac{\alpha}{2}r} \int_0^L \int_{\phi/\Delta k_x}^{\phi/\Delta k_x + d} \cos(\Delta k_x x' + \Delta k_z z) dx' dz \quad (I.4)$$

According to previous discussion of $\chi^{(2)}_{\mathrm{ind}}$ of collinear EM waves[1], relative phase difference ϕ between E_{ω} and $E_{2\omega}$ is crucial to the efficiency of $\chi^{(2)}$ induction. However, as referred to equation I.4, relative phase ϕ effect would be cancalled out by spatial averaging of relatively large laser beam size[2] (providing that $d \gg \frac{\phi}{\Delta k_x}$). So relative phase of the fundamental and Second Harmonic (SH) EM waves will not affect average second order nonlinearity $\left\langle \chi^{(2)}_{\mathrm{ind}} \right\rangle$ induced in sample.

I.b Orientation of azo-dye molecule during AOP

Photo-induced reorientation of azo-dye molecules can be visualised in 2-level molecule system. Orientation hole burning (redistribution) by fundamental and SH EM fields (independent excitation or interference excitation) of two-level azo-dye can be expressed as[3] :

$$\begin{aligned} P_{01} \propto & \frac{(\mu_{01} \bullet E_{2\omega})\overline{(\mu_{01} \bullet E_{2\omega})}}{4} + \frac{(\mu_{01} \bullet E_{\omega})(\Delta\mu \bullet E_{\omega})\overline{(\Delta\mu \bullet E_{\omega})}\,\overline{(\mu_{01} \bullet E_{\omega})}}{16(\hbar\omega)^2} \\ & + \frac{\overline{(\mu_{01} \bullet E_{2\omega})}(\mu_{01} \bullet E_{\omega})(\Delta\mu \bullet E_{\omega}) + (\mu_{01} \bullet E_{2\omega})\overline{(\mu_{01} \bullet E_{\omega})(\Delta\mu \bullet E_{\omega})}}{8\hbar\omega} \end{aligned} \quad (I.5)$$

where the first 2 terms in equation II.5 are axial (centro-symmetric) photo-excitation due solely to fundamental/SH EM fields as they are in even order to EM field strength. The last term in the equation corresponds to noncentro-symmetric photo-excitation due to interference excitation of fundamental and SH EM fields which is the origin of AOP-induced $\chi^{(2)}$.

For the sake of simplicity of illustrating All-Optical Poling mechanism, we would assume that the EM polarization of fundamental and SH EM fields are of the same direction along z-axis as shown in figure I.2. Number of Photo-orientation of 1-D azo-dye $N_\tau(\Omega, t)$ at solid angle Ω (equation II.6) can be expanded in Legendre polynomial :

$$\begin{aligned} \frac{dN_\tau(\Omega,t)}{dt} &= -\xi\left(aN_\tau(\Omega,t)\cos^2\theta + bN_\tau(\Omega,t)\cos^4\theta + cN_\tau(\Omega,t)\cos^3\theta\right) + \\ &\xi\begin{pmatrix} a\iint N_\tau(\Omega,t)\cos^2\theta P(\Omega_1-\Omega)d\Omega_1 + \\ b\iint N_\tau(\Omega,t)\cos^4\theta P(\Omega_1-\Omega)d\Omega_1 + c\iint N_\tau(\Omega,t)\cos^3\theta P(\Omega_1-\Omega)d\Omega_1 \end{pmatrix} - \tau^{-1}\nabla^2 N_\tau(\Omega,t) \end{aligned} \tag{I.6}$$

where τ is homogeneous thermal diffusion constant, ξ is quantum efficiency for molecular orientation.

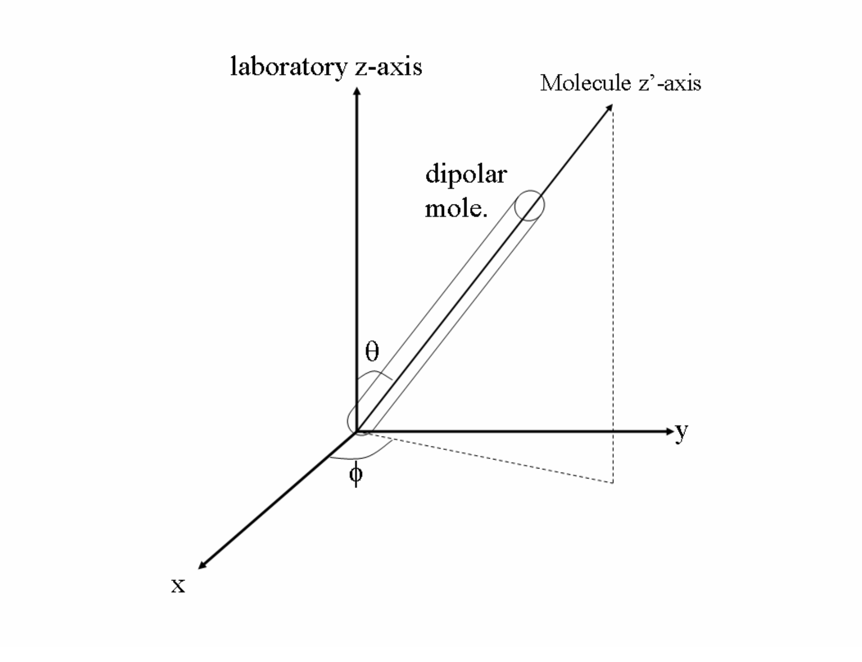

Figure I.2 Spherical coordinate representation for orientation distribution

$a \propto \mu_{01}^2 \left|E_{2\omega}^2\right|, b \propto \frac{\mu_{01}^2 \Delta\mu^2}{4(\hbar\omega)^2}\left|E_\omega^4\right|, c \propto \frac{\mu_{01}^2 \Delta\mu}{\hbar\omega}\left|E_\omega^2 \overline{E}_{2\omega}\right| \cos(\phi + \Delta k_x x + \Delta k_z z)$, μ_{01} is transition dipole moment and $\Delta\mu = \mu_1 - \mu_0$ is difference in dipole moment between excited and ground states dipole moment.

and $N_\tau(\Omega, t) = \sum_j \frac{2j+1}{2} A_{\tau,j}(t) P_j[\cos\theta]$.

For broad distribution of homogeneous thermal diffusion constant of polymer matrix, conservation of azo-dye molecule population gives :

$N = \int_0^\infty N_\tau(\Omega, t) d\tau d\Omega$ where N is the total number of azo-dye molecule in the system.

Time evolution (t') of AOP-induced $\left\langle \chi_\tau^{(2)}(0) \right\rangle_{t'}$ can be expressed as equation I.7-8 according to the relation $\left\langle \chi_\tau^{(2)}(0) \right\rangle_{t'} \sim N_\tau \beta A_{\tau,1}(t')$ and equation II.6 where β is the second order hyper-polarizability and lowest order truncation of legendre polynomial expansion $A_{\tau,1}(t')$ is assumed :

$$\left\langle \chi_\tau^{(2)}(0) \right\rangle_{t'} \sim \frac{\gamma\left(\int_0^L \int_{\phi/\Delta k_x}^{\phi/\Delta k_x + d} \cos(\Delta k_x x' + \Delta k_z z) dx' dz\right)}{15 + 21\gamma^2 + 70/(b\xi\tau)} \left[1 - e^{-\frac{b\xi}{35}\left(15 + 21\gamma^2 + 70/(b\xi\tau)\right)t'}\right] \tag{I.7}$$

$$\left\langle \chi_\tau^{(2)}(0) \right\rangle_{t'} \sim A(\Delta\Phi, \tau)\left[1 - m e^{-\frac{J}{\tau}t'}\right] \tag{I.8}$$

where γ is ratio between fundamental and SH EM fields $\sim \left|\frac{E_{2\omega}}{E_\omega^2}\right|$, $\Delta\Phi$ corresponds to the spatial averaging term.

Growth of macroscopic second order NLO susceptibility $\left\langle \chi^{(2)}(0) \right\rangle_{t'}$ of azo-dyes being hosted in polymer matrix of dispersion of thermal diffusion constant can be expressed as :

$$\left\langle \chi^{(2)}(0) \right\rangle_{t'} \sim \int_{\tau} \int_{\Delta\Phi} \left\langle \chi_{\tau}^{(2)}(0) \right\rangle_{t'} \mathrm{d}\Delta\Phi \mathrm{d}\tau \sim \int_{\tau} \int_{\Delta\Phi} A(\Delta\Phi, \tau) \left[1 - m e^{-\frac{J}{\tau} t'} \right] \mathrm{d}\Delta\Phi \mathrm{d}\tau \qquad (I.9)$$

Equation II.9 describe the $\chi^{(2)}$ growth during AOP. After the termination of AOP, azo-dyes reorientate randomly to attain centrosymmetric distribution. Without illumination (dark relaxation), a, b and c are all equal to ZERO and time evolution of $\left\langle \chi^{(2)}(t) \right\rangle_{t'}$ can be described as :

$$\left\langle \chi^{(2)}(t) \right\rangle_{t'} \sim \int_{\tau} \left(\int_{\Delta\Phi} \left\langle \chi_{\tau}^{(2)}(0) \right\rangle_{t'} \mathrm{d}\Delta\Phi \right) e^{-\frac{2}{\tau} t} \mathrm{d}\tau \qquad (I.10)$$

which illustrates clearly the multi-exponential nature of $\chi^{(2)}$ relaxation.

References

1. C. Fiorini, F. Charra, J. M. Nunzi, and P. Raimond, "Quasi-permanent all-optical encoding of noncentrosymmetry in azo-dye polymers," Journal Of The Optical Society Of America B-Optical Physics **14**(8), 1984-2003 (1997).
2. A. Apostoluk, D. Chapron, G. Gadret, B. Sahraoui, L. M. Nunzi, C. Fiorini-Debuisschert, and P. Raimond, "Quasi-phase-matched gratings printed by all-optical poling in polymer films," Optics Letters **27**(22), 2028-2030 (2002).
3. C. Fiorini, F. Charra, and J. M. Nunzi, "6-Wave Mixing Probe Of Light-Induced 2nd-Harmonic Generation - Example Of Dye Solutions," Journal Of The Optical Society Of America B-Optical Physics **11**(12), 2347-2358 (1994).